THE PENNSYLVANIA STATE UNIVERSITY
DEPARTMENT OF ENGINEERING SCIENCE & MECHANICS

EXPERIMENTAL STUDIES AND MODELING OF LITHIUM BORATE/SILICA COMPOSITE SOLID ELECTROLYTE

Muhammad Risyad Hasyim
May 2017

A thesis
submitted in partial fulfillment
of the requirements
for a baccalaureate degree
in Chemical Engineering and Engineering Science
with honors in Engineering Science

Reviewed and approved* by the following:

Michael T. Lanagan
Professor of Engineering Science and Mechanics
Thesis Supervisor

Corina S. Drapaca
Associate Professor of Engineering Science and Mechanics
Undergraduate Academic Advisor

Judith A. Todd
P.B. Breneman Chair and Professor
of Engineering Science and Mechanics
Department Head

Abstract

The development of solid electrolytes with better conductivity is crucial to meet the future energy demand and improve safety standards of today's battery and capacitor technology. Dispersed ionic conductors is a class of composite solid electrolytes, made out of a conductor and an insulator, in which conductivity enhancements of orders of magnitude can be observed at different insulator concentrations. In this work, dispersed ionic conductors are investigated both experimentally and theoretically to understand fundamental mechanisms of their unique electrical properties and determine important factors which can contribute to better conductivity in these materials.

For experimental studies, lithium borate/silica composites, 40 wt% SiO_2 with $x{\cdot}Li_2O + (1-x){\cdot}B_2O_3$, x = 0.33, 0.50, were explored with the goal of achieving Li-ion conductivity enhancements across batches with different compositions and processing steps. Enhancements across different batches were observed and all samples yielded higher conductivity than literature values for pure lithium borate conductors. Impedance spectroscopy results were also modelled through heuristics-derived bricklayer circuit models, the theoretical model (TM) and approximation model (AM), with results showing remarkable precision and accuracy of the simple models to analyze impedance data.

For theoretical studies, a rigorous framework based upon effective medium approximation (EMA) and percolation theory was developed to model general composite materials of arbitrary number of components. Solution was developed specifically for dispersed ionic conductors and applied to study percolating behaviors as well as impedance spectra of the classic $LiI - Al_2O_3$. The EMA framework showcases its practical usefulness in understanding the influence of each component in the composite towards frequency-domain electrical characteristics. Both experimental and theoretical studies elucidate important factors related to compositional, microstructural, and phase control that can help guide both experimentalists and theorists to develop better dispersed ionic conductors.

Table of Contents

List of Figures

List of Tables

List of Symbols

Alphabetical

C_{all}	Overall materials capacitance
C_g	Grain capacitance
C_{gb}	Grain boundary capacitance
$\mathbf{D}(\mathbf{r},t)$,$\tilde{\mathbf{D}}(\mathbf{r},t)$	Displacement field in the continuum composite material and its phasor form
$\mathbf{E}(\mathbf{r},t)$, $\tilde{\mathbf{E}}(\mathbf{r},t)$	Electric field in the continuum composite material and its phasor form
E_{all}	Solid electrolyte's overall activation energy
E_{int}	Activation energy of interfacial conduction pathways
$f(\hat{\sigma}, P_1, P_2, \ldots, P_M)$	Microstate probability distribution of the random AC network's complex conductivity in an M-many component system.
$G_{(l,m);k'}$	Lattice Green's function of the discrete Laplace operator
$G(\mathbf{r},\mathbf{r}')$	Green's function of the continuum Laplace operator
$\mathbf{J}(\mathbf{r},t)$, $\tilde{\mathbf{J}}(\mathbf{r},t)$	DC conduction current density and its phasor form
j_0	Local perturbation current
j_{eff}	Current passing through points A and B in an effective medium network
$\mathcal{K}_{\hat{\sigma}}^{(k)}$	k-th order coupling coefficient
n	Exponent of the constant phase element

N	Dimension of the space
P_i	Volume fraction of component i
Q_{block}	Interfacial conductor/insulator constant phase element
Q_g	Grain constant phase element
$\mathcal{Q}_{\hat{\sigma}}^{(l,k)}$	k-th order coupling coefficient of a quasi l-component system
P_a, P_b, P_c	Volume fractions of conductor, space charge layer, and insulator in a dispersed ionic conductor
p_c	Critical percolation threshold in 2-component system
p_c'	Interface percolation of dispersed ionic conductor
p_c''	Conductor/insulator transition of dispersed ionic conductor
R	Insulator particle radius
R_g	Grain resistance
R_{gb}	Grain boundary resistance
R_{int}	Interfacial conductor/insulator resistance
z	Number of connecting bonds from a single node in a network

Greek & Other Symbols

$\Delta_{M=2,3,4}$	Discriminant function of a 2-, 3-,and 4-component systems respectively
$\delta_{(l,m);(l',m')}$ or $\delta_{(l,m);l'}$	Kronecker delta on a 2D square lattice
$\delta(\mathbf{r}-\mathbf{r}')$	Dirac delta function
$\varepsilon(\mathbf{r})$, $\varepsilon_{i,j}$	Permittivity in the continuum composite material and the random AC network
η	Dimensionless space charge layer length $(1+\lambda/R)$
λ	Space charge layer thickness
$\rho(\mathbf{r},t)$, $\tilde{\rho}(\mathbf{r},t)$	Charge density of the continuum composite material and its phasor form

Σ_{AB}	Measured conductivity between two points in an infinite homogeneous network
$\hat{\sigma}_0$	Complex conductivity of an impurity taken from the random AC network
σ_{all}	Combined grain and grain boundary conductivity
$\hat{\sigma}_{\text{eff}}$	Complex conductivity of the effective medium
$\hat{\sigma}_{\text{eff}}^{\min}$, $\hat{\sigma}_{\text{eff}}^{\max}$	Theoretical minimum and maximum bounds of conductivity the effective medium
σ_{int}	Conductivity of the insulator/conductor interface
$\hat{\sigma}_m$	Complex conductivity of a homogeneous network
$\hat{\sigma}(\mathbf{r})$, $\hat{\sigma}_{i,j}$	Complex conductivity of the continuum composite material and in the random AC network
$\sigma_\infty(\mathbf{r})$, $\sigma_{i,j}^\infty$	DC conductivity of the continuum composite material and the random AC network
Φ_0	Local voltage drop caused by impurity in the effective medium
$\Phi_{(l,m);k'}$	Measured potential difference between two points in an infinite homogeneous network.
Φ_{eff}	Voltage drop between points A and B in an effective medium network
$\phi(\mathbf{r},\omega)$, ϕ_i	Potential inside the continuum composite material and at node i of the random AC network
ω	Angular frequency
∇_h^2	Discrete Laplace operator

Acknowledgments

I would like to thank a number of individuals: my thesis supervisor, Prof. Michael Lanagan, for giving me the opportunity to work on solid state ionics and being very open-minded to my modeling ideas; my co-advisor, Prof. Dinesh Agrawal, for advising the experimental studies of lithium borate/silica composites and guiding the fabrication steps; Regis Cleary, for introducing me to the project on lithium/borate silica composites in the first place; Prof. Corina Drapaca, for introducing me to applied and numerical mathematics through courses and academic advising; and last but not least, Dr. Seth Berbano, who was my graduate student mentor that guided me enormously in the first few critical years of this project and taught me the foundations of experimental materials science research; from ceramics fabrication and processing to basic theory and data interpretation of various materials characterizations, especially impedance spectroscopy.

I would also like to thank Penn State Materials Research Institute (MRI) staff: Amanda Baker, Jeff Long, Steve Perini, Julie Anderson, Nichole Wonderling, Gino Tambourine, and Maria Dicola, for their wonderful mentorship and guidance in various materials characterization and fabrication tools that MRI can offer. This material is based on work supported by the National Science Foundation (NSF) as part of the CDP (I/UCRC 1361503), NSF GRFP (DGE-1255832), NSF-ERC ASSIST (EEC-1160483), 3M Science and Technology Fellowship, and Department of Energy GATE Fellowship (DE-EE0005575). Any opinion, findings, conclusions and/or recommendations expressed are those of the author and do not necessarily reflect the views of the NSF.

Chapter 1

Background

1.1 Superionic and Dispersed Ionic Conductors

Li-ion solid-state conductors are promising replacements for current organic-based liquid electrolytes used in commercial Li-ion batteries. However, the relatively poor ionic conductivity of these solid state electrolytes presents a barrier to successful commercialization. There is a myriad of crystalline structures that are reported to have Li-ion conduction. Some of these include garnet-type $Li_7La_3Zr_2O_{12}$ [10] and $Li_5La_3M_2O_{12}$ (M = Nb, Ta) [11], thio-LISICON [12], $Li_2S - P_2S_5$ [13], perovskite $La_{0.5}Li_{0.5}TiO_3$ [14, 15], NASICON [16], $Li_{1.4}Al_{0.4}Ge_{1.6}(PO_4)_3$ [17], and LISICON ($Li_{2+2x}Zn_{1-x}GeO_4$) [18]. These materials have unique crystal structures and Li-doping to create the best Li-ion conduction pathways. However, most of these materials have room temperature conductivity values in the range of $10^{-5} - 10^{-3}$ $S\,cm^{-1}$, which are considerably lower than commercial organic liquid electrolytes, which have conductivity values at the order of $10^{-1} - 10^{-2}$ $S\,cm^{-1}$ at room temperature. There are superionic conductors that have conductivity values at the order of 10^{-2} $S\,cm^{-1}$ which rival the commercial liquid electrolytes, such as $Li_{10}GeP_2S_{12}$ [19], $Li_{10}SnP_2S_{12}$ [20], $Li_{10}Si_2PS_{12}$ [21], and $Li_{9.54}Si_{1.74}P_{1.44}S_{11.7}Cl_{0.3}$ [22].

An alternative strategy for increasing ionic conductivity is to synthesize composite or multiphase conductors. Among these composite conductors, dispersed ionic

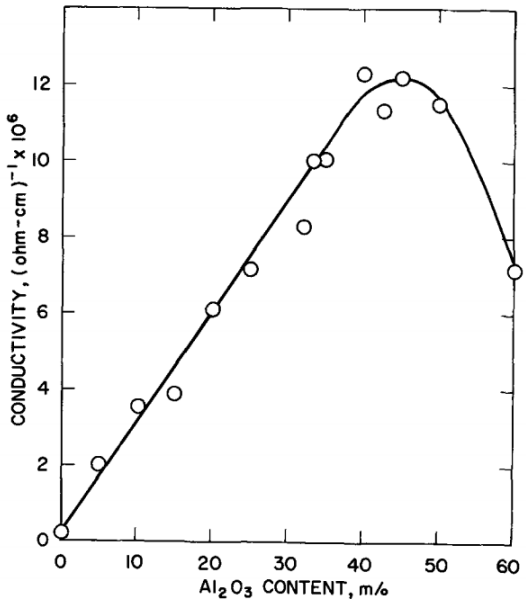

Figure 1.1: $LiI - Al_2O_3$ system, a classic dispersed ionic conductor. Adapted from Ref. [1]

conductors gave an important class of such materials. Dispersed ionic conductors are composite conductors made from conducting and insulating constituents. Despite having an insulator, the formation of space charge regions at the interfaces of the grains between the conductor and insulator causes the promotion of more vacancies or interstitials by attracting the mobile ions, effectively changing the concentration profiles of the conducting species and thus creating fast conduction pathways near the interface [5]. A more comprehensive review for the mechanism can be found elsewhere [23].

When the optimized volume fraction and phase distribution of an insulating phase is given, a conduction enhancement by orders of magnitude can be observed. The very first reported dispersed ionic conductor was a lithium-based system, a $LiI - Al_2O_3$ composite, shown in Fig. 1.1, reported an order of magnitude higher conductivity at 25 ^{o}C and Arrhenius behavior within a temperature range of -40 ^{o}C to 100 ^{o}C [1]. Other systems including $AgI - Al_2O_3$ (0-40 mol% of Al_2O_3, $25 - 150$ ^{o}C) [24], $CuCl - Al_2O_3$ (0-30 mol% of Al_2O_3, $25 - 400$ ^{o}C), shown in Fig. 1.2 [2], and $CaF_2 - Al_2O_3/BaF_2 - Al_2O_3$ (0-40 mol% of Al_2O_3, measured at 500 ^{o}C) [25], were reported to have Arrhenius behavior and conductivity enhancements up to two orders

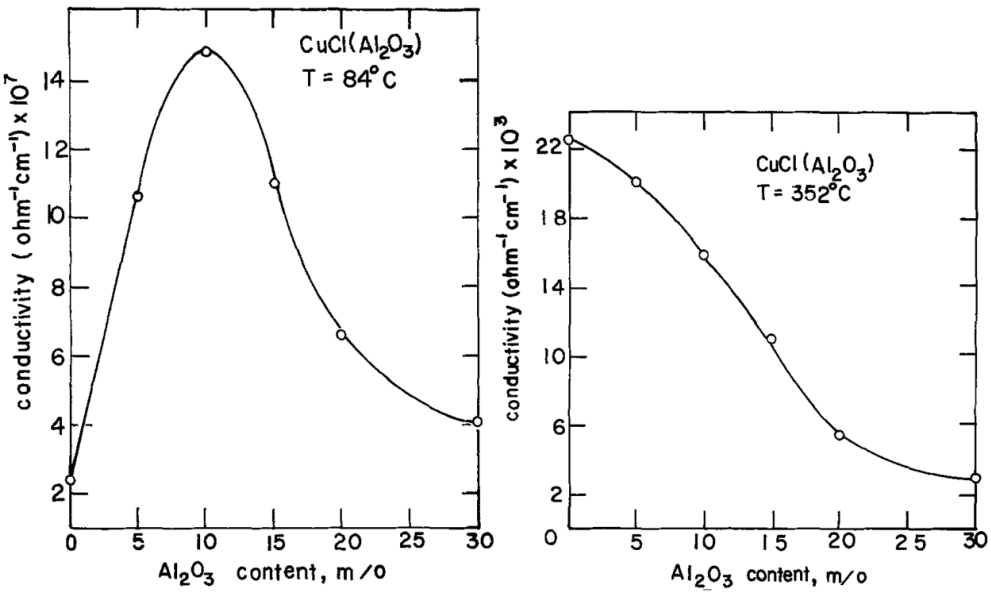

Figure 1.2: $CuCl - Al_2O_3$ system, another classic dispersed ionic conductor. Notice that at low temperatures, conductivity maximum is achieved while at higher temperatures this was not achieved, contributing to a non-Arrhenius behavior. This phenomenon is one of the many that has to be taken to account in the development of models for dispersed ionic conductors. Adapted from Ref. [2]

of magnitude. It is important to note the range of Arrhenius behavior because many of these materials exhibit non-Arrhenius behavior due to the significant presence of space charge layers at low temperatures. For a list of these dispersed ionic conductors and other composite systems, review articles and other literature can be found elsewhere [26, 27].

More recently, the concept behind dispersed ionic conductors and space charge regions is being applied to nanocrystalline conductors and multi-component oxides /insulator composites. An example of a Li-ion composite nanocrystalline conductor is the $Li_2O - B_2O_3$ system [4, 28], in which both Li_2O and B_2O_3 formed two different nanocrystalline phases instead of a single lithium borate phase. The data that were obtained can be found in Fig. 1.3. A strong functional dependence for its conductivity was found for B_2O_3 composition and grain size, a consequence of increased defects in the interface. Furthermore, in a study of multi-component oxides /insulator composites, silica was added from 0-6 vol% as an insulating phase to the

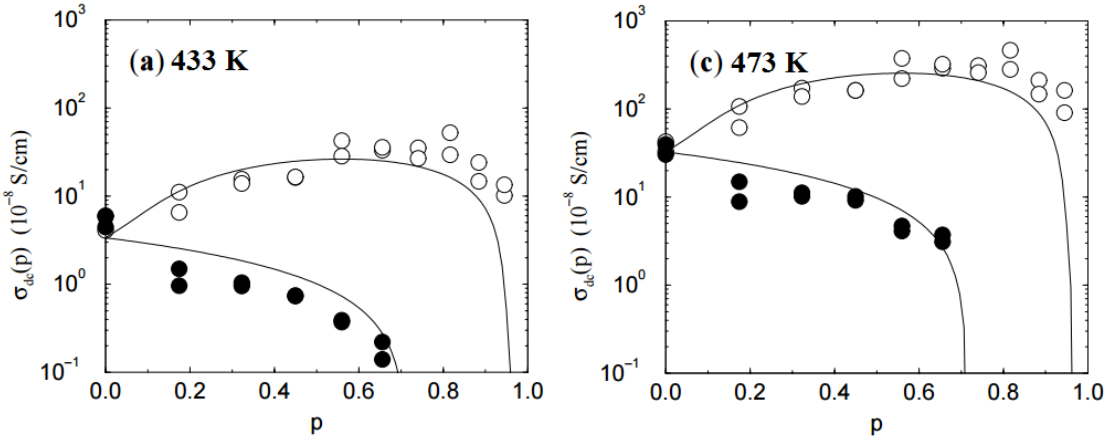

Figure 1.3: A $Li_2O - B_2O_3$ system, nanocrystalline (white) and microcrystalline (black), at two different temperatures. The curves represent best fit of the 'continuum percolation' model, which may be found in Ref. [3]. Data is adapted from Ref. [4]

.

perovskite $La_{0.5}Li_{0.5}TiO_3$ phase [29], and a blocking effect was observed since the optimal silica concentration was not reached. Another dispersed ionic conductor with a multi-component oxide is $Li_2SO_4 - Al_2O_3$, where both proton and Li-ion conduction exist, contributing to a conductivity of 10^{-2} S cm^{-1} at 500 ^{o}C [30].

1.2 Theoretical Developments

There are incredible amount of mathematical models put forth to explain the phenomena in dispersed ionic conductors. Rather than classifying the attempts based on what particular theory/mathematical technique they used, it is much easier to understand them in terms of two different levels: *microscopic* level and *macroscopic* level. While most methods fall in both categories, almost all of them will focus more in one category than the other.

At the *microscopic* level, the modeling focuses on formulating the exact mechanism of the conductivity enhancement. Assigning space-charge layer as the underlying mechanism came early during the studies of a $CuCl - Al_2O_3$ system [2]. The early proposed model is only qualitatively correct in predicting the non-Arrhenius behaviors

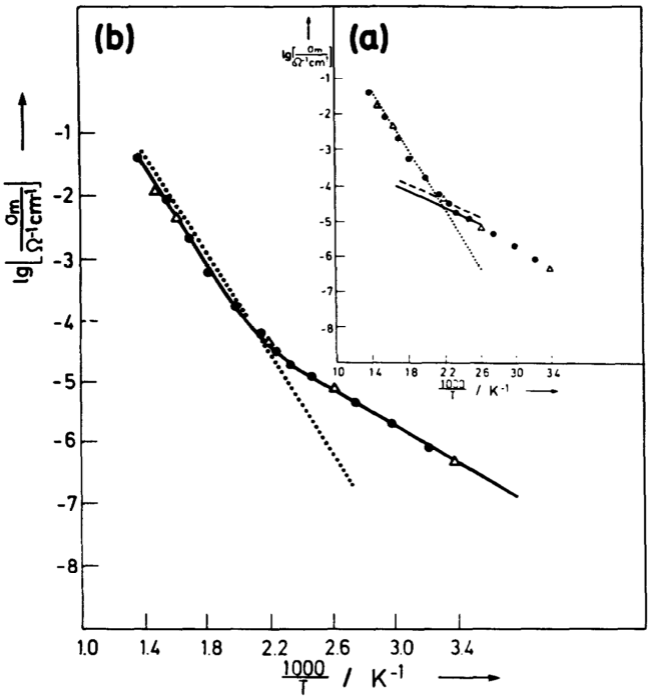

Figure 1.4: Fitting from the space charge layer model developed by Maier [5]. In dispersed ionic conductors, low activation energy is observed before it transitions to a higher activation energy corresponding to the bulk conductivity.

and dilute concentration dependence. Thus, an early improvement was made although the model is still limited to dilute insulator concentrations [31]. Later on, space charge layer models were improved even further with Maier's theoretical studies which include not only the analysis on dispersed ionic conductors but also on general two-phase composites and polycrystalline materials [5, 23, 32–35]. These developments were significant because they connect the existence of space charge layers to interfacial defect chemistry, which currently stands as the chief microscopic mechanism for the space charge layer model. More recently, the space-charge layer model have been extended with more advanced computer simulations to extend the results in 3D space [36, 37].

It is worth noting that for some dispersed ionic conductors, a secondary phase might form at the interface as a result of the interfacial defect chemistry, which maybe crystalline or amorphous [38, 39]. The existence of such phases at the interfaces was later confirmed in some studies, although composition was difficult to determine at

the time [40, 41]. The most comprehensive treatment for this particular behavior came with a paper by Jiang and Wagner [39], where an expression similar to the ones derived by Maier was made for the existence of secondary amorphous phase.

The richest development of models for dispersed ionic conductors came at the macroscopic level, which try to explain the trends in DC conductivity as a function of insulator concentrations. The surmounting difficulty for this task is due to diverse behaviors of these conductivity/concentration graphs, where conductivity maxima and trends came in a wide variety of shapes. And thus, it is important to create a 'mixing rule' for the conductor, insulator, and space charge layer from first principles that agrees with the wide variety of experimental observations. The most rigorous and successful type of modeling came through the use of statistical mechanics, in particular percolation theory, which is a physical and mathematical theory that treats the macroscopic behavior of connected clusters.

In a study of a bond percolation model, a hypothetical 2D dimensional square lattice and 3D cubic lattice dispersed ionic conductor was studied through Monte Carlo simulations, which has a conducting bond, an insulating bond, and an enhanced conducting bond representing the space charge layer [42]. With the bond-percolation approach, it was found that a dispersed ionic conductor would exhibit two transitions: interface percolation, the composite attain a state of conductivity enhancement, and the conductor-insulator transition, where the composite starts to behave as an insulator. It is later recognized, however, that not only the Monte Carlo method is numerically taxing, volume fraction equations that depend upon primitive square/cubic lattices are too simplified to describe the complex geometry of real materials. Thus, the Monte Carlo approach was replaced with a real-space renormalization group approach [8] and later on, with the effective medium approximation [3, 43].

The effective medium variant of the percolation model is important because closed-form expressions can be obtained that would be able to reproduce results from heavy computer simulations. While initially it was used to reproduce results in 2D and 3D simple lattices [43], an extension to include effects of overlapping insulator particles was made and dubbed the 'continuum percolation' model which allows it to create a more diverse set of curves that can be used to perform non-linear regression in a

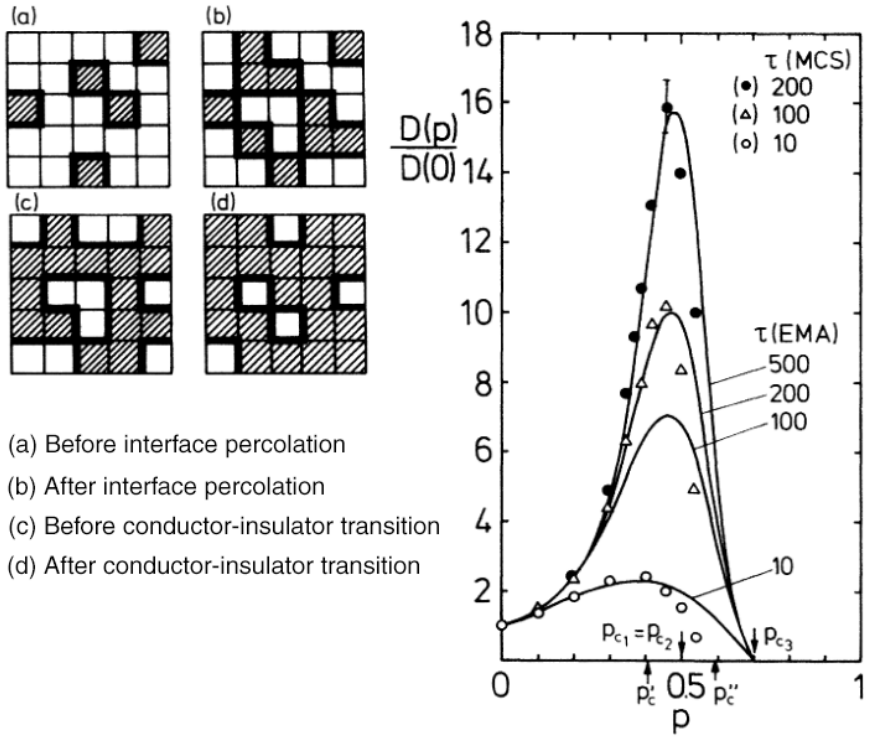

Figure 1.5: A summary of percolation model showing Monte Carlo simulation (MCS) and effective medium approximation (EMA) for 2D square lattice. The percolation model allows the transitional behavior from being a conductor to an enhanced conductor to an insulator properly. Adapted from Ref. [6]

conductivity/concentration data [3, 4], as shown in Fig. 1.3. Both the simplicity and effectiveness of the effective medium variant of percolation model leads to independent formulations of effective medium theories for dispersed ionic conductors [44–47], which are based upon a two-fold application of a two-phase effective medium theories and hence, less rigorous than percolation-based effective medium theories.

While many models have been made to address conductivity as a function of temperature and phase concentration, only a relatively small amount has been done to extend them to frequency domain. This is despite of the fact that frequency-domain characterization tools such as impedance spectroscopy is one of the most popular electrical characterization tools to probe microscopic phenomena. Most theoretical studies indicate abrupt changes in dielectric behavior when the dispersed ionic conductor comes near to any of the percolation thresholds, such as maximum peaks and

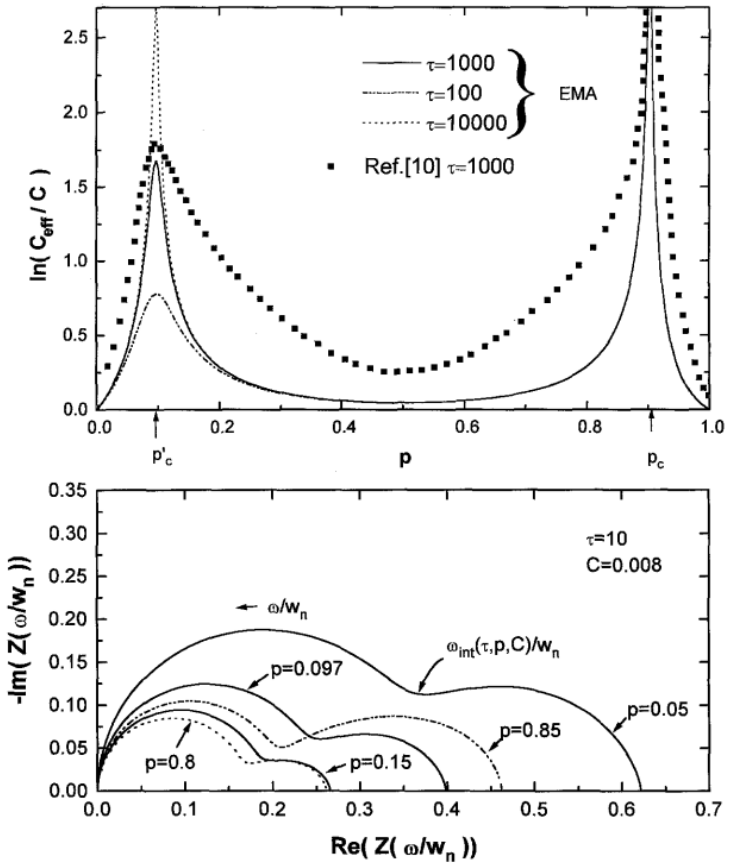

Figure 1.6: Behavior of static capacitance/dielectric constant, adapted from Ref. [7]. Dotted data come from Ref. [8]. Notice that a peak is achieved at interface percolation and a singularity is achieved for conductor/insulator transition.

singularities [7, 8, 46]. The effective medium approximation made from percolation theory was later extended to frequency domain under the stochastic transport theory scheme, where it was found that percolating paths intrinsically have their own dispersive and capacitive element, that can be shown in Nyquist plots and producing asymmetric curves in the electrical modulus plots [7]. Fig. 1.6 shows the results of the frequency domain studies from Ref. [7].

1.3 Outline of Work

The main objective of this work is to study the fundamental mechanism of conductivity enhancements in dispersed ionic conductors and derive some important factors which can contribute to better conductivity. Meeting this objective requires a holistic investigation which includes both *experiment* and *theory*:

1. *Experiment*: Studies need to be conducted to comprehensively review the effects of fabrication steps, such as sintering and milling. Thus, lithium borate/silica composites, 40 wt% SiO_2 with $x{\cdot}Li_2O + (1-x){\cdot}B_2O_3$, x = 0.33, 0.50, were explored where different batches named *micron* and *nanoscale* were made. Extensive characterization is performed to study the phase, microstructure, and electrical properties of these materials.

2. *Theory*: The lack of rigorous yet simple mathematical model that connect (1) insulator concentration and (2) frequency dependence needs to be addressed. To address this issue, the problem of modeling composite materials with arbitrary number of components was tackled instead, from the point of view of effective medium approximation (EMA) and percolation theory. Key concepts such as *random AC networks* and *lattice Green's functions* are intimately connected to the rigorous foundation of the derived final model for dispersed ionic conductors.

Chapter 2 will discuss the experimental study conducted on these lithium/borate silica composites. Chapter 3 will discuss the theoretical study conducted to derive the general effective medium approximation framework for composite solid electrolytes.

Some content of this thesis has been adapted with permission from the following publication:

- Hasyim, M. R., S. S. Berbano, R. M. Cleary, M. T. Lanagan, D. K. Agrawal (2017), "Impedance spectroscopy modeling of lithium borate with silica: A dispersed ionic conductor system," *Ceramics International*, **43**(9), pp. 6796-6806. http://doi.org/10.1016/j.ceramint.2017.02.097. See Ref. [48].

Chapter 2

Impedance Spectroscopy Study of Lithium Borate/Silica

In this work, a lithium borate, $x \cdot Li_2O + (1 - x) \cdot B_2O_3$ ($x = 0.5, 0.33$) $-SiO_2$ system was synthesized, which shall be denoted as lithium borate/silica composites. These composites are synthesized to observe conductivity enhancements as function of precessing methods in a similar vein with previous studies [4] as well as analyzing the dispersive phenomena in their impedance spectroscopy data. Later in Section 2.3, an analytical circuit model will be derived through heuristics arguments based upon careful consideration of the microstructure and phase characterization. In particular, deviations from classical impedance plots will be explained carefully through proper choices of circuit elements, each of which has an assigned physical and microstructural meaning to them.

Microstructural and phase characterizations consisting of scanning electron microscopy (SEM), energy dispersive X-ray spectroscopy (EDS) and X-ray diffraction (XRD) were used to confirm the successful synthesis of the lithium borate/silica composites. Consequently, impedance spectroscopy measurements were used to support the newly proposed models based upon two aspects: (1) goodness of fit, (2) uniqueness of the fit, and (3) their ability to reproduce essential results necessary to verify the existence of the dispersed ionic conductor phenomena.

2.1 Materials and Methods

The lithium borate/silica composite materials were synthesized and categorized based upon size reduction processes. There were two distinct batches; the first batch, named micron batch, utilized amorphous fumed silica and a 24 h ball milling to mix the two powders together while the second batch, named nanoscale batch, sought to reduce the particle size down to submicron-to-nanoscale lengths by high-energy planetary milling for 8 hr, a method that has shown to increase ionic conductivity by several orders of magnitude [49]. In addition, 20 nm silica nanopowder was used for the nanoscale batch. Different lithium oxide/boron oxide mole ratios/fractions were also explored. Two mole ratios will be used: R = 1.0 corresponding to x = 0.50, and R = 0.5 corresponding to x = 0.33. The silica constituent was fixed at 40 wt%. In later sections, a sample will be referred to its mole fraction and batch, e.g., x = 0.50 nanoscale sample. Table 2.1 summarizes the different types of samples across the two batches along with the naming conventions for them.

Table 2.1: Naming conventions for the lithium borate/silica samples. All samples undergo identical ceramic fabrication process as prescribed in Fig. 1. Optimization is based on size reduction principle. *a variant named x = 0.33, nanoscale-S was created by sintering the sample at 550 ^{o}C and sputtering the Ag electrode instead of co-firing.

Ratio of $n_{Li_2O}/n_{B_2O_3}$	R = 0.5 (x = 0.33)	R = 1.0 (x = 0.50)
Micron batch 24 h ball-milling amorphous silica	x = 0.33 micron	x = 0.50 micron
Nanoscale batch 8 h planetary milling amorphous nanosilica	x = 0.33 nanoscale x = 0.33 nanoscale-S*	x = 0.50 nanoscale

Lithium carbonate (99.998% Alfa Aesar), boric acid (99.99% Alfa Aesar), amorphous fumed silica (99.8% Alfa Aesar), and nano $-$ SiO_x amorphous (99.5%, x = 1.2 to 1.6, Nanostructured and Amorphous Materials, Inc.) were used as obtained. Stoichiometric mixtures of lithium carbonate and boric acid were calcined at 700 ^{o}C for 1 h, ramped from room temperature at a rate of 3 ^{o}C/min, yielding a white fluffy powder. The white powder was then ball milled for 24 h, melted at 1000 ^{o}C, ramped

from room temperature at a rate of 3 °C/min, and melt-quenched to produce a clear lithium borate glass. The glass was grounded in a mortar and pestle then ball milled for 24 h to produce a fine amorphous white powder.

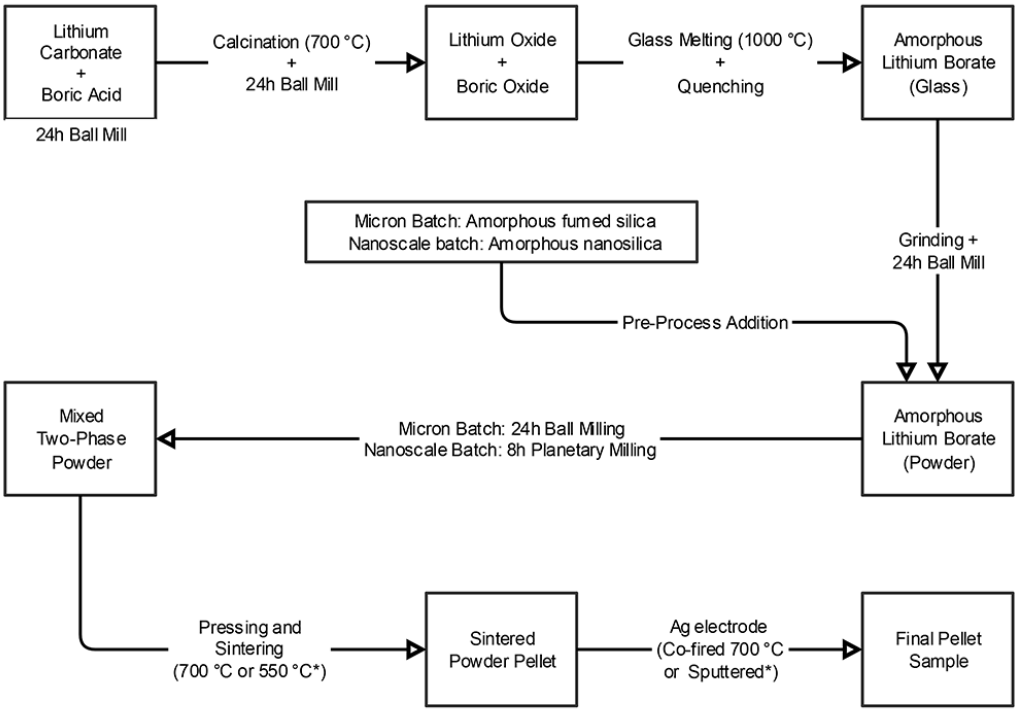

Figure 2.1: Fabrication steps for the lithium borate/silica glass-ceramics. Temperatures within each step correspond to peak temperatures of the heat treatments. * 550 °C sintering with sputtering was done with x = 0.33 nanoscale-S sample only.

For the micron batch, amorphous fumed silica was introduced to the newly synthesized amorphous powder after melting and prior to the 24 h ball milling. After ball milling, the powder was pressed into a pellet at a pressure of 155 MPa for 5 minutes and 232 MPa for 3 minutes subsequently using a uniaxial press and sintered at 700 °C for 1 h. Ag thick film paint was painted on the pellets and co-fired in a tube furnace with the pellets at 700 °C in Ar (80 cc/min). For the nanoscale batch, amorphous nanosilica was introduced followed by 8 h high-energy planetary milling to produce the two-phase mixed powder. These samples followed the same press-and-sinter process and electrode co-firing, with the exception of one sample (x = 0.33 nanoscale-S) which was sintered at a lower temperature (550 °C for 1 h) and elec-

trodes were sputtered to avoid the high-temperature co-firing process. This special variation was conducted to observe phase-change and re-crystallization effects. Fig. 2.1 summarizes all the steps required in fabricating the composite material for the two different batches. Fig. 2.2 shows the locations for the sample's compositions in an equilibrium phase diagram. The phase diagram will be helpful in identifying any anomalies in XRD patterns.

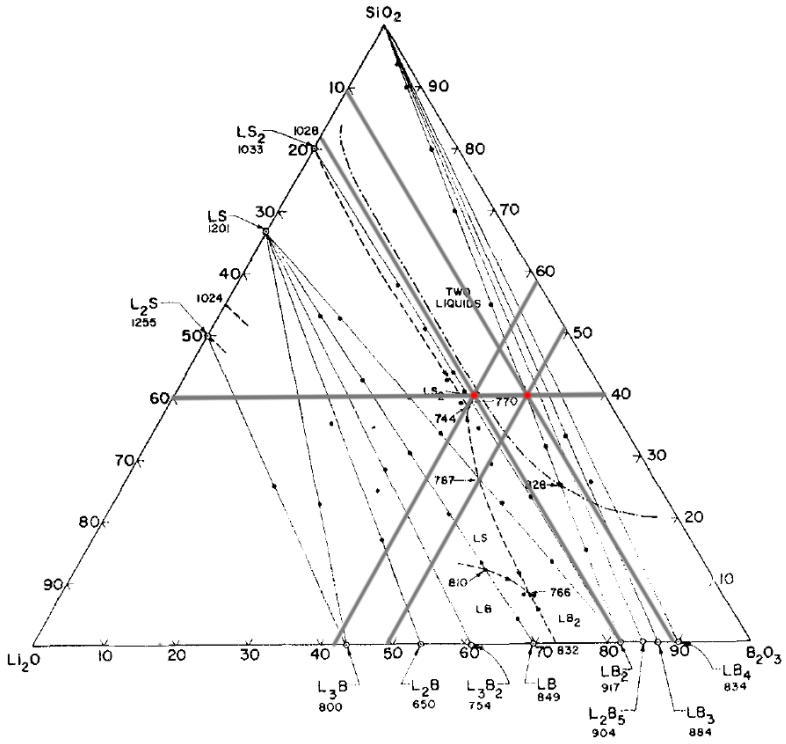

Figure 2.2: Location of synthesized lithium borate/silica composites in an equilibrium ternary phase diagram for x = 0.50 and x = 0.33.

Impedance spectroscopy was conducted in a temperature-controlled chamber from 1 MHz 0.01 Hz with temperature ranges that varied depending on the samples, typically 200-500 °C. X-ray powder diffraction (XRD) data were obtained using a Ni-filtered Cu Kα radiation source (PANalytical Empyrean). The 2θ range was set to be 5-70^o degrees with a step size of 0.026 2θ/min. Scanning electron microscopy (SEM) was utilized (FEI Nova NanoSEM 630 FESEM) and energy dispersive x-ray spectroscopy (EDS) was conducted to observe elemental distributions in the samples. For SEM imaging, samples were fractured and prepared inside a non-conductive epoxy resin, as well as polished and coated with iridium to avoid charging.

2.2 Microstructural and Phase Characterization

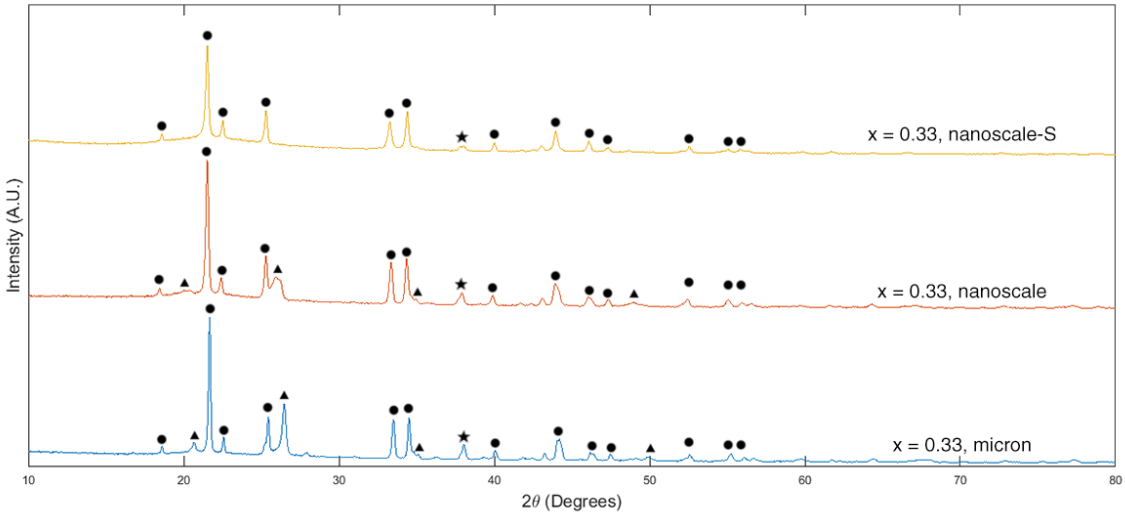

Figure 2.3: XRD patterns for samples with ratio R = 0.5 or x = 0.33 (● - $Li_2B_4O_7$; ▲ - SiO_2; ⋆ - Ag).

Fig. 2.3 shows the X-ray diffraction patterns for samples with R = 0.5 or x = 0.33 for the micron and nanoscale samples. Two separate crystalline phases were identified, lithium tetraborate $Li_2B_4O_7$ and quartz silica. With these XRD results, it also confirmed that a crystallization process occurred within the composite material, starting from glassy lithium borate and amorphous silica powder. Furthermore, the special sample (x = 0.33, nanoscale-S) missed quartz silica peaks within its spectra. This evidence suggested further that the silica phase in these composite materials re-crystallized during the sintering or the electrode co-firing step. In addition, from previous studies of $Li_2O - B_2O_3$ and $Li_2O - B_2O_3 - SiO_2$ phase diagrams [50, 51], provided also in Fig. 2.2 (see page 13), the x = 0.33 composition (weight fractions of 0.400 for SiO_2;0.106 for Li_2O; 0.494 for B_2O_3 and mole fractions of 0.385 for SiO_2; 0.205 for Li_2O; 0.410 for B_2O_3) should be exactly in the binary join of SiO_2 and Li_2O-$2B_2O_3$ (LB_2). Thus, in this particular ratio and/or composition, the phase composition that was sought through nonequilibrium processing matches with the equilibrium phase composition.

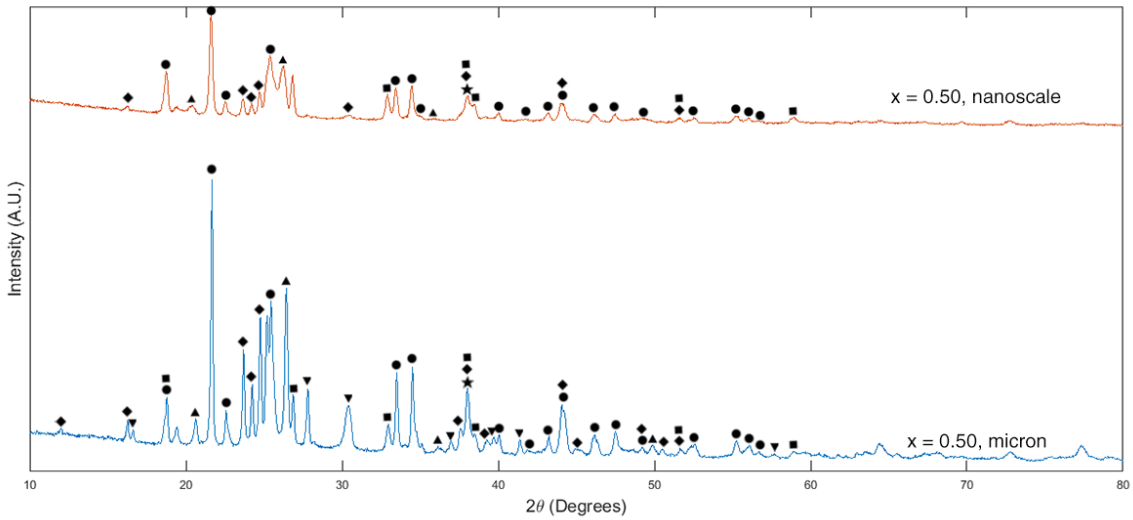

Figure 2.4: XRD patterns for samples with ratio R = 1.0 or x = 0.50 (● - $Li_2B_4O_7$; ▲ - SiO_2; ★ - Ag; ♦ - $Li_2Si_2O_5$; ■ - Li_2SiO_3; ▼ - $LiBO_2$).

Fig. 2.4 (see page 15) shows X-ray diffraction patterns for samples with R = 1.0 or x = 0.50 for the micron and nanoscale samples. Based on stoichiometry and previous result on x = 0.33, samples were expected to contain lithium metaborate $LiBO_2$ and quartz silica phases only. However, peak analysis indicated that multiple phases had been formed. These phases included lithium borates ($Li_2B_4O_7$ and $LiBO_2$), lithium silicates ($Li_2Si_2O_5$ and Li_2SiO_3) and quartz silica. Referring to the same phase diagram [50, 51], the x=0.50 composition (weight fractions 0.400 for SiO_2; 0.180 for Li_2O; 0.420 for B_2O_3 and mole fractions of 0.356 for SiO_2; 0.322 for Li_2O; 0.322 for B_2O_3) should be in a phase field with SiO_2 (S), Li_2O-$2SiO_2$ (LS_2), and Li_2O-$2B_2O_3$ (LB_2) phases, albeit very close to the binary join of LS_2 and LB_2. While the non-equilibrium processing methods helped in retaining the lithium metaborate (LB) phase, the higher lithium content of the x=0.5 samples provided a path for reaction with silica, allowing additional lithium silicate (LS_2) and borate (LB_2) phases to be observed in the XRD patterns. Furthermore, due to how close the composition is to the binary join, uncertainty in the actual composition provides a possibility that the x=0.50 sample lies in the neighboring phase field with Li_2O-SiO_2 (LS), Li_2O-$2SiO_2$ (LS_2), and Li_2O-$2B_2O_3$ (LB_2). This would explain why lithium metasilicate (LS) was observed in the XRD patterns.

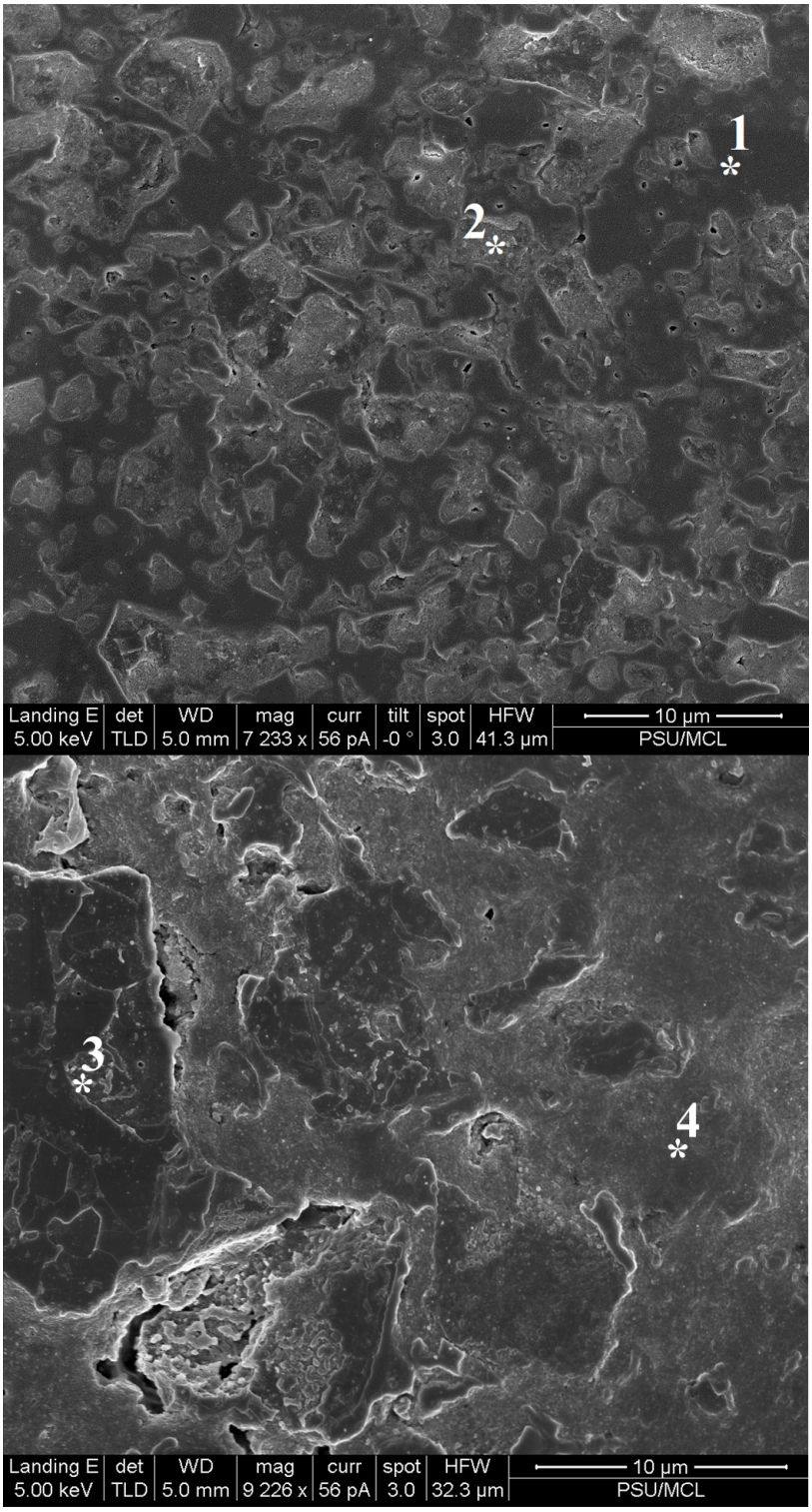

Figure 2.5: SEM images of x = 0.33, nanoscale (left) and x = 0.33, micron (right) polished cross-sections. Lighter region is the silica rich phase while the darker region is the lithium borate rich phase. Numberings on SEM images correspond to the sample point EDS spectra in Fig. 2.6.

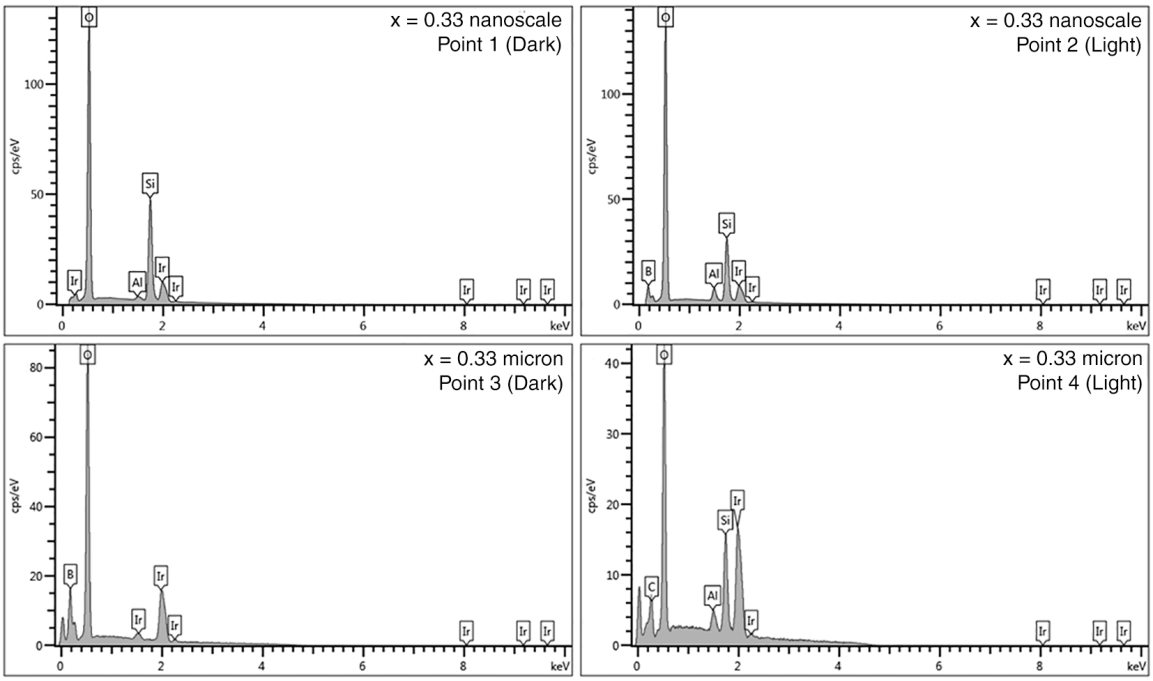

Figure 2.6: Sample of compiled EDS spectra for x = 0.33 nanoscale and micron samples. For the nanoscale sample, the phases were homogeneously distributed making EDS point spectra vary widely. Hence, an almost identical elemental distribution for two different regions can be observed. Meanwhile, the micron samples gave a better elucidation of elemental distribution.

Fig. 2.5 (see page 16) provides the SEM images for micron and nanoscale samples at x = 0.33, highlighting their microstructure. Since silicon is the heavier element than boron, the lighter region can be identified as the silica rich phase while the darker regions can be correlated with lithium borate rich phase for both samples. Multiple point EDS measurements in the micron sample, some of which are provided in Fig. 2.6 (see page 16), also supported this distribution. However, multiple point EDS measurements on the nanoscale sample, some of which are also provided in Fig. 2.6, did not provide clear elucidation of the elemental distribution. In fact, Fig. 2.6 provides two point EDS measurements for the nanoscale sample that have identical elemental distributions but located at a dark and light region. The logical explanation for this anomaly is that as a micron technique, the sampling volume of EDS exceeded the volume of the phases in the samples, which occupied regions less than 10 μm, causing an overlap between different phases during the point EDS measurements of the nanoscale sample.

The amount of volume that these two phases occupy in each sample is very crucial in the subsequent circuit modeling. For micron samples, each phase took in a very large volume and as a consequence, there was less contact surface area between the silica rich phase and the lithium borate rich phase. Furthermore, the uneven distribution also caused some lithium borate rich phases to be completely isolated and immersed in the silica-rich phase. On the other hand, nanoscale samples had a much more homogeneous distribution between the two phases and occupied a much smaller and even volume. Hence, it is expected that nanoscale samples had a higher interfacial area.

Once the materials phase composition and microstructure have been considered, impedance spectroscopy can be used to validate the new equivalent circuit models and quantify the characteristics of the conduction mechanisms. In this chapter, characterization results on phase composition and microstructure are presented to provide evidence that the two-phase microstructure arrangement validated a need for new equivalent circuit models. In Section 3.2, equivalent circuit models are formulated based on the assumption of dispersed ionic conductor starting from a brick-layer physical picture. Afterwards, in Section 3.3, the results from impedance spectroscopy are used to rigorously test the newly-made equivalent circuit models.

2.3 Circuit Modeling

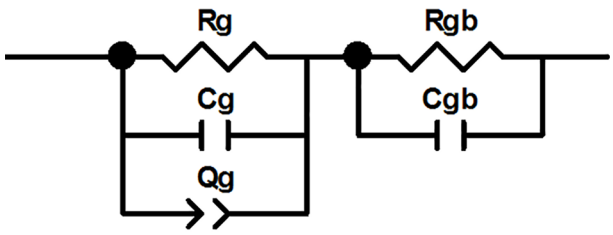

Figure 2.7: The classical circuit model (2P) for a polycrystalline material. The 2P model has a modification in the grain to account frequency dispersion.

Shown in Fig. 2.7 is a variation of a classical model that is found in many polycrystalline material studies, which shall be denoted as the 2P model. In this typical

model, one parallel RC circuit refers to the grain contribution and the other refers to the grain boundary contribution. The parameters are grain resistance R_g, grain boundary resistance R_{gb}, grain capacitance C_g, grain boundary capacitance C_{gb}, and grain constant phase element Q_g. A constant phase element (CPE) is added in parallel to the grain parallel RC circuit to take account the frequency dispersion that persists in many polycrystalline materials. The assignment of the CPE in such a manner is a common procedure [52]. Additionally, this model will serve as a benchmark for the newly proposed circuit models.

There is great evidence that both micron and nanoscale samples are composed of two regions which are conductor-rich and insulator-rich separately. Hence, all of the samples require a more involved circuit model where interactions commonly found in a dispersed ionic conductor matter. To develop such circuit model, it is worth explaining the primary assumptions. These primary assumptions rely on the physics that have been already established within the field of dispersed ionic conductors, as well as common conventions in developing circuit models:

- Brick-layer assumption: given that grain size distribution is narrow and the grain shapes are isotropic, a material can be modeled as composed of smaller cubes/squares, representing bulk grains, stacked together uniformly and bordered with their grain boundaries [53].

- Dispersed ionic conductor assumption: There exist fast-transport ionic conduction regions within the boundaries of a conductor and insulator.

Fig. 2.8.a shows the brick-layer physical picture. The brick-layer physical picture represents a 2D brick layer model that has two different phases randomly scattered but follows the specified composition being used (40 wt%). It is worth noting that Fig. 2.8.a is very similar to the realizations of percolation models mentioned previously, especially regarding the lattice-like pictures that the percolation model proposes. The difference between the brick-layer physical picture and the percolation models is that the physical picture explicitly includes the boundaries that act, in a sense, as a third phase that contributes to overall conductivity process. In addition, the boundaries are also labeled to be amorphous for this physical picture, rather than the purely grain boundary treatment that is often seen in brick-layer models.

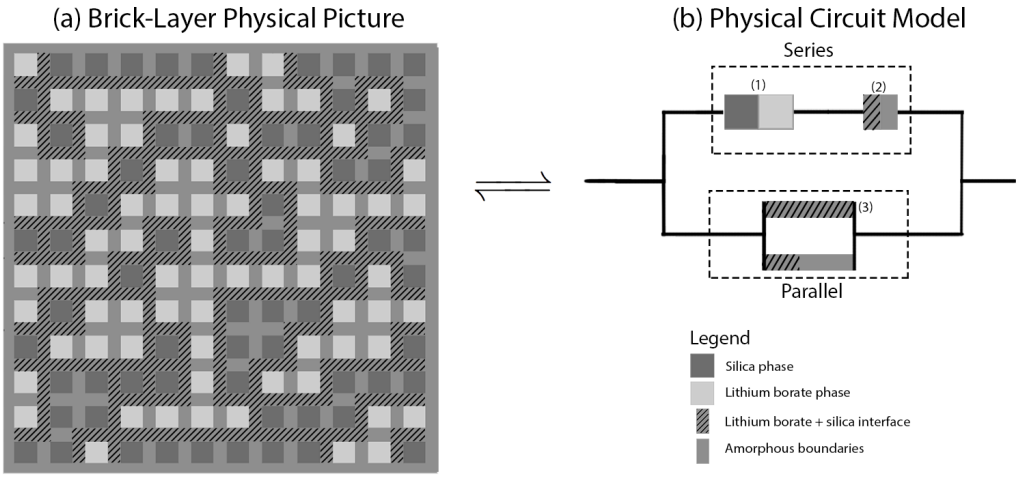

Figure 2.8: (a) The brick-layer physical picture, which gives an idea of how the circuit model can be made with dispersed ionic conductor assumptions and microstructure. (b) The physical circuit model, which provides a way to break down the physical picture into the series and parallel configuration. In the series configuration, transport contribution is divided into an effective mean grain impedance and effective mean grain boundary impedance. Each impedance is a mixture contribution for each phase. In the parallel configuration, transport configuration is dominated by interface pathways partially blocked by amorphous boundaries.

Like circuit models derived from the brick-layer model, the series and parallel configuration of the brick-layer physical picture will be considered, denoting two pathways for charge carriers to move through the microstructure [53]. In the conventional brick layer model, the series configuration often refers to both grain (squares) and grain boundary (adjacent, left-right boundaries) components connected in series. In this particular brick-layer physical picture, the construction has a fundamental difference. With a two-phase composition, there are now three different kinds of boundaries: conductor-conductor, insulator-insulator, and conductor-insulator. There are also two types of grains: conductor grains and insulator grains. By the same principle, the series configuration must be represented as five different components connected in series. This is impractical in nonlinear regression analysis, where too many parameters can cause convergence issues and large error values. Hence, only effective boundary and effective grain contributions should be considered. In here, effective refers to a component which is made from the combination of two or more similar components and taken entirely as one entity.

The parallel configuration is unique in that it is purely composed of boundaries and interfaces; the crucial feature in dispersed ionic conductors. A very similar principle to that in percolation models is used. In a percolation model, the critical threshold in which conductivity enhancement is found is when one continuous line network of insulator-conductor boundaries is formed. In the brick-layer physical picture, this is possible but quite unlikely given the current composition. Hence, it is more likely for the interface pathways to be discontinuously broken by the normal amorphous boundaries that no longer contain the insulator-conductor boundaries. The concept of discontinuous conducting pathways can be found in the modeling of impedance spectra of concrete where discontinuous conduction pathways exist due to concrete paste intermediates essentially acting as insulators [54, 55].

The analysis of the series and parallel configuration can be transported to the physical circuit model which is shown in Fig. 2.8.b. Physical refers to how pieces from the brick-layer model, boundaries, and grains, are assembled directly to act as pseudo-circuit components. These pieces are properly assembled in accordance to the previous qualitative analyses on the parallel and series configurations. By having this picture, electrical circuit components can be assigned to each configuration.

Fig. 2.9.a shows the equivalent circuit for the theoretical model (TM). For the series configuration, there are different circuit elements such as R_g acting as the effective grain resistance, R_{gb} as the effective grain boundary resistance, C_{gb} as the effective grain boundary capacitance, and C_{all} as the overall materials capacitance. Meanwhile, for the parallel configuration, a resistor R_{int} defined as the interfacial conductor/insulator resistance and a constant phase element Q_{block} can be found. The reasoning for the particular arrangement of circuit elements will be elaborated in the subsequent paragraphs.

For the series configuration, a ladder topology is adopted instead of the usual series topology adopted in circuit modeling of multi-phase materials. One reason is that ladder topology is very common for slightly more complex ionic conduction mechanisms. For instance, both a ladder network and its generalization, a transmission line, have been used for mixed ionic-electronic conductors to model the contribution of conventional ionic conduction in the grain and grain boundaries as well as the

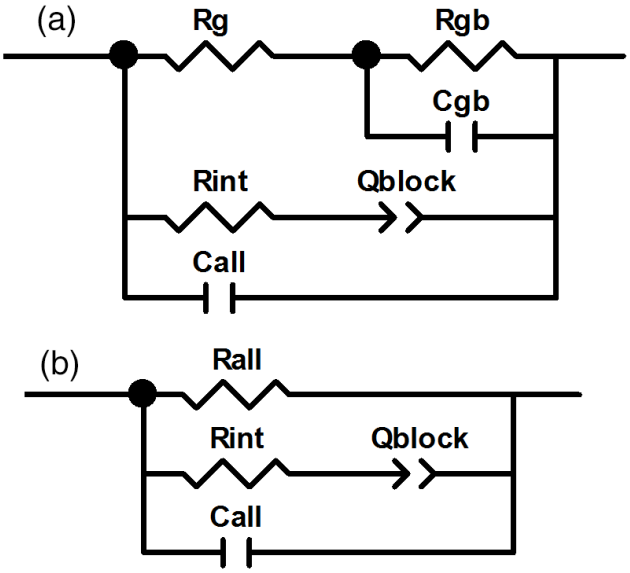

Figure 2.9: (a) The final theoretical model (TM). $(R_{int} + Q_{block})$ represents the parallel configuration while $(C_{all}^{-1} + (R_g + (R_{gb}^{-1} + C_{gb}^{-1})^{-1})^{-1}$ represents the series configuration. (b) The approximation model (AM). The series configuration is simplified by eliminating C_{gb}.

electronic conduction [56, 57]. Another reason is because both a ladder topology and series topology can be exchanged mathematically, creating somewhat similar but directly analogous circuit components that have similar roles for both practical and modeling purposes [58].

For the parallel configuration, three RC parallel circuits in series corresponding to the three different interfacial boundaries is the straightforward modeling method. However, this suffers from not being able to capture the characteristic discontinuous conduction pathways expected. Similar to researchers studying concrete [54], this specific conduction process is instead modeled with a resistor in series with a constant phase element. The choice of the constant phase element is necessary since the conduction (represented as the resistor) is not ideally blocked by the amorphous boundaries, but some amount does pass through and contributes to ionic conduction. Since a constant phase element can be interpreted as a non-ideal capacitor, it becomes the choice component to be combined in series with the resistor.

At first glance, this model is a reasonable circuit model that can be used for nonlinear regression analysis. Furthermore, all seven parameters have assigned microstructural meaning to them, which gives the model a good physical foundation. However, the amount of parameters involved will be problematic during higher temperature measurements required to obtain Arrhenius behavior. In this situation, impedance semicircles shift to a higher frequency region (> 1 MHz) outside of the instruments range and creating incomplete semicircle arcs. When this happens, convergence issues and error values emerge. Hence, simplifications must be made to the TM model in order for Arrhenius behavior to be captured properly.

This simplification can be achieved by ignoring relaxation associated with the effective grain boundary, i.e., removing C_{gb}. This exclusion can be made by assuming that the large portion of the relaxation process observed is due to the discontinuous conduction pathways at the interfaces. By removing this component, there will also be a need to combine the effective grain resistor R_g and an effective grain boundary resistor R_{gb} into a single resistor R_{all}. This model shall be referred as the approximation model (AM), as shown in Fig. 2.9.b.

It is important that the TM and AM models are tested in a rigorous manner, i.e. the TM and AM models uniquely and accurately fit the experimental data. Thus, in the subsequent impedance analysis section, the 2P, TM, and AM models were used to fit impedance data of all samples at a selected, moderate temperature ($200 - 300$ ^{o}C). The classical 2P model would serve as a benchmark for the new models. Furthermore, the models were simulated at higher and lower frequencies to showcase the full relaxation feature.

Further validation must also come from predicting two other aspects: (1) physically realizable values for common components and (2) proper relations obtained between two values which are consistent with the dispersed ionic conductor assumption. For these relations, two main hypotheses are presented to test against the nonlinear regression results:

1. Effective grain resistance will be higher than the other resistances at lower temperatures. In the TM model, this means that $R_g > R_{gb}$ and $R_g > R_{int}$. Lower temperatures are specified since it is expected that the conduction pathways

have different activation energy, hence a temperature crossover point may exist.

2. The energy barrier or activation energy for conduction in normal grain/grain boundary pathways is higher than those with the insulator-conductor interfaces. This can be shown with the AM model when $E_{all} > E_{int}$, where E_{all} is the combined activation energy and E_{int} is the interface activation energy for the discontinuous conduction pathways.

Lastly, the AM model will be used to generate Arrhenius plots and obtain activation energy values for the nanoscale and micron samples.

2.4 Electrical Characterization

Fig. 2.11 shows the combined Nyquist, imaginary impedance ($-Z''$) semi-log and imaginary modulus (M'') semi-log plot for x = 0.33 nanoscale with all three fitted models. Fig. 2.12 shows the combined plot for x = 0.50 micron with all three fitted models. The plots for the rest of the samples (x = 0.50 nanoscale and x = 0.33 micron) are also provided in Fig. 2.13 and Fig. 2.10 respectively. In all of these figures, the most common feature is a depressed and seemingly asymmetrical single arc. This is counter-intuitive with the understanding of dispersed ionic conductors since these materials exhibit different phases, boundaries, and conduction mechanisms; all of which should provide at least two semicircles that are distinguishable. This contradiction can be resolved by realizing that highly-overlapped relaxation processes can still occur for multi-phase materials, as exemplified in works by Fricke on effective-medium approaches [59, 60].

Although it looked as if all models fitted the data correctly at first glance, it is clear that the benchmark 2P model did not fit the experimental data very well. When simulated to higher frequencies, the 2P model revealed an anomalous high-frequency M" tail that does not correspond to the measured electrical data. Such error can be sourced from badly parametrized values for the bulk constant phase element. On the other hand, the newly proposed models (TM and FM) can replicate a proper and symmetrical relaxation peak as expected for a real modulus data, despite the constant phase element that is present in both models. The successful prediction of the M" peak and goodness of fit proved one part of the validity of these new models.

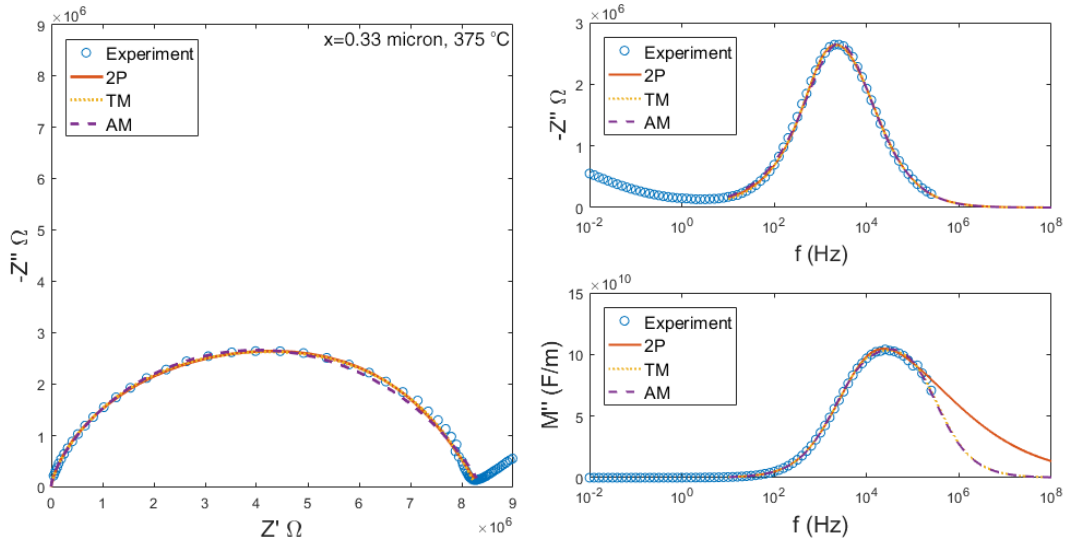

Figure 2.10: Combined Nyquist, imaginary impedance (-Z") semi-log, and imaginary modulus (M") plot of x = 0.33, nanoscale sample at 300°C. The benchmark 2P model predicted a large high-frequency M" tail while the TM and AM models captured the relaxation behavior more properly.

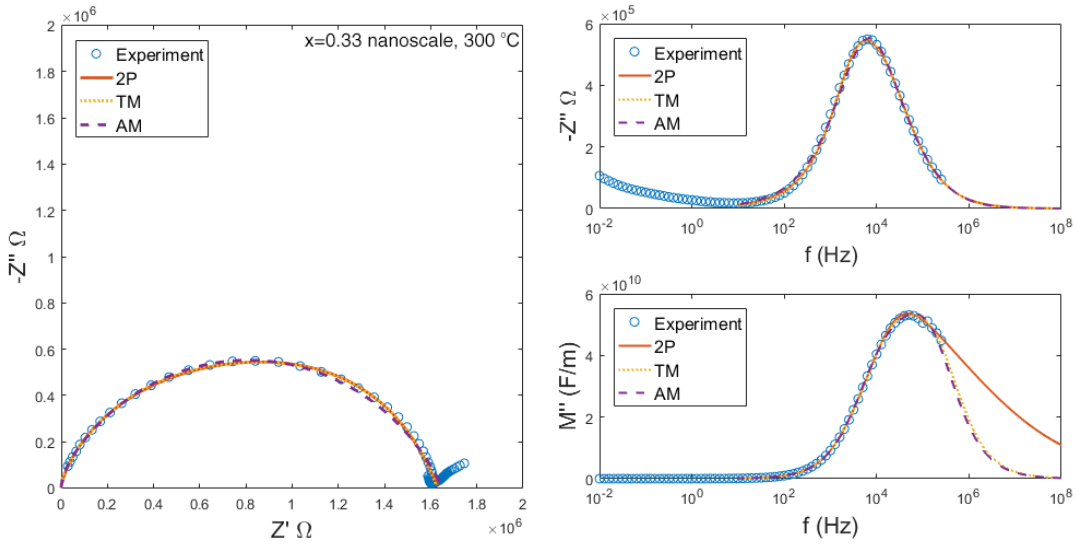

Figure 2.11: Combined Nyquist, imaginary impedance (-Z") semi-log, and imaginary modulus (M") plot of x = 0.50, micron sample at 300°C. The benchmark 2P model also predicted a large high-frequency M" tail while the TM and AM models still captured the relaxation behavior more properly.

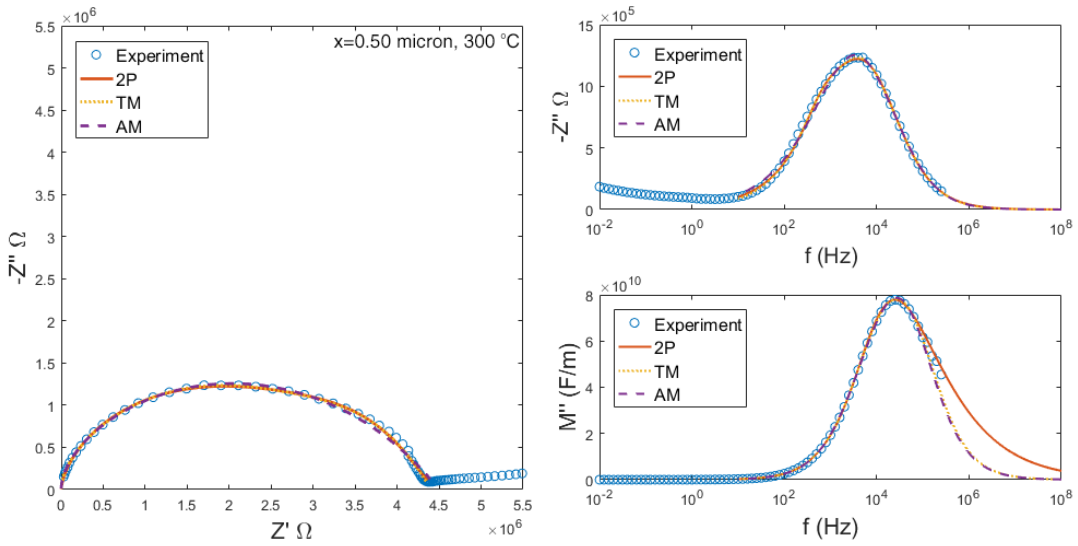

Figure 2.12: Combined Nyquist, imaginary impedance (-Z") semi-log, and imaginary modulus (M") plot of x = 0.33, nanoscale sample at 300°C. The benchmark 2P model predicted a large high-frequency M" tail while the TM and AM models captured the relaxation behavior more properly.

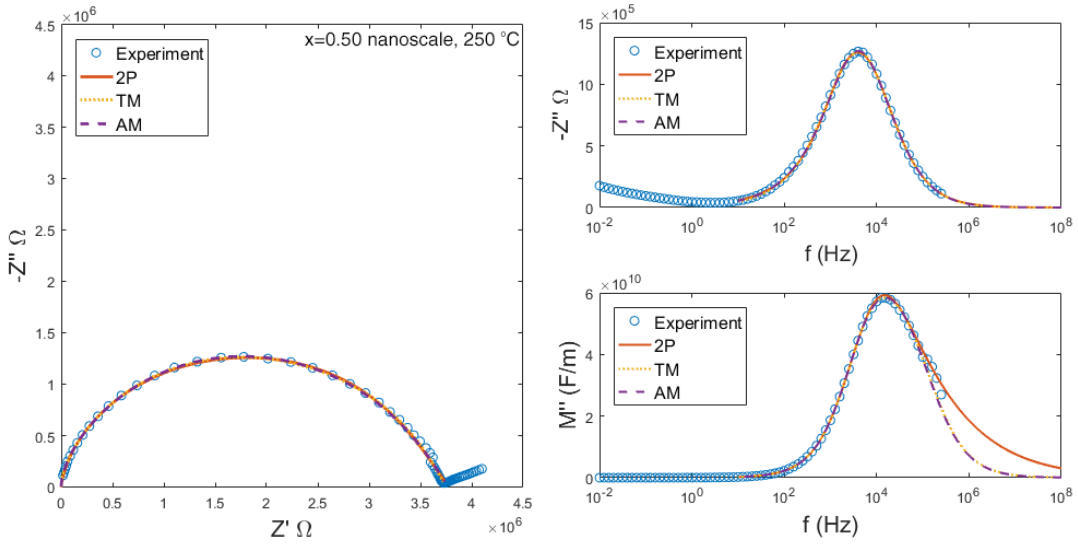

Figure 2.13: Combined Nyquist, imaginary impedance (-Z") semi-log, and imaginary modulus (M") plot of x = 0.50, micron sample at 300°C. The benchmark 2P model also predicted a large high-frequency M" tail while the TM and AM models still captured the relaxation behavior more properly.

Table 2.2: Fitted 2P model parameters for selected samples.

Parameters (2P)	x = 0.33 nanoscale 300 °C	x = 0.50 micron 300 °C
R_g (MΩ)	1.29 ± 0.03	3.93 ± 0.04
C_g (pF)	2.01 ± 0.03	3.42 ± 0.04
Q_g (nF s^{1-n})	0.51 ± 0.06	0.92 ± 0.06
n	0.64 ± 0.01	0.53 ± 0.01
R_{gb} (MΩ)	0.35 ± 0.02	0.52 ± 0.03
C_{gb} (nF)	0.14 ± 0.01	0.45 ± 0.03

Table 2.3: Fitted TM model parameters for selected samples. Notice that $R_g > R_{gb}$ and $R_g > R_{int}$.

Parameters (TM)	x = 0.33 nanoscale 300 °C	x = 0.50 micron 300 °C
R_g (MΩ)	1.38 ± 0.02	3.91 ± 0.03
R_{gb} (MΩ)	0.25 ± 0.02	0.50 ± 0.02
R_{int} (MΩ)	0.28 ± 0.02	0.80 ± 0.04
Q_{block} (nF s^{1-n})	0.18 ± 0.02	0.41 ± 0.03
n	0.71 ± 0.01	0.61 ± 0.01
C_{gb} (nF)	0.14 ± 0.02	0.39 ± 0.03
C_{all} (pF)	5.47 ± 0.05	4.14 ± 0.02

Table 2.4: Fitted AM model parameters for selected samples. Notice that $R_{all} > R_{int}$.

Parameters (AM)	x = 0.33 nanoscale 300 °C	x = 0.50 micron 300 °C
R_{all} (MΩ)	1.65 ± 0.02	4.49 ± 0.02
R_{int} (MΩ)	0.29 ± 0.02	0.79 ± 0.06
Q_{block} (nF s^{1-n})	0.34 ± 0.03	0.76 ± 0.05
n	0.67 ± 0.01	0.56 ± 0.01
C_{all} (pF)	5.57 ± 0.06	4.19 ± 0.04

The obtained physical parameters corresponding to the 2P, TM, and AM models are compiled in Table 2.2, 2.3, and 2.4 respectively. From these values, it can also be observed that the order of magnitude of the capacitance values agrees with the corresponding microstructural assignment given to them. For example, in x = 0.33 nanoscale sample, the TM model has C_{all} = 5.62 ± 0.05 pF while in the AM model, C_{all} = 5.57 ± 0.06 pF. This is expected since C_{all} comes originally from the effective grain capacitance, where 10^{-12} F is expected for grain contributions. The same evidence can be found for the effective grain boundary contribution; the capacitance value C_{gb} were found in the order magnitude of 10^{-10} F, as expected for grain boundaries.

In addition, the TM model passes the two hypothesis tests proposed in Section 3.2. These two hypotheses will be mentioned briefly again and discussed in detail. The first hypothesis states that the effective grain resistance will be higher than the other resistances at lower temperatures. The evidence comes from Table 2.3 and Table 2.4, both of which compile the physical parameters for the TM and AM models respectively. From there, it is very much evident that the grain resistance R_g is consistently lower. As an example, x = 0.33 nanoscale sample has an effective grain resistance R_g = 1.38 ± 0.02 MΩ which is larger than the effective grain boundary resistance R_{gb} = 0.25 ± 0.02 MΩ and the discontinuous conduction pathways resistance R_{int} = 0.28 ± 0.02 MΩ.

A reduction of one order of magnitude is quite significant and provides more evidence of the dispersed ionic conductor phenomena in the samples. Suppose that no prior assumption on dispersed ionic conductivity is made, then the resistances associated with the interfaces and grain boundaries are expected to be higher than the grains, which occupies the bigger volume of charge carriers and therefore provides the main action for the conduction. But now with the dispersed ionic conductor assumption, the TM model explicitly represents the faster interfacial conduction pathways, in which their origins rely on thermodynamics, and visualize the interplay of two phases concretely in the form of a consistently lower R_{int}.

The second hypothesis is that the energy barrier or activation energy for conduction in normal grain/grain boundary pathways is higher than those with the

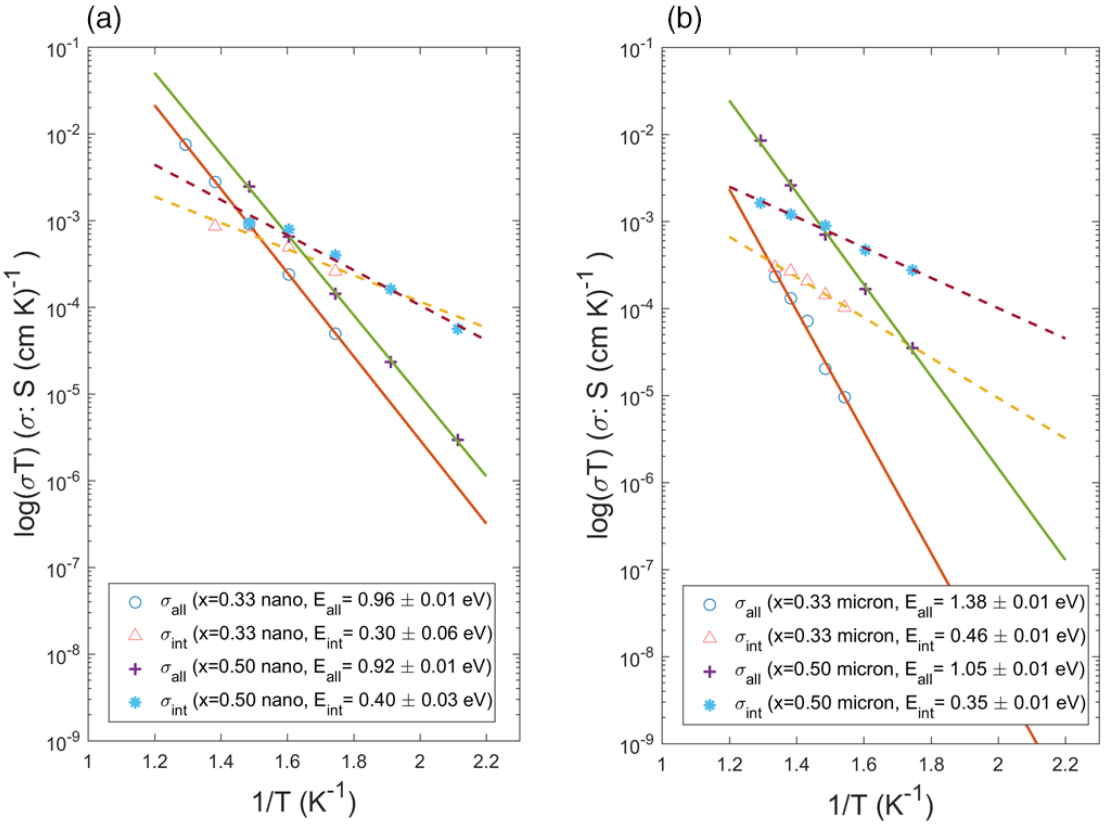

Figure 2.14: (a) Arrhenius plot with the AM model for the nanoscale samples. (b) Arrhenius plot with the AM model also for the micron samples. All samples follow the relationship $E_{all} > E_{int}$.

insulator-conductor interfaces. In order to prove this, the Arrhenius plots can be used as evidence. Fig. 2.14.a. shows the Arrhenius plot for the nanoscale samples while Fig. 2.14.b shows the Arrhenius plot for the micron samples. All samples exhibited lower activation energies for the interfacial insulator/conductor conductivity. Using x = 0.50 nanoscale sample as an example, the combined activation energy E_{all} = 0.92 ± 0.01 eV while the interface activation energy for the discontinuous pathways E_{int} = 0.40 ± 0.04 eV. Furthermore, the crossover temperature can also be observed, indicating that the regular conduction pathway is more dominant at temperatures higher than 400 ^{o}C. Another example can be taken from x = 0.33 micron, where the combined activation energy E_{all} = 1.38 ± 0.01 eV while the interface activation energy for the discontinuous pathways E_{int} = 0.46 ± 0.04 eV.

Table 2.5: Conductivity values for the combined grain and grain boundary (σ_{all}) and insulator/conductor interface (σ_{int}).

Samples	T (K)	σ_{all} ($\mathrm{S\,cm^{-1}}$)	σ_{int} ($\mathrm{S\,cm^{-1}}$)	Ratio (nanoscale/micron)
x = 0.33 micron	673	$3.01{\cdot}10^{-8}$	$2.13{\cdot}10^{-7}$	45 (for σ_{all})
x = 0.33 nanoscale	673	$1.35{\cdot}10^{-6}$	$1.23{\cdot}10^{-6}$	6 (for σ_{int})
x = 0.50 micron	573	$6.11{\cdot}10^{-8}$	4.81 10-7	23 (for σ_{all})
x = 0.50 nanoscale	573	$1.44{\cdot}10^{-6}$	$4.01{\cdot}10^{-6}$	8 (for σ_{int})

A related evidence for conductivity enhancements can be found in Table 2.5, which compiled conductivity values for the combined grain and grain boundary conduction σ_{all} and the interfacial conduction σ_{int} at selected temperatures, extracted with the AM model. For σ_{all}, the nanoscale samples exhibit 20 to 45 times better conductivity than the micron samples. The comparison for σ_{int} is also very compelling; the nanoscale samples exhibit 5 to 8 times better interfacial conductivity than the micron samples. This shows that parameters involving grain, grain boundary, and conductor/insulator interface within the newly proposed models can capture the effects of high-energy planetary milling and amorphous nanosilica effectively.

It is important also to compare the activation energy values with current literature values on similar dispersed ionic conductor systems and lithium borate conductors. Table 2.6 compiles literature values of activation energies and conductivities for Li-ion-containing phases in the lithium borate/silica composites investigated in this work [61,62]. It is worth noting that sample preparations made in the Ref. [62] closely resemble this works preparation (pellet-sized samples, sintering temperature, precursors), making the comparison fair and accurate. In comparison to E_{all} obtained in this work, these literature values are consistently higher but lower compared to E_{int}. Furthermore, the conductivity values obtained in this work (as seen in Table 4) lie in between the amorphous and crystalline conductivity values for each composition, where the polycrystalline materials have lower conductivities. This brief comparison of the conductivity values and activation energies with corresponding singe-phase studies suggests that that the polycrystalline lithium borate/silica composites made in this work achieved a characteristic that is between the amorphous and crystalline lithium borate for each composition being made.

Table 2.6: Literature values for activation energies and conductivity values for each phase present in this works composites. It should be noted that most of the literature activation energies are lower than the calculated E_{all} but higher than E_{int}.

Li-ion Conductors	E_a (eV)	σ ($\mathrm{S\,cm^{-1}}$)	T (K)	Ref.
$Li_2Si_2O_5$, crystalline	1.37	$6.8{\cdot}10^{-8}$	673	[61]
Li_2SiO_3, crystalline	0.92	$3.0{\cdot}10^{-6}$	673	[61]
$LiBO_2$, crystalline	1.37	$2.4{\cdot}10^{-9}$	573	[62]
$LiBO_2$ $(0.50Li_2O - 0.50B_2O_3)$ amorphous	0.49	$8.6{\cdot}10^{-4}$	573	[62]
$Li_2B_4O_7$, crystalline	1.18	$5.8{\cdot}10^{-7}$	673	[62]
$Li_2B_4O_7$, $(0.33Li_2O - 0.67B_2O_3)$ amorphous	0.69	$2.6{\cdot}10^{-4}$	673	[62]

Table 2.7 (see page 32 compiles literature values of activation energies and highest conductivity value in various Li-ion dispersed ionic conductors. The interface activation energy of the discontinuous conduction pathways E_{int} are comparable with $LiI - Al_2O_3$ [1], perovskite $Li_{0.5}La_{0.5}TiO_3 - SiO_2$ [29], and $Li_2MnCl_4 - CeO_2$ [63]. For the literature values that follow E_{int}, the studies were conducted at a wide range of insulator concentrations. Therefore, an optimal insulator concentration, activation energy, and ionic conductivity were obtained. The exceptions to these are $Li_3PO_4 - Al_2O_3$ [64], which is closer to E_{all}, and $Li_2SO_4 - Al_2O_3$ [30]. For the study conducted on $Li_3PO_4 - Al_2O_3$, only one composition was explored and hence no indication of whether the conductivity enhancement was at its optimum. Furthermore, the conductivity of $Li_2SO_4 - Al_2O_3$ in the study was found to be dominated by protons instead, excluding it from comparison with this works lithium borate/silica composites.

By excluding the exceptions, a trend can be observed where an activation energy closer to 0.50 eV is correlated with a material at an optimum concentration of insulator. It will then be beneficial to rigorously study lithium borate/silica composites with a wider insulator composition range to observe how activation energy and conductivity changes, and see whether the same correlation to optimal values can be obtained for the lithium borate/silica composites.

Table 2.7: Activation energies for various Li-ion dispersed ionic conductors. The literature values agree with the activation energy of the discontinuous interface pathways, which is at 0.35-0.40 eV. The exception to this rule is either due to *presence of proton conduction or **an investigation of only one composition, leaving the optimal concentration undetermined.

Dispersed Ionic Conductors	E_a (eV)	σ (S cm^{-1})	T (K)	Composition	Ref.
$LiI - Al_2O_3$	0.43	$1.00{\cdot}10^{-5}$	298	33-45 mol%	[1]
$Li_{0.5}La_{0.5}TiO_3 - SiO_2$	0.41	$7.50{\cdot}10^{-5}$	303	5 vol%	[29]
$Li_2SO_4 - Al_2O_3$	1.36*	$1.00{\cdot}10^{-2}$	773	18 mol%	[30]
$Li_2MnCl_4 - CeO_2$	0.5	$2.00{\cdot}10^{-3}$	473	10 mol%	[63]
$Li_3PO_4 - Al_2O_3$	1.07**	$1.00{\cdot}10^{-5}$	667	48-46 vol%	[64]

2.5 Summary

Two-phase materials consisting of 40 wt% SiO_2 with $x \cdot Li_2O + (1 - x) \cdot B_2O_3$ $x = 0.33, 0.50$ were successfully synthesized through a multi-step ceramic fabrication process, differentiated based upon the intensity of the milling/particle size reduction process (micron or nanoscale). From phase analysis, samples with $R = 0.5$ or $x = 0.33$ closely resemble to the expected composite system while samples with $R = 1.0$ or $x = 0.50$ show more complex phase compositions. In addition, the microstructural data showed that the nanoscale samples contain a more homogeneous distribution of phases while the micron samples give a more uneven distribution, with some lithium borate rich phases isolated within the insulating silica-rich phase.

Fundamental knowledge regarding accurate conduction models is the key to realizing how composite ionic conductors may be used in future Li-ion conducting devices. Supported by the phase and microstructural characterizations, conduction models for composite ionic conductors were derived heuristically based on the theory of dispersed ionic conductors. This process yielded the TM model and its approximation, the AM model, which provided the means to properly analyze impedance spectroscopy data of dispersed/composite ionic conductor systems without the need to use percolation models. Results from impedance spectroscopy based on qualitatively observing the goodness and uniqueness of fit and comparing model parameters consistently proved the power of the new models. It is suspected based upon the model parameters comparisons with literature values of activation energies that the synthesized composite materials can be further optimized through compositional, microstructural, and phase control. Hence, future studies that span different silica weight percent will be crucial in understanding both the model and material better.

Chapter 3

Effective Medium Approximation of Composite Solid Electrolytes

In the preceding section, two heuristics models, the TM and AM models, were developed to analyze impedance spectra of dispersed ionic conductors. By explicitly considering parallel interfacial pathways that are blocked discontinuously by amorphous boundaries, the model was able to take account the frequency dispersion phenomena that were occurring in the lithium borate/silica composites. However, problems will occur if the TM and AM models are extended to model concentration and temperature behaviors, especially since none of the models were inherently percolating and microscopic mechanism of the space charge layers were not directly specified. This brings to the larger issue on the integrated mathematical modeling of dispersed ionic conductors. The recognized variables such as (1) insulator concentration, (2) temperature, and (3) frequency are usually treated separately, lacking the connection in between. Of the three variables, two of them (insulator concentration and frequency) are intimately linked at the macroscopic level.

In this chapter, a framework is developed to derive frequency-domain effective medium approximation (EMA) models for a composite material with an arbitrary number of components. In Section 3.1, *the random AC network* is derived by discretizing continuum electrodynamics equations for inhomogeneous media. In addition, the *lattice Green's function* is introduced and its role in calculating conductivities inside a

homogeneous network of impedances is discussed. In Section 3.2, the simplest version of the EMA known as the *single-bond* EMA is derived by a combination of the heuristics approach proposed by Kirkpatrick [65] and the lattice Green's function developed previously.

In Section 3.3, the mathematical features of the single-bond EMA derived for the composite material are discussed, which has the form of a *polynomial*. Using the two-component system as an example, an emphasis is made in the role of the coefficients and discriminant of the polynomial in determining the percolating behavior of a composite material. Afterwards, the polynomials for a 3- and 4-component system are developed. Analytical solutions for the DC case and low-frequency case were also developed for the 2-, 3-, and 4- component systems. Finally, Section 3.4 will introduce the application of the three-component system to model dispersed ionic conductors. Developments from the 'continuum percolation' model of dispersed ionic conductors [3] are combined together to synthesize the full AC extension. Its utility in non-linear regression analysis of dispersed ionic conductors and analyzing the material's percolating behavior is presented for literature data on the classic system $LiI - Al_2O_3$ with accompanying parametric studies of the impedance spectra at different volume fractions.

3.1 Derivation of the Random AC Network

As a form of lattice models, percolation-based models must be derived under an appropriate framework or physical theory. In the context of conductivity and transport, the effective medium approximation of percolation-based models have been formulated through a number of different physical theories that fall between either (1) stochastic-based transport theories, governed by a master equation for random walks on a lattice [66–69], or (2) electrodynamics-based theories, governed by the Maxwell's equations both in a continuum and a lattice space [65,70–72]. Interestingly, both types of theories will yield an identical result in the DC conductivity case. On the other hand, a stochastic-based transport theory will yield a completely different result for the AC or frequency-domain case as a result of frequency-dependence of a random

walk on a lattice[1]. The subtle difference in both types of theories is taken for granted when modeling DC conductivity of dispersed ionic conductors, as observed from the variety of EMA scheme proposed in literature [3, 4, 43–47]. The lack of recognition of this difference forms the uncertainty that impedes the frequency-domain extension of the percolation-based models of composite solid electrolytes.

It should be natural that the conductivity and permittivity of composite materials are governed by continuum electrodynamics or Maxwell's equations. In fact, it is often the norm to use Maxwell's equations in describing the electromagnetics of an inhomogeneous medium, either through finite element analysis or homogenization theory. Therefore, it is desirable to derive percolation models that have direct correspondence from those equations. In this section, the transformation of continuum electrodynamics equations to its collapsed lattice form is given as rigorous justification of using percolation models to describe the composite material. This transformation procedure will also be used to introduce the lattice Green's function in the context of calculating the conductivity between two points of an infinite impedance network; an important procedure in formulating the EMA for composite materials.

3.1.1 Correspondence of Continuum and Lattice Model

Consider an isotropic linear composite material sitting in an $\mathbb{R}^n$ (N-dimensional) space and is composed of M-many components such as a conductor, insulator, space charge layers, grain boundaries, etc. As a composite material, its long-range DC conductivity σ_∞ and permittivity ε will locally vary as a function of position vector $\mathbf{r}$. There are several relevant electrodynamics equations that is used to describe its electrical properties. Using the usual notation:

$$\nabla \cdot \mathbf{D}(\mathbf{r}, t) = \rho(\mathbf{r}, t) \tag{3.1}$$

$$\nabla \cdot \mathbf{J}(\mathbf{r}, t) + \frac{\partial \rho(\mathbf{r}, t)}{\partial t} = 0 \tag{3.2}$$

$$\mathbf{J}(\mathbf{r}, t) = \sigma_\infty(\mathbf{r})\mathbf{E}(\mathbf{r}, t) \tag{3.3}$$

$$\mathbf{D}(\mathbf{r}, t) = \varepsilon(\mathbf{r})\mathbf{E}(\mathbf{r}, t) \tag{3.4}$$

[1]This difference and the appropriateness of one theory over the other in modeling composite materials is discussed in Section 3.2

where these equations correspond to Gauss' Law, the continuity equation, and the constitutive relations respectively. It should be noted that the displacement field $\mathbf{D}$ is formulated to include polarization effects in the term, i.e. $\varepsilon(\mathbf{r}) = \varepsilon_0(1+\chi_e(\mathbf{r}))$, where χ_e is the material's susceptibility. The notation for the long-range DC conductivity σ_∞ has the 'infinity' subscript to separate it from the more general complex conductivity $\hat{\sigma}$, which would have relative permittivity incorporated within its expression.

In frequency domain, all four equations can be expressed in phasor form:

$$\nabla \cdot \tilde{\mathbf{D}}(\mathbf{r}) = \tilde{\rho}(\mathbf{r}, t) \tag{3.5}$$

$$\nabla \cdot \tilde{\mathbf{J}}(\mathbf{r}) + j\omega\tilde{\rho}(\mathbf{r}) = 0 \tag{3.6}$$

$$\tilde{\mathbf{J}}(\mathbf{r}) = \sigma_\infty(\mathbf{r})\tilde{\mathbf{E}}(\mathbf{r}) \tag{3.7}$$

$$\tilde{\mathbf{D}}(\mathbf{r}) = \varepsilon(\mathbf{r})\tilde{\mathbf{E}}(\mathbf{r}) \tag{3.8}$$

Applying an electric field with known potential $\tilde{E} = -\nabla\phi$, all four equations can be collapsed into a single equation which is equivalent to Kirchhoff's AC current law in differential form:

$$\nabla \cdot (\hat{\sigma}(\mathbf{r})\nabla\phi(\mathbf{r}, \omega)) = 0 \tag{3.9}$$

$$\hat{\sigma}(\mathbf{r}) = \sigma_\infty(\mathbf{r}) + j\omega\varepsilon(\mathbf{r}) \tag{3.10}$$

By the divergence theorem, the differential form can be transformed into the integral form:

$$\iiint_V \nabla \cdot (\hat{\sigma}(\mathbf{r})\nabla\phi(\mathbf{r}, \omega))\ \mathrm{d}V = \oiint_S (\hat{\sigma}(\mathbf{r})\nabla\phi(\mathbf{r}, \omega) \cdot \mathbf{n})\ \mathrm{d}S = 0. \tag{3.11}$$

Formulating Eq. 3.10 in a closed surface integral form helps to understand its role as a statement of charge conservation. The following discretization procedure will be done for the integral form, although the result will in fact be equivalent when done in the differential form.

Consider an arbitrary discretization of the continuum Kirchhoff's current law in integral form. Because it is a closed surface integral, the discretization can be interpreted as partitioning the closed surface into z-many different surfaces. If $z = 2N$, then the discretization formally follows an N-dimensional cube partitioning of the

space with lattice spacing a. Suppose that i signifies one arbitrary node in the lattice, Eq. 3.11 will be discretized in the following way:

$$\oiint_S (\hat{\sigma}(\mathbf{r})\nabla\phi(\mathbf{r},\omega)\cdot\mathbf{n})\ \mathrm{d}S \approx \sum_{j=0}^{z} \hat{\sigma}_{i,j}\left(\frac{\phi_j-\phi_i}{a}\right)a^2 \tag{3.12}$$

where subscript j is the nearest neighbour of the node i, and each summation term in Eq. 3.12 represents a surface integral being performed in one surface of the N-dimensional cube. Setting Eq. 3.12 to equal to zero and dividing LHS as well as RHS by a, Kirchhoff's (AC) current law for a discretized composite material can be obtained:

$$\sum_{j=0}^{z} \hat{\sigma}_{i,j}(\phi_j-\phi_i) = 0 \tag{3.13}$$

$$\hat{\sigma}_{i,j} = \sigma_{i,j}^{\infty} + j\omega\varepsilon_{i,j} \tag{3.14}$$

The Kirchoff's current law in this particular form can be found in Kirkpatrick's seminal work on percolation and conduction [65] for the DC case, although full derivation was not entirely given like the preceding paragraphs. Fig. 3.1 visualizes the short mathematical manipulation that was done to produce Eq. 3.13. Essentially, the previous discretization procedure starts from a continuum version of the composite material and transform it into a network of conducting bonds. Each bond will have a circuit element corresponding to the complex conductivity $\hat{\sigma}_{i,j}$ at that given location. The value of this circuit element will be randomly distributed throughout all possible conductivity values that the material can have locally. And thus, the simple mathematical manipulation gives rise to a *random AC network* [8]. The DC case is commonly referred in the literature as the random resistor network (RRN).

Interestingly, each discretized surface represents one flow of current from a given node which implies that the partitioning of the surface will influence the *topology* of the resultant network. Such feature can only occur when discretizing the integral. Thus, the main question is what type of lattice or number of discretized surfaces is the most suitable? Or equivalently, what network topology will best represent the physical, continuum reality of composite materials? From this derivation and at the

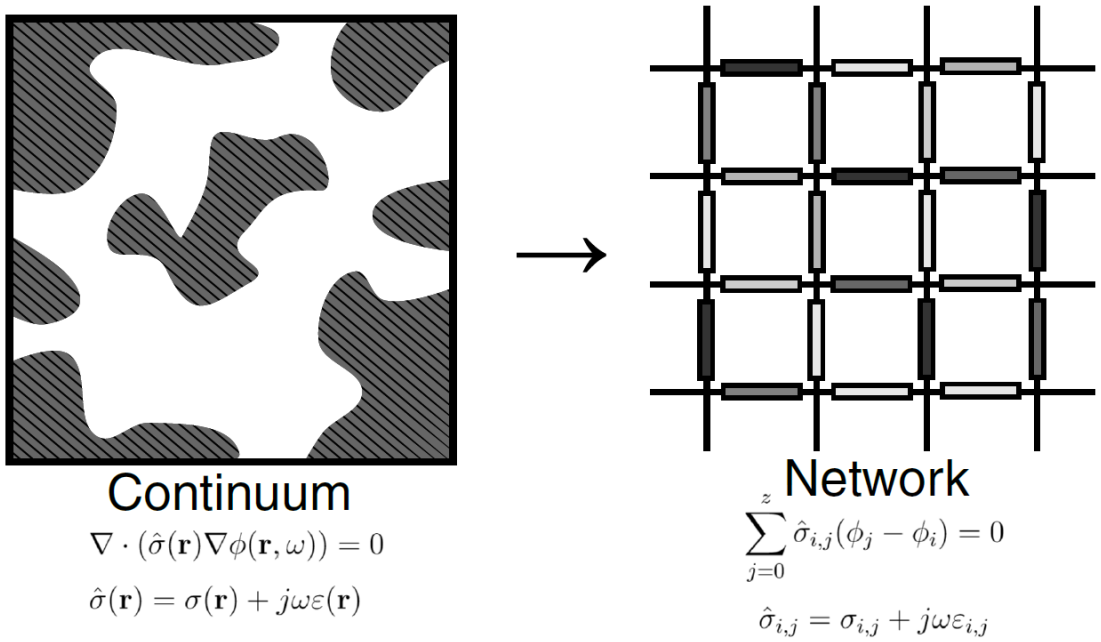

Figure 3.1: An illustration of the discretization process. A continuum formulation of the composite material problem is discretized to produce a network of randomly distributed conductivity bonds. Kirchhoff's law is the main equation that described both the continuum and network.

most conservative interpretation, a *simple cubic* ($z = 6$) network is appropriate since it corresponds directly to the finite difference scheme in 3D space. However, this does not imply that the EMA cannot be done in different lattices. To keep things as general as possible, the EMA will be performed by assuming an arbitrary topology of the network.

3.1.2 Lattice Green's Function

Just like the Green's function is helpful in solving ordinary and partial differential equations, the lattice Green's function will also be helpful in solving difference equations in lattice space. Its usage in the effective medium approximation of random resistor networks is ubiquitous, although how the Green's function is specifically used

will depend entirely upon the approach to derive the EMA scheme[2]. This section will seek to present the lattice Green's function in the context of how it was first encountered on solving resistances (more generally, impedances) of an infinite electrical network [9, 73].

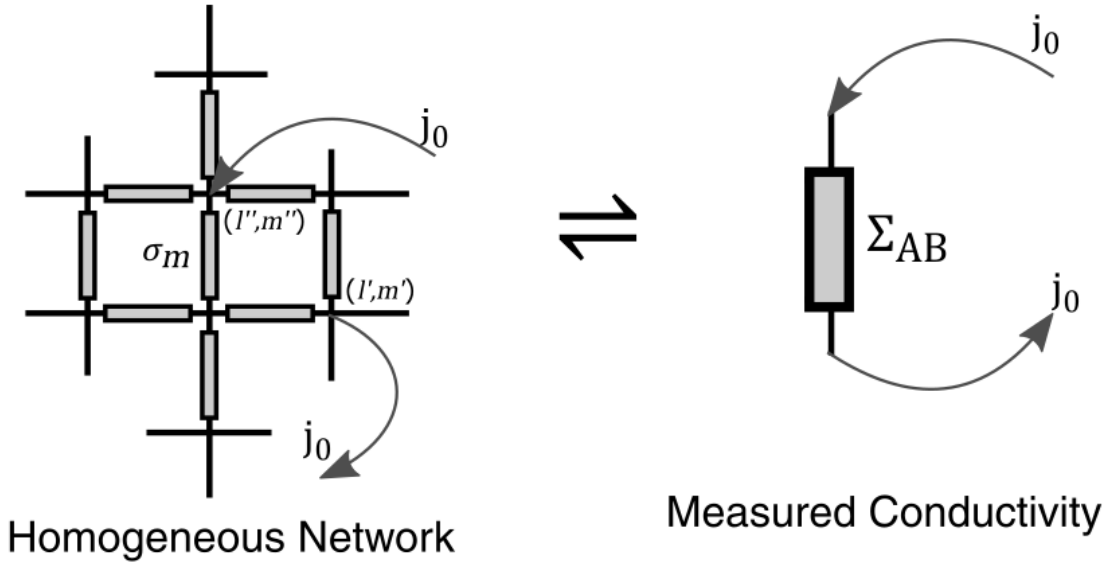

Figure 3.2: Illustration of the problem on measured conductivity. A current j_0 is introduced locally at some position and extracted at another point. The goal is to derive an expression for the measured conductivity in between these two points Σ_{AB} as a function of the network topology.

For the sake of simplicity, the case that is being considered is the 2D square lattice although it can be generalized to any dimension and network topology. The illustration of the problem can be found in Fig. 3.2. Suppose that a current j_0 is introduced locally inside the homogeneous network at position **A** with coordinates $\{l', m'\}$ in the network and extracted again at position **B** with coordinates $\{l'', m''\}$, which may be any point outside of A. What would be the total conductivity measured between these two points?

Firstly, one must start with the continuum Kirchhoff's law in differential form, instead of the integral form, and formulate its discretized form for a *homogeneous*

[2]The approaches used in formulating the effective medium approximation and the relation of each to the lattice Green's function will be discussed more in-depth in Section 3.2

network with conductivity $\hat{\sigma}_d$:

$$\hat{\sigma}_d(\nabla_h^2\phi_{(l,m)}) = 0 \tag{3.15}$$

where ∇_h^2 denotes the discrete Laplace operator, $\hat{\sigma}_d$ is the uniform conductivity in the network, and $\phi_{l,m}$ is the potential at node $\{l,m\}$. The discrete Laplace operator can actually be found by simply setting Eq. 3.15 to the discretized integral form, which is Eq. 3.13. However, the present mathematical notation of Eq. 3.13 is not based upon set coordinate location. To have the discrete Laplace operator formulated in terms of set coordinate location, it can be defined using the finite difference scheme, generalized in the N-dimensional space. With the 2D square lattice, the discrete Laplace operator is essentially:

$$\begin{aligned}(\nabla_h^2\phi_{(l,m)}) =& \frac{[\phi_{(l+1,m)} - \phi_{(l,m)}] + [\phi_{(l-1,m)} - \phi_{(l,m)}]}{a^2} \\ &+ \frac{[\phi_{(l,m+1)} - \phi_{(l,m)}] + [\phi_{(l,m-1)} - \phi_{(l,m)}]}{a^2}\end{aligned} \tag{3.16}$$

The operator in its explicit form will not be used in subsequent discussion, but it is beneficial to keep in mind.

Now, the set $\{s', q'\}$ is defined as the location difference or 'distance' between point **A** and **B**, i.e. $\{s', q'\} = \{l'' - l^{'} -, m'' - m^{'}\}$. Eq. 3.15 can be used to solve the problem by using a superposition argument illustrated in Fig. 3.3 (see page 42). According to the superposition argument, the local current j_0 can be found by considering two fictitious cases. Case (1) is a current j_0 that is introduced at **A** and extracted at "infinity" and case (2) is a current j_0 introduced at "infinity" and extracted at **B**. As far as Eq. 3.15 or Kirchhoff law is concerned, the two fictitious cases are a form of charge conservation violation and it transform Eq. 3.15 into the following,

$$\text{for case (1):} \quad \hat{\sigma}_d(\nabla_h^2\phi_{(l,m)}) = j_0\delta_{(l,m);(l',m')} \tag{3.17}$$

$$\text{for case (2):} \quad \hat{\sigma}_d(\nabla_h^2\phi_{(l-s',m-q')}) = -j_0\delta_{(l,m);(l',m')} \tag{3.18}$$

where $\delta_{(l,m);(l',m')}$ is the Kronecker delta for the 2D square lattice. The Kronecker delta is used to express the situation that current conservation is violated at *only* point **A** for case (1) and point **B** in case (2), but it won't be the case anywhere else.

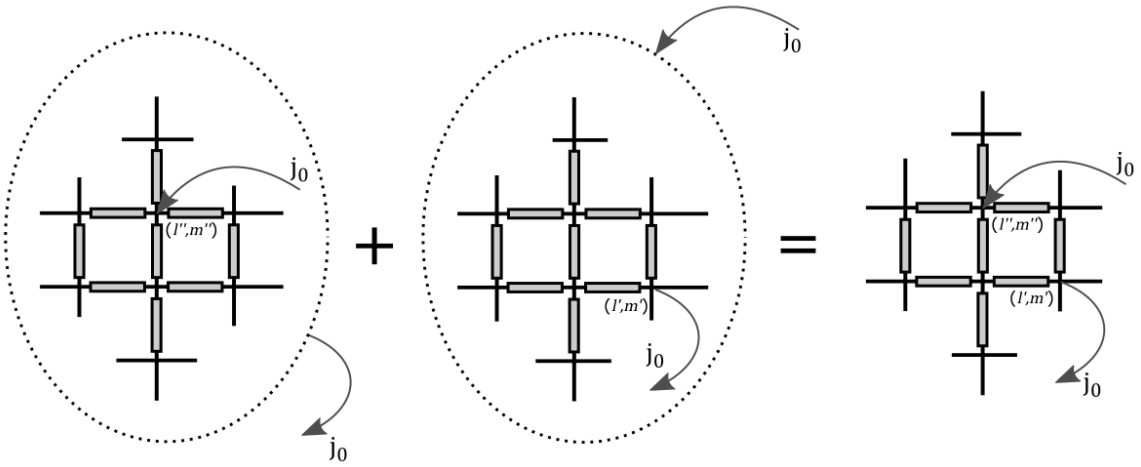

Figure 3.3: Illustration of the superposition argument. Two fictitious cases are considered, where a current j_0 introduced and extracted at "infinity" (dashed boundary) can be found. The summation of contributions in these two cases will correspond to the physical case (right), where current at "infinity" cancels each other.

Because conductivity won't be measured at "infinity", the Kronecker delta for current at infinity is not introduced. Also, notice that Eq. 3.18 is modified to make use of translational invariance in the lattice.

For simplicity, the subscript $k' = (l', m')$ is used to express position at point **A**. Now, both equations may be subtracted to yield the following collapsed difference equation:

$$\hat{\sigma}_d(\nabla_h^2 \Phi_{(l,m);k'}) = -2j_0\delta_{(l,m);k'} \tag{3.19}$$

where $\Phi_{(l,m);k'} = \phi_{l-s',m-q'} - \phi_{l,m}$ is the measured potential difference between point **A** and **B**. Notice that the Eq. 3.19 looks very similar to the formulation of the Green's function for the continuum Laplace operator:

$$\nabla^2 G(\mathbf{r}, \mathbf{r}') = -\delta(\mathbf{r} - \mathbf{r}') \tag{3.20}$$

where G is the Green's function and $\delta(\mathbf{r} - \mathbf{r}')$ is the Dirac delta. This correspondence implies the existence an equivalent concept of *lattice Green's function* $G_{(l,m);k'}$ in the network. Thus, the lattice Green's function can be defined similarly like the

continuum case using the discrete Laplace operator:

$$\nabla_h^2 G_{(l,m);k'} = -\delta_{(l,m);k'} \tag{3.21}$$

by further comparing term-by-term between Eq. 3.19 and Eq. 3.21, and defining the measured conductivity between points **A** and **B** as $\Sigma_{AB} = j_0/\Phi_{(l,m);k'}$, a concise equation can be obtained:

$$\Sigma_{AB} = \frac{\hat{\sigma}_d}{2G_{(l,m);k}} \tag{3.22}$$

With methods of operational calculus, the closed-form expression of the lattice Green's function problem can be found for the 2D square lattice [73]. If point **A** is at the origin, i.e. $k' = (0, 0)$ then the lattice Green's function is:

$$G_{(l,m)} = \frac{1}{2}(-1)^{m+n+1} \int_0^\infty e^{-2t}(I_0(t)I_0(t) - I_m(t)I_n(t))dt \tag{3.23}$$

where $I_n(t)$ is the modified Bessel function of the first kind. In 3D simple cubic lattice, where the location of a node is specified by the set coordinate $\{l, m, n\}$, the lattice Green's function is expressed as:

$$G_{(l,m,n)} = \frac{1}{2}(-1)^{l+m+n+1} \int_0^\infty e^{-3t}(I_0(t)I_0(t)I_0(t) - I_l(t)I_m(t)I_n(t))dt \tag{3.24}$$

where the subscript k' is dropped to imply that the problem is now fixed at the origin.

For the 2D square lattice, computing the values of the Green's function has been solved analytically by van der Pol [73] and the result is presented graphically in Fig. 3.4. Notice that the Green's function value for the nearest neighbours of the origin $G_{(0,1)} = G_{(1,0)} = G_{(0,-1)} = G_{(-1,0)} = \frac{1}{4}$. It can later be proven that the values of these nearest neighbor Green's function are dependent solely on the network topology:

$$G_{(1,0,\ldots,0)} = G_{(-1,0,\ldots,0)} = \ldots = G_{(0,\ldots,0,1)} = G_{(0,\ldots,0,-1)} = \frac{1}{z} \tag{3.25}$$

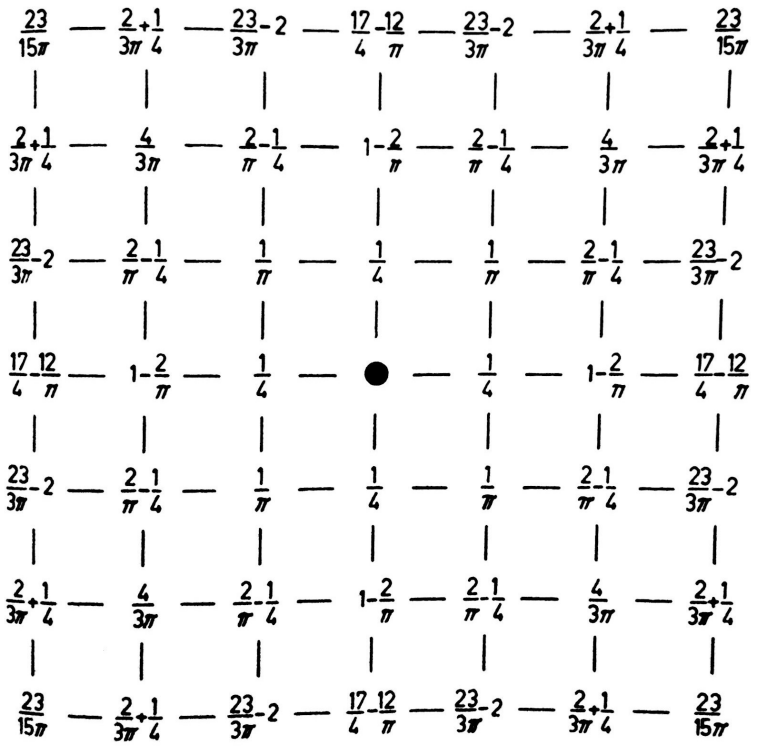

Figure 3.4: Values of 2D square lattice Green's function of the discrete Laplace operator ∇_h^2. Taken from Ref. [9].

This implies that if points A and B are nearest neighbours, Σ_{AB} for two nearest neighbours in an arbitrary network topology would be:

$$\Sigma_{AB} = \frac{z\hat{\sigma}_d}{2} \tag{3.26}$$

One of the most important point on this section is that the lattice Green's function, i.e. the closed-form expressions of Eq. 3.23 and Eq. 3.24, can be used independently of whether one is concerned with the original problem formulated in this section. This fact will be true in the formulation of the EMA scheme, where the approaches by different authors will use the lattice Green's function either in the same way as the original problem of this section or in a completely different way.

3.2 Effective Medium Approximation

Formulating the EMA can be done in various ways. In general, however, they may be divided into two approaches. The first approach is the *heuristics* approach, first done by Kirkpatrick [65, 74]. This method was inspired from classical treatments of mixtures, relied heavily upon symmetry arguments, and did not use the lattice Green's function. The second approach is the *bond Green's function* approach, first proposed by Ahmed and Blackman [75–79] This is the rigorous method to derive the EMA for percolation models, making use of the EMA's formal equivalence to coherent potential approximation (CPA) for substitutional alloys [80]. The derivation that shall be used in this section will be a mixture of both, relying upon the simplicity of the heuristics approach and the rigor of the Green's function method. Usage of the Green's function in deriving the EMA will also help in elucidating its strengths and weaknesses.

Suppose that there exists a *homogeneous* network in which each element in the network has a conductivity of $\hat{\sigma}_{\text{eff}}$. An electric field is applied to such network, which induces a voltage drop across it. Between nearest neighbors A and B, a voltage drop Φ_{eff} and a current j_m associated with it may be found. By Ohm's law:

$$\Phi_{\text{eff}} = \frac{j_{\text{eff}}}{\hat{\sigma}_{\text{eff}}}. \tag{3.27}$$

Now, a single impurity element/bond $\hat{\sigma}_0$ will replace the element between points A and B inside the homogeneous effective network as illustrated in Fig. 3.5. This impurity will originate from the random AC network that has been introduced to model the composite material, i.e. its conductivity is randomly distributed. This perturbs the homogeneous system and disrupts the original voltage drop Φ_{eff} between points A and B. To correct this effect, a local current j_0 will be introduced at point A and extracted at point B, in which the direction opposes the electric field. The voltage drop returns to normal and the impurity element will have the following relation through Ohm's law:

$$\Phi_{\text{eff}} = \frac{-j_0 + j_{\text{eff}}}{\hat{\sigma}_0} \tag{3.28}$$

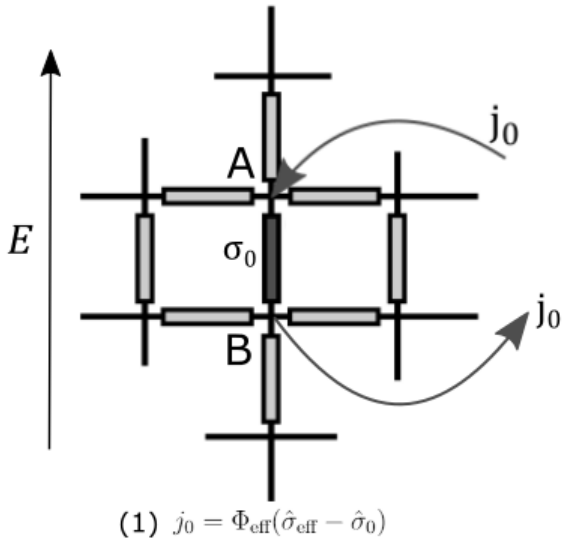

Figure 3.5: First step in the heuristics approach. A homogeneous network with a single impurity bond is applied an electric field. The disruption in voltage drop caused by the impurity is corrected by a local current j_0

By further combining Eq. 3.27 and 3.28, the following relation can be obtained:

$$j_0 = \Phi_{\text{eff}}(\hat{\sigma}_{\text{eff}} - \hat{\sigma}_0). \tag{3.29}$$

An important question to ask is, what was the extra local voltage drop Φ_0 caused by introducing the single impurity element before introducing j_0? To answer that question, the electric field that was used to induce the voltage drop in the network can be turned off leaving the local current j_0 as the only actor in the network. Now, the network can be collapsed into a parallel circuit, consisting of the impurity bond and the surrounding as illustrated in Fig. 3.6. It is clear that by Ohm's law

$$j_0 = (\Sigma_{AB}{}' + \hat{\sigma_0})\Phi_0 \tag{3.30}$$

This can then be substituted into Eq. 3.29 and combined with Eq. 3.27 to yield a closed-form expression for Φ_0:

$$\Phi_0 = \frac{\Phi_{\text{eff}}(\hat{\sigma}_{\text{eff}} - \hat{\sigma}_0)}{\hat{\sigma}_0 + \Sigma_{AB}{}'}. \tag{3.31}$$

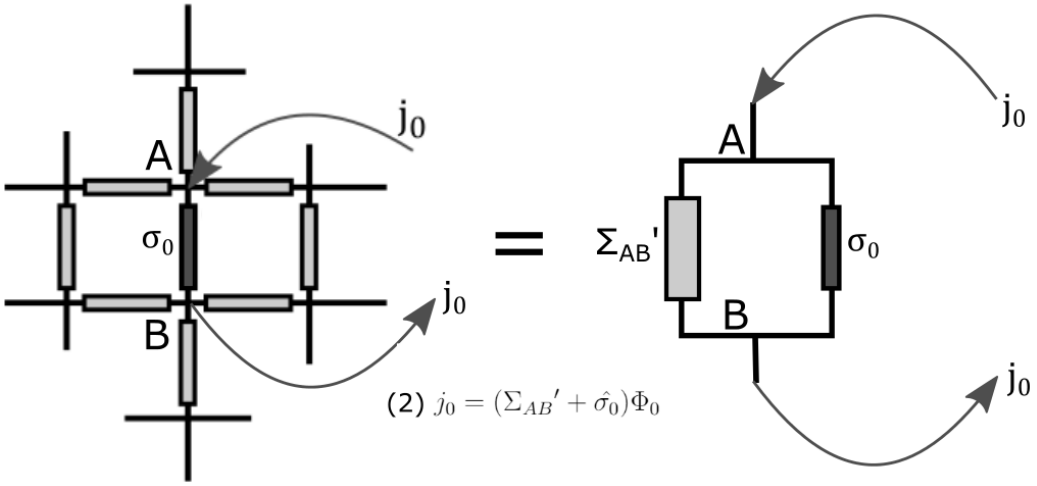

Figure 3.6: Second step in the heuristics approach. The electric field E was erased, leaving the local current to be the only contributor the voltage drop. The network was then collapsed into a parallel circuit consisting of the impurity and an equivalent impedance representing the medium surrounding the impurity

The next question to ask is, what is the expression for $\Sigma_{AB}{}'$? To answer this question, $\hat{\sigma}_0$ is momentarily replaced back with $\hat{\sigma}_{\text{eff}}$ so that the parallel circuit can be further collapsed into a single element Σ_{AB} but still keeping the local current j_0, as illustrated in Fig. 3.7. The connection between relationship Σ_{AB} and $\Sigma_{AB}{}'$ is easily expressed from elementary circuit theory:

$$\Sigma_{AB} = \Sigma_{AB}{}' + \hat{\sigma}_{\text{eff}} \tag{3.32}$$

From previous analysis on lattice Green's function, the expression for Σ_{AB} is known in terms of the value of the Green's function at the node of analysis and $\hat{\sigma}_{\text{eff}}$ (see Eq. 3.22). Setting point A as the origin and realizing that point B is the nearest neighbour from the origin, the expression for $\Sigma_{AB}{}'$ can be found as:

$$\Sigma_{AB}{}' = \left(\frac{1}{2G_{(1,0,\ldots,0)}} - 1\right)\hat{\sigma}_{\text{eff}} = \left(\frac{z}{2} - 1\right)\hat{\sigma}_{\text{eff}} \tag{3.33}$$

Equipped with Eq. 3.33, Eq. 3.31 can be now be expressed as

$$\Phi_0 = \frac{\Phi_{\text{eff}}(\hat{\sigma}_{\text{eff}} - \hat{\sigma}_0)}{\hat{\sigma}_0 + (z/2 - 1)\hat{\sigma}_{\text{eff}}} \tag{3.34}$$

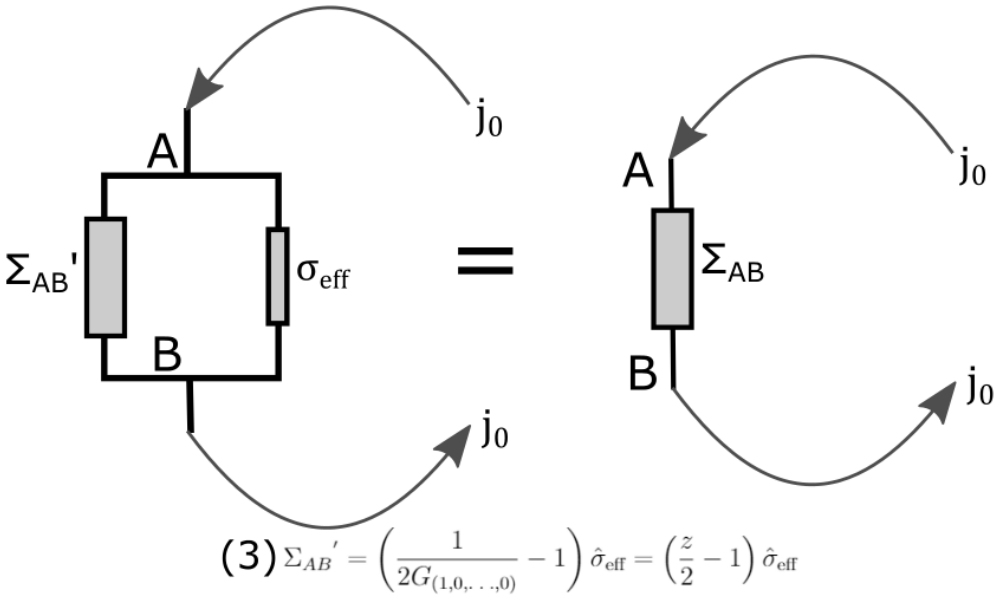

Figure 3.7: Third step in the heuristics approach. The conductivity surrounding the impurity, Σ'_{AB}, can be expressed using the lattice Green's function, as discussed previously.

Recall that the local current j_0 was introduced to make Φ_0 disappear. However, it is also known that $\hat{\sigma}_0$ takes in multiple different values due to the inhomogeneity of the composite material. A complex-valued probability distribution function (pdf) $f(\hat{\sigma})$ can be used to characterize all possible values of the local conductivity in the inhomogeneous material. Thus, with respect to the effective medium for composite materials, one component of a composite material can be taken as one 'microstate' of the 'statistical ensemble' governed by the pdf $f(\hat{\sigma})$[3]. Denoting angular brackets as the 'ensemble averaging' process, the goal now is to perform the following procedure:

$$\langle \Phi_0 \rangle_{\hat{\sigma}_0} = 0 \tag{3.35}$$

this condition is known as the *self-consistency* condition. An illustration of this step can also be found in Fig. 3.8. Imposing such condition will create the integral form

[3]The statistical physics analogy is used quite liberally in this case. However, it does illustrate the role of the probability distribution function as a way to define the microstates of the ensemble and *not* as some probability distribution governing how conductivity changes as a function of distance in the composite.

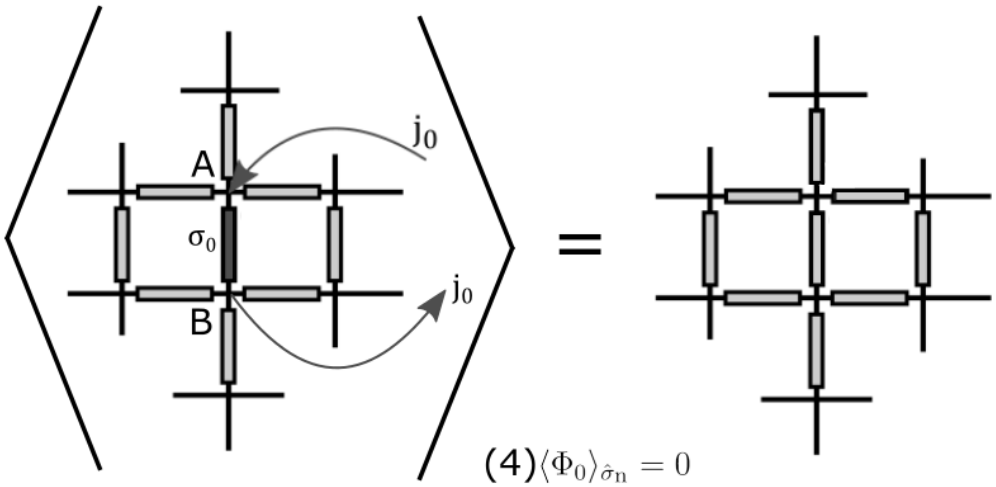

Figure 3.8: Fourth step in the heuristics approach. One value of conductivity that the impurity can take can be regarded as one 'microstate'. All configurations of the homogeneous network perturbed by the impurity form a 'statistical ensemble' that needs to be averaged to obtain the full effective medium back, expressed in terms of the impurity conductivities. Angular brackets indicate such averaging process.

of the *single-bond* EMA for the random AC network:

$$\int_{\Omega} f(\hat{\sigma}, P_1, P_2, \ldots, P_M) \frac{\hat{\sigma} - \hat{\sigma}_{\text{eff}}}{\hat{\sigma} + (z/2 - 1)\hat{\sigma}_{\text{eff}}} \, \mathrm{d}\hat{\sigma} = 0 \tag{3.36}$$

where $f(\hat{\sigma}, P_1, P_2, \ldots, P_M)$ simply implies that the pdf will also be a function of the volume fractions of each component in the composite material. The phrase single-bond refers to the usage of a a single impurity bond to perturb the effective medium.

To determine the simplest pdf for a composite material with M-many components, it can be realized that the total possible conductivity values or microstates of the ensemble are equal to the total number of components. Thus, $f(\hat{\sigma})$ can be represented as a sum of several Dirac delta distributions [4]:

$$f(\hat{\sigma}, P_1, P_2, \ldots, P_M) = \sum_{i=1}^{M} P_i \delta(\hat{\sigma} - \hat{\sigma}_i) \tag{3.37}$$

[4]The Dirac delta is not used like the Kronecker delta from the previous discussion on lattice Green's function, but it is used to simply transform the *continuous* probability distribution function to a discrete one since the number of microstates of the ensemble is now finite and countable

$$\text{where } \sum_{i=1}^{M} P_i = 1 \tag{3.38}$$

There is a slight mathematical problem. One may notice that formally speaking, the Dirac delta functions are only defined on real numbers and not the complex numbers. This fact is somewhat ignored in most treatments of the EMA. For the sake of completeness and rigor, the Dirac delta function on the complex plane can be simply defined by using Cauchy's integral formula:

$$\delta(z - z_0) = \frac{1}{2\pi i} \frac{1}{z - z_0} \tag{3.39}$$

$$g(z_0) = \frac{1}{2\pi i} \oint_{\Gamma} \frac{g(z)}{z - z_0} \, \mathrm{d}z \tag{3.40}$$

where $g(z)$ is any holomorphic function, i.e. analytic functions. This definition is consistent with complex-valued Dirac delta functions found in quantum field theory models and electrical engineering applications [81–83]. Eq. 3.36 is now defined as the contour integration on a complex plane, enclosing the complex conductivity of each component of the composite material in a complex plane. Applying this probability distribution, the algebraic equation for the single-bond EMA of a composite material with M-many components will be,

$$\sum_{i=1}^{M} P_i \frac{\hat{\sigma}_i - \hat{\sigma}_{\text{eff}}}{\hat{\sigma}_i + (z/2 - 1)\hat{\sigma}_{\text{eff}}} = 0 \tag{3.41}$$

The final result is important as it implies that the DC and AC case will have identical formulation/result. Such result is the norm for most classic effective medium approximations derived using Maxwell's equations. This is in contrast to the frequency-domain extension of the EMA derived from a stochastic transport theory [67]:

$$\int_{\Omega} f(w, P_1, P_2, \ldots, P_M) \frac{w - w_{\text{eff}}}{w(1 - \tilde{u}\hat{P}_{bb}) + (z/2 - (1 - \tilde{u}\hat{P}_{bb}))w_{\text{eff}}} \, \mathrm{d}w = 0 \tag{3.42}$$

$$\hat{\sigma}_{\text{eff}} = \frac{ne^2}{k_B T} a^2 w_{\text{eff}} \tag{3.43}$$

where w is the random jump rate or the random walk transition rate which is

necessarily real, $\tilde{u} = j\omega/w_n$ is normalized angular frequency, and $\hat{P}_{bb}$ is the diagonal bra-ket of the random walk propagator. The diagonal bra-ket of the propagator further determines how the random walk becomes frequency-dependent for different lattices. For a 1D chain and a 3D simple cubic lattice:

$$\hat{P}_{bb} = \begin{cases} \dfrac{1}{\sqrt{\tilde{u}(\tilde{u} + 4w_{\text{eff}})}} & \text{for 1D chain} \\ \dfrac{1}{2(\tilde{u} + w_{\text{eff}} + \sqrt{\tilde{u}(\tilde{u} + 12w_{\text{eff}})})} & \text{for 3D } sc \text{ lattice} \end{cases} \tag{3.44}$$

This particular EMA is indeed powerful for one specific objective: to model the microscopic mechanism of hopping conduction in *single-phase* disordered media, where the hopping transition rates in the given atomic lattice may not be uniform.

In the case of composite materials, the microscopic phenomenon is simply modeled through each individual component's complex conductivity $\hat{\sigma}_0$. A "disorder" would then be defined in terms of how those individual conductivities are randomly distributed throughout the inhomogeneous medium. Therefore, it is inappropriate to base the frequency-domain EMA scheme based upon the transition rates of a given atomic lattice[5]. Instead, the random AC network, naturally derived from continuum electrodynamics equations for an inhomogeneous media, is the more appropriate lattice picture of the composite material problem.

Another important point must be made regarding the weakness of the *single bond* EMA. It is a well-known property that almost all single-bond EMAs lose their accuracy near percolation thresholds (such as conductor/insulator transition). The explanation for this behavior can be found due to "correlation" effects that become significant at very large length scales near those critical regions, as the network's electrical properties are transforming in an incredibly disruptive manner[6]. One famous method to correct the behavior near those critical regions is to replace the single

[5]This is not to say that it cannot be worked out. One may assign transition rates for each component of the composite material and derive the effective conductivity. Afterwards, the equation can be added in parallel with a capacitor to model the material's permittivity, such was done in Ref [7] for dispersed ionic conductors. However, such model cannot take into account the inhomogeneity of the material's relative permittivity, making this EMA scheme inappropriate still.

[6]An analogy can also be made with solid-to-gas phase transition, such as sublimation, in materials. In such phase transition, the rigid atomic lattices are being disrupted at all length scales as the material is transforming into free-moving gas atoms.

impurity bond with a *cluster* of impurities. Cluster extension methods for the EMA will almost always require the use lattice Green's functions, hence why their presence in the EMA is significant. In terms of the heuristics approach, cluster extension will require the evaluation of Σ_{AB} beyond the nearest neighbor is needed, which is where the lattice Green's function would be invaluable. In terms of the bond Green's function approach, lattice Green's function will be used as part of a diagrammatic expansion imposed by the cluster extension in different orders of correction. More on the bond Green's function approach can be found in several references [75–79].

3.3 Models for M-Component System

One may notice that the single-bond EMA will immediately produce a characteristic M-th order polynomial for an M-many component system. This fact can be readily observed by multiplying the denominator of Eq. 3.41 to produce another equivalent equation:

$$\sum_{i=1}^{M} \left\{ P_i(\hat{\sigma}_i - \hat{\sigma}_{\text{eff}}) \left[\prod_{j \neq i}^{M-1} (\hat{\sigma}_j + \left(\frac{z}{2} - 1 \right) \hat{\sigma}_{\text{eff}}) \right] \right\} = 0 \tag{3.45}$$

which is essentially a polynomial of M-th order if each factor is expanded. The fact that the algebraic structure of the effective medium approximation (EMA) is a polynomial has significant physical context towards understanding the percolating behavior of composite materials with arbitrary number of components.

In general, the coefficients of the polynomial resulting in expanding Eq. 3.45 are regarded as a product of algebraic manipulation. However, if each coefficient can be thought of as a **coupling coefficient**, its role in determining the mixing rule for a multi-component composite material will be clearly appreciated. The coupling coefficients can be denoted as $\mathcal{K}_{\hat{\sigma}}^{(k)}$, derived term-by-term after expanding the polynomial such as Eq. 3.41:

$$\sum_{k=0}^{M} \mathcal{K}_{\hat{\sigma}}^{(k)} (\hat{\sigma}_{\text{eff}})^{M-k} = 0 \tag{3.46}$$

Suppose that a compact polynomial was obtained for a composite material with some number of components M. One may then ask several basic questions which is related to the properties of the resulting polynomial:

1. What is the physical significance of each coupling coefficient?
2. What is the role of the discriminant Δ_M of the polynomial?
3. What does the polynomial tells us about the solution to the composite material problem?

To answer these questions efficiently, it is instructive to start with the simplest composite system, which is the two-component system or $M = 2$. This will allow some of the key concepts to be understood in a simpler manner.

3.3.1 2-Component System, $M = 2$

The two-component system is the simplest model for a composite material and can be interpreted as a model for two-phase material which has no or little existing space charge layer contribution. And as the simplest model of a composite material, the percolating behavior of the EMA will be more thoroughly discussed here. Firstly, it is easy to see the resulting quadratic equation can be found by applying Eq. 3.41:

$$P_1 \frac{\hat{\sigma}_1 - \hat{\sigma}_{\text{eff}}}{\hat{\sigma}_1 + (z/2-1)\hat{\sigma}_{\text{eff}}} + P_2 \frac{\hat{\sigma}_2 - \hat{\sigma}_{\text{eff}}}{\hat{\sigma}_2 + (z/2-1)\hat{\sigma}_{\text{eff}}} = 0 \tag{3.47}$$

Multiplying the denominator and expanding each term, the two-component system will result in the following quadratic equation with the following coupling coefficients:

$$\mathcal{K}_{\hat{\sigma}}^{(0)}(\hat{\sigma}_{\text{eff}})^2 + \mathcal{K}_{\hat{\sigma}}^{(1)}(\hat{\sigma}_{\text{eff}}) + \mathcal{K}_{\hat{\sigma}}^{(2)}(\hat{\sigma}_{\text{eff}}) = 0 \tag{3.48}$$

$$\mathcal{K}_{\hat{\sigma}}^{(0)} = -\left(\frac{z}{2} - 1\right) \tag{3.49}$$

$$\mathcal{K}_{\hat{\sigma}}^{(1)} = \hat{\sigma}_1 \left(\frac{z}{2}P_1 - 1\right) + \hat{\sigma}_2 \left(\frac{z}{2}P_2 - 1\right) \tag{3.50}$$

$$\mathcal{K}_{\hat{\sigma}}^{(2)} = \hat{\sigma}_1 \hat{\sigma}_2 \tag{3.51}$$

The solution is simply obtained by the quadratic formula in which the solution will always be positive, i.e. the physical result:

$$\hat{\sigma}_{\text{eff}} = -\frac{1}{2\mathcal{K}_{\hat{\sigma}}^{(0)}}\left[\mathcal{K}_{\hat{\sigma}}^{(1)} + \sqrt{\left(\mathcal{K}_{\hat{\sigma}}^{(1)}\right)^2 - 4\mathcal{K}_{\hat{\sigma}}^{(0)}\mathcal{K}_{\hat{\sigma}}^{(2)}}\right]. \tag{3.52}$$

With closed-form expressions of the 1st and 2nd coupling coefficients derived, it is now easy to see why the 'coupling' terminology is used using the diagram representation of the coupling coefficients found in Fig. 3.9. In the 1st order coupling coefficient, each individual (complex-valued) conductivity ($\hat{\sigma}_1$ and $\hat{\sigma}_2$)is weighted proportionally to its respective volume fraction. Each of them would then be added to produce the final coupling coefficient. However, the 2nd order coupling coefficient will feature a coupling between the two component's conductivity, mathematically represented simply by the product between the two.

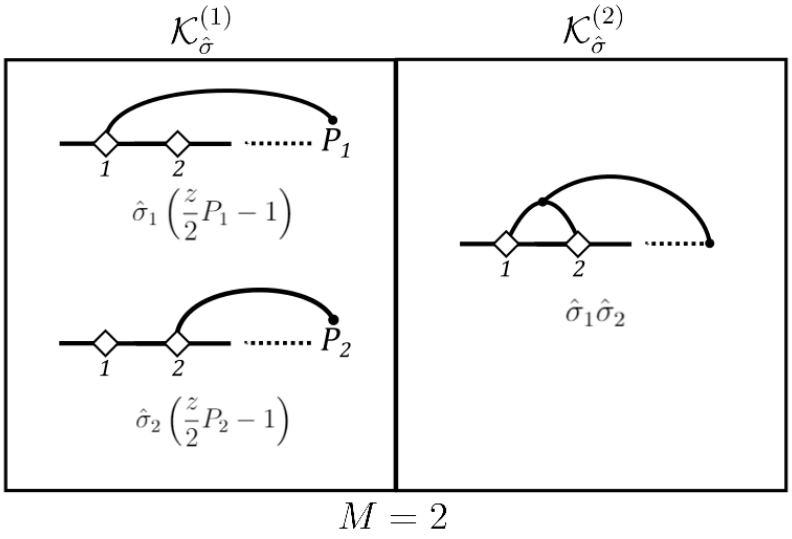

Figure 3.9: Diagram representation of coupling behavior in a two-component system ($M = 2$) with accompanying mathematical expressions. One diagram represents one term in the coupling coefficient. A diamond ($\diamond$) represents one complex conductivity, a dashed line indicates proportionality with volume fraction for each term. Black curves will connect conductivities as a form of coupling and finalize the loop by connecting it to its respective volume fraction proportionality. Thus, a closed loop will indicate a non-zero term. For instance, one term in the 1st coupling coefficient has $\diamond$ for one component completing a loop with its own volume fraction.

This concept is crucial in non-linear regression analysis of multi-component composite materials as it implies that any EMA model cannot be used to *completely parametrize* each individual conductivity using one set of data unless some foreknowledge or assumption was acquired to reduce the coupling or order of the system. Fortunately, the diagrams in Fig. 3.9 can be instructive in how a *decoupling procedure* can be made to make the models more tractable. The decoupling procedure is illustrated in Fig. 3.10. By treating one of the conductivities to be zero, which is a typical for modeling an insulating component in the DC regime, an M-component system is reduced to an $M-1$ component system as the highest order coupling coefficient vanishes to zero. Thus, the two-component system is reduced to a quasi one-component system. For a system with arbitrary number of components, the coefficients resulted from such procedure will be denoted as $\mathcal{Q}_{\hat{\sigma}}^{(l,k)}$, where the superscript set (l,k) denotes to what order it the component system is decreased to, e.g., $l=2$ for reducing an arbitrary system to a quasi two-component system, as and its order.

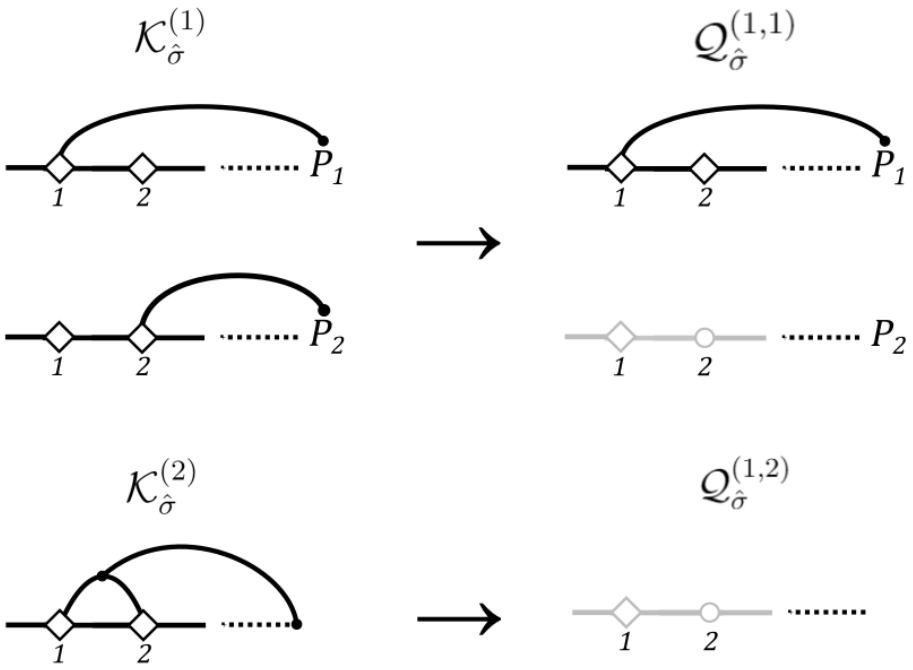

Figure 3.10: A decoupling procedure by introducing an ideal insulator in (2), i.e. $\hat{\sigma}_2 = 0$. When an ideal insulator is set as one of its component, the coupling loop vanishes which completely erases it from contributing to the effective conductivity. In the two-component ($M=2$) case, this turns the problem into a quasi-one-component problem.

The resulting quasi-one component system can be found with the following straight line equation:

$$\begin{aligned} \hat{\sigma}_{\text{eff}} &= -\frac{\mathcal{Q}_{\hat{\sigma}}^{(1,1)}}{\mathcal{Q}_{\hat{\sigma}}^{(1,0)}} \\ \mathcal{Q}_{\hat{\sigma}}^{(1,0)} &= -\left(\frac{z}{2}-1\right) \\ \mathcal{Q}_{\hat{\sigma}}^{(1,1)} &= \hat{\sigma}_1\left(\frac{z}{2}P_1-1\right) \end{aligned} \tag{3.53}$$

It is easy to verify that the straight-line equation crosses zero conductivity at a specific concentration denoted as the critical percolation threshold p_c. For a 3D simple cubic lattice where $z = 6$, the percolation threshold $p_c = 1/3$. The decoupling procedure made above is in fact the standard way for which true percolation to be studied for any lattice system [7]. However, it is difficult to appreciate the result by performing the decoupling procedure alone. More intuition can be made by analyzing the discriminant of the quadratic equation.

It was briefly described that the discriminant of the solution to the two-component system is related to the percolation threshold of the system [84]. Thus, in the context of coupling coefficients, the percolation threshold for this specific conductor/insulator mixture can also be found using its discriminant:

$$\Delta_{M=2} = \left(\mathcal{K}_{\hat{\sigma}}^{(1)}\right)^2 - 4\mathcal{K}_{\hat{\sigma}}^{(0)}\mathcal{K}_{\hat{\sigma}}^{(2)} \tag{3.54}$$

The discriminant can be plotted, starting from $\sigma_2 = \sigma_1/10$ to $\sigma_2 = 0$ to represent gradual transformation of one component to an ideal insulator. The figure for such case when $z = 6$ (3D simple cubic lattice) can be found in Fig. 3.11. It is interesting to note that the curve starts from the top at higher value of σ_2 before the minimum touches the x-axis. This particular point in the minimum simultaneously act as when $\Delta_{M=2} = 0$. With elementary calculations, it can be easily shown that the minimum point is equivalent to the percolation threshold $p_c = 1/3$.

[7] Alternatively, one may set one of the component's conductivity to be infinite, i.e. $\hat{\sigma}_2 = \infty$, representing a conductor-superconductor mixtures. Studying conductor-ideal insulator and conductor-superconductor mixtures is the standard mode of analysis for many percolation studies.

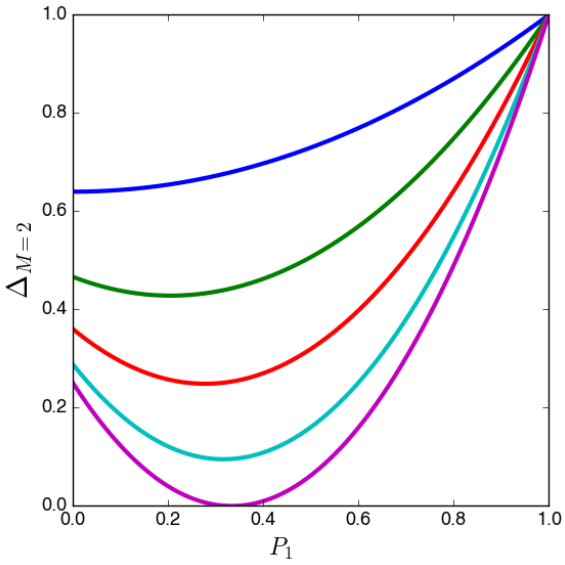

Figure 3.11: Plot of the discriminant function ($z = 6$) for the two-component system $\Delta_{M=2}$ normalized to its value at $P_1 = 1$. The larger the ratio between σ_1 and σ_2, the lower the minimum of the discriminant.

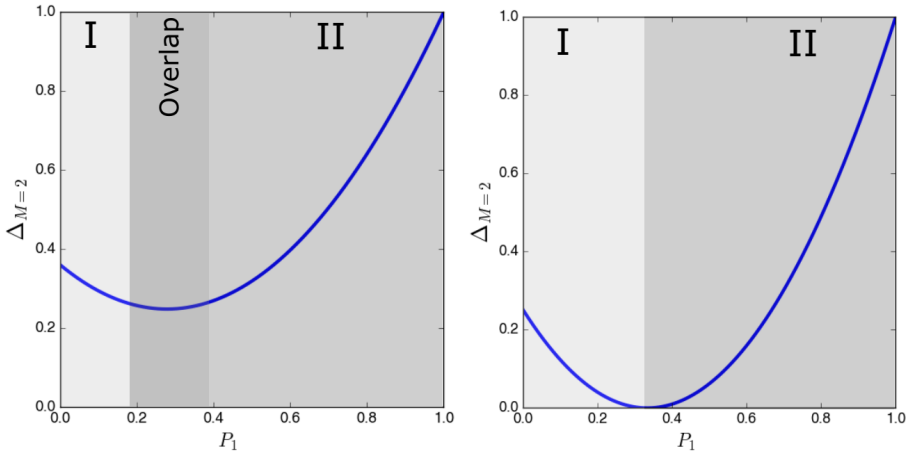

Figure 3.12: Comparison between the discriminant function when $\sigma_2 = \sigma_1/8$ and $\sigma_2 = 0$. When the minimum touches the x-axis, true percolation is established. When this is not the case, overlap of regions is observed.

Thus, the discriminant of the two-component system helps determine how significant is the percolation transition, as illustrated in Fig. 3.12. When the minimum of the discriminant touches the x-axis, the material will experience true percolation and two distinct regions of concentrations may be found indicating a composite material

that can take two different electrical properties (conducting and insulating, in this case). When this is not the case, the system does not have true percolation and what was supposed to be two distinct regions becomes two *overlapping* regions. The minimum point can then be used to determine the effective transition point.

Before moving on towards higher number component system, several final comments shall be made. Firstly, a famous effective medium approximation named the Bruggemann symmetrical formula can be obtained by setting $z = 6$ and applying the analytical solution to the two-component problem:

$$\hat{\sigma}_{\text{eff}} = \frac{1}{4}\left[\mathcal{K} + \sqrt{\mathcal{K}^2 - 8\hat{\sigma}_1\hat{\sigma}_2}\right] \tag{3.55}$$
$$\mathcal{K} = \hat{\sigma}_1(3P_1 - 1) + \hat{\sigma}_2(3P_2 - 1)$$

The Bruggemann symmetrical formula was obtained directly from the continuum electrodynamics equations (without any discretization process) as an improvement to the Maxwell-Garnett equation [85]. This direct correspondence to a continuum EMA model provides an important precedence for the choice of a 3D simple cubic lattice as the correct lattice model for the composite material. Secondly, one must keep in mind that the percolation threshold obtained for 3D simple cubic lattice does not agree with the accurate and widely-accepted 'exact' result through large-scale Monte Carlo simulations, which is $p_c = 0.2456$. As discussed in Section 3.2, this discrepancy can be sourced from the lack of correlation effects in the single-bond EMA.

With the role of the coupling coefficients and discriminant established, the discussion is now ready to move towards higher number component system. At the present, no analytical solution has been provided yet a general k-th order mixing coupling coefficients for an arbitrary number of components. However, it is known by Abel-Ruffini theorem that an analytical *algebraic* solution in the form of radicals, e.g. square roots, cubic roots, can only be obtained for polynomials of order 4 and below. This restriction should be well enough for many applications. Because of that, the results for 3-, and 4- component system will be presented in the next subsections.

3.3.2 3-Component System, $M = 3$

The three-component system can represent a model for a two-component composite with a single space charge layer, such as that of dispersed ionic conductors, or just a general three-phase material with negligible space charge layer. Applying Eq. 3.41 again, it may be independently confirmed that the k-th order coupling coefficients for the resulting cubic equation will be the following:

$$\mathcal{K}_{\hat{\sigma}}^{(0)}(\hat{\sigma}_{\text{eff}})^3 + \mathcal{K}_{\hat{\sigma}}^{(1)}(\hat{\sigma}_{\text{eff}})^2 + \mathcal{K}_{\hat{\sigma}}^{(2)}(\hat{\sigma}_{\text{eff}}) + \mathcal{K}_{\hat{\sigma}}^{(3)} = 0 \tag{3.56}$$

$$\mathcal{K}_{\hat{\sigma}}^{(0)} = -\left(\frac{z}{2} - 1\right)^2 \tag{3.57}$$

$$\begin{aligned}
\mathcal{K}_{\hat{\sigma}}^{(1)} =& \left(\frac{z}{2} - 1\right)\left[\hat{\sigma}_1\left(\frac{z}{2}P_1 - 1\right) + \hat{\sigma}_2\left(\frac{z}{2}P_2 - 1\right) + \hat{\sigma}_3\left(\frac{z}{2}P_3 - 1\right)\right] \\
\mathcal{K}_{\hat{\sigma}}^{(2)} =& \hat{\sigma}_1\hat{\sigma}_2\left(\frac{z}{2}(1 - P_3) - 1\right) + \hat{\sigma}_2\hat{\sigma}_3\left(\frac{z}{2}(1 - P_1) - 1\right) \\
&+ \hat{\sigma}_1\hat{\sigma}_3\left(\frac{z}{2}(1 - P_2) - 1\right)
\end{aligned} \tag{3.58}$$

$$\mathcal{K}_{\hat{\sigma}}^{(3)} = \hat{\sigma}_1\hat{\sigma}_2\hat{\sigma}_3 \tag{3.59}$$

The diagram representation for the coupling coefficients in the three-component system may be found in Fig. 3.13. The similar trend is also observed with the two-component system except that now the combinatorial way in which coupling occurs can be more clearly appreciated, especially when looking at the 2^{nd} coupling coefficient. Each term in the 2^{nd} coupling coefficient is linearly proportionally to the volume fraction of the uncoupled component within that term.

For the cubic equation, an analytical solution has been derived for real coefficients, which is known as the Cardano's solution [86]. Thus, it may be used for both DC exactly and low-frequency AC approximately. Expressed in terms of the k-th order coupling coefficients, the analytical solution is the following:

$$\hat{\sigma}_{\text{eff}} = -\frac{\mathcal{K}_{\hat{\sigma}}^{(1)}}{3\mathcal{K}_{\hat{\sigma}}^{(0)}} + \sqrt[3]{\mathcal{R}_{\hat{\sigma}} + \sqrt{(\mathcal{R}_{\hat{\sigma}})^2 - (\mathcal{S}_{\hat{\sigma}})^3}} + \sqrt[3]{\mathcal{R}_{\hat{\sigma}} - \sqrt{(\mathcal{R}_{\hat{\sigma}})^2 - (\mathcal{S}_{\hat{\sigma}})^3}} \tag{3.60}$$

$$\mathcal{R}_{\hat{\sigma}} = \frac{\mathcal{K}_{\hat{\sigma}}^{(1)}\mathcal{K}_{\hat{\sigma}}^{(2)}}{6\left(\mathcal{K}_{\hat{\sigma}}^{(0)}\right)^2} - \frac{\mathcal{K}_{\hat{\sigma}}^{(3)}}{2\mathcal{K}_{\hat{\sigma}}^{(0)}} - \left(\frac{\mathcal{K}_{\hat{\sigma}}^{(1)}}{3\mathcal{K}_{\hat{\sigma}}^{(0)}}\right)^3 \tag{3.61}$$

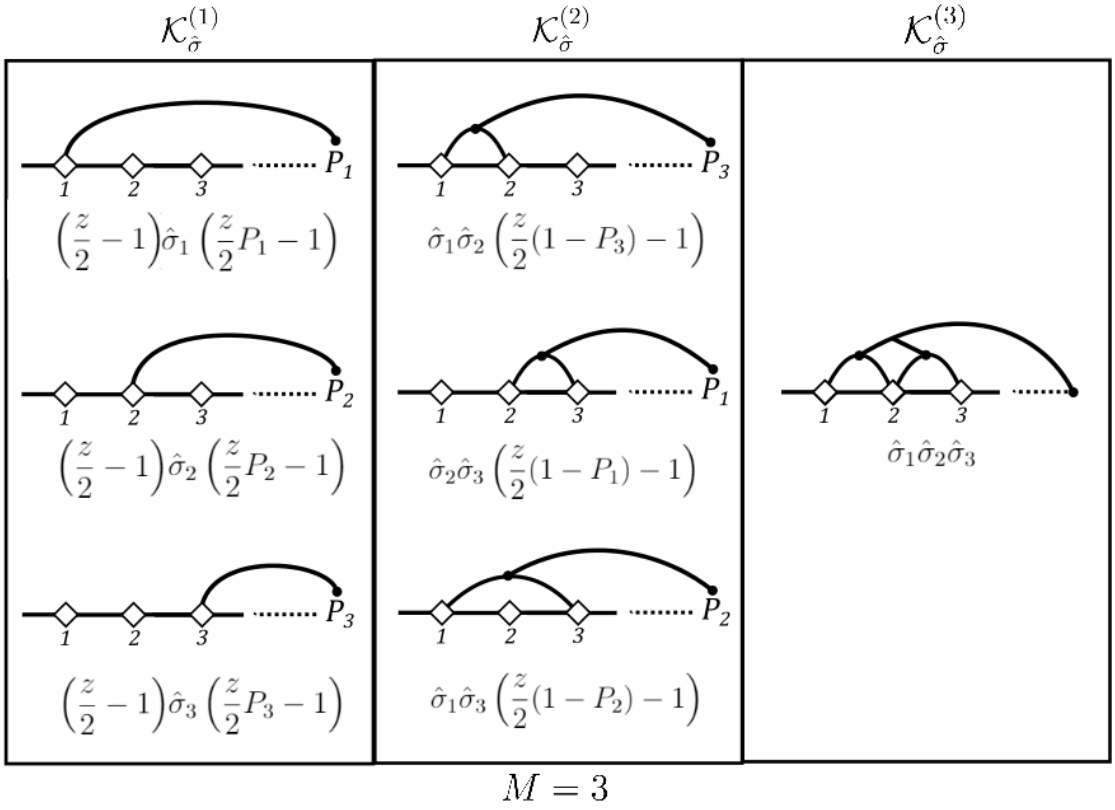

Figure 3.13: Diagram representation of coupling behavior in a three-component system ($M = 3$) with accompanying mathematical expressions. The combinatorial way in which coupling occurs can now be clearly elucidated. For instance, in the 2nd coupling coefficient, each diagram is weighted by the volume fraction of the uncoupled component of that specific diagram. This suggests that the general solution may involve some sort of complex combinatorial representation that depends on the order of the coupling coefficient k and the number of components M

$$\mathcal{S}_{\hat{\sigma}} = \frac{\mathcal{K}_{\hat{\sigma}}^{(2)}}{3\mathcal{K}_{\hat{\sigma}}^{(0)}} - \left(\frac{\mathcal{K}_{\hat{\sigma}}^{(1)}}{3\mathcal{K}_{\hat{\sigma}}^{(0)}}\right)^2 \tag{3.62}$$

For a general solution at finite frequencies, which will be helpful in studying the impedance and modulus spectra, a numerical method can be used such as the `roots` function in MATLAB and Python to solve for all roots of the polynomial in a fast manner, and extract only the physical solution. The physical solution will correspond to the root in which its real part will be positive or equal to zero, i.e. $Re(\hat{\sigma}_{\text{eff}}) \geq 0$. For details in implementing this procedure, see the Appendix.

The percolation thresholds and general percolating behavior of the system can be further determined by looking at the determinant of the cubic polynomial:

$$\Delta_{M=3} = \left(\mathcal{K}_{\hat{\sigma}}^{(1)}\mathcal{K}_{\hat{\sigma}}^{(2)}\right)^2 - 4\mathcal{K}_{\hat{\sigma}}^{(0)}\left(\mathcal{K}_{\hat{\sigma}}^{(2)}\right)^3 - 4\mathcal{K}_{\hat{\sigma}}^{(3)}\left(\mathcal{K}_{\hat{\sigma}}^{(1)}\right)^3 - 27\left(\mathcal{K}_{\hat{\sigma}}^{(0)}\mathcal{K}_{\hat{\sigma}}^{(3)}\right)^2 + 18\mathcal{K}_{\hat{\sigma}}^{(0)}\mathcal{K}_{\hat{\sigma}}^{(1)}\mathcal{K}_{\hat{\sigma}}^{(2)}\mathcal{K}_{\hat{\sigma}}^{(3)} \tag{3.63}$$

Following the example of the two-component system, a decoupling procedure at the DC case can be performed by setting one of its components to zero. This will transform the equation into the following quadratic equation:

$$\mathcal{Q}_{\hat{\sigma}}^{(2,0)}(\hat{\sigma}_{\text{eff}})^2 + \mathcal{Q}_{\hat{\sigma}}^{(2,1)}(\hat{\sigma}_{\text{eff}}) + \mathcal{Q}_{\hat{\sigma}}^{(2,2)} = 0 \tag{3.64}$$

$$\mathcal{Q}_{\hat{\sigma}}^{(1,0)} = -\left(\frac{z}{2} - 1\right)^2 \tag{3.65}$$

$$\mathcal{Q}_{\hat{\sigma}}^{(1,1)} = \left(\frac{z}{2} - 1\right)\left[\hat{\sigma}_1\left(\frac{z}{2}P_1 - 1\right) + \hat{\sigma}_2\left(\frac{z}{2}P_2 - 1\right)\right] \tag{3.66}$$

$$\mathcal{Q}_{\hat{\sigma}}^{(1,2)} = \hat{\sigma}_1\hat{\sigma}_2\left(\frac{z}{2}(1 - P_3) - 1\right) \tag{3.67}$$

where both the solution and the discriminant is already defined from previous section.

Unlike the two-component system, the volume fraction has an extra degree of freedom. Thus, the percolating behavior of the system will depend on what type of mixtures are being made and how does each component's volume fraction change with only the volume fraction of one component. An analysis of the percolating behavior of a three-component system through the discriminant function will be done for dispersed ionic conductors in Section 3.4.

3.3.3 4-Component System, $M = 4$

While conductor-insulator composites are heavily studied, a general two-phase material has shown to have two distinct space charge layers, one for each phase if each contains conducting ions [35]. This implies that a four-component system might be suitable for that specific purpose. Alternatively, a solution to the four-component composite will also be important for a general four-phase material which neglects

their space charge layer contributions. The four component system will result in a quartic equation with the following coupling coefficients:

$$\mathcal{K}_{\hat{\sigma}}^{(0)}(\hat{\sigma}_{\text{eff}})^4 + \mathcal{K}_{\hat{\sigma}}^{(1)}(\hat{\sigma}_{\text{eff}})^3 + \mathcal{K}_{\hat{\sigma}}^{(2)}(\hat{\sigma}_{\text{eff}})^2 + \mathcal{K}_{\hat{\sigma}}^{(3)}(\hat{\sigma}_{\text{eff}}) + \mathcal{K}_{\hat{\sigma}}^{(4)} = 0 \tag{3.68}$$

$$\begin{aligned}
\mathcal{K}_{\hat{\sigma}}^{(0)} &= -\left(\frac{z}{2}-1\right)^3 \\
\mathcal{K}_{\hat{\sigma}}^{(1)} &= \left(\frac{z}{2}-1\right)^2\left[\hat{\sigma}_1\left(\frac{z}{2}P_1-1\right)+\hat{\sigma}_2\left(\frac{z}{2}P_2-1\right)+\hat{\sigma}_3\left(\frac{z}{2}P_3-1\right)+\hat{\sigma}_d\left(\frac{z}{2}P_4-1\right)\right] \\
\mathcal{K}_{\hat{\sigma}}^{(2)} &= \left(\frac{z}{2}-1\right)\left(\hat{\sigma}_1\hat{\sigma}_2\left\{\frac{z}{2}[1-(P_3+P_4)]-1\right\}+\hat{\sigma}_2\hat{\sigma}_3\left\{\frac{z}{2}[1-(P_1+P_4)]-1\right\}\right. \\
&\quad +\hat{\sigma}_3\hat{\sigma}_d\left\{\frac{z}{2}[1-(P_1+P_2)]-1\right\}+\hat{\sigma}_1\hat{\sigma}_d\left\{\frac{z}{2}[1-(P_2+P_3)]-1\right\} \\
&\quad \left.+\hat{\sigma}_1\hat{\sigma}_3\left\{\frac{z}{2}[1-(P_2+P_4)]-1\right\}+\hat{\sigma}_1\hat{\sigma}_d\left\{\frac{z}{2}[1-(P_2+P_3)]-1\right\}\right) \\
\mathcal{K}_{\hat{\sigma}}^{(3)} &= \hat{\sigma}_1\hat{\sigma}_2\hat{\sigma}_3\left(\frac{z}{2}(1-P_4)-1\right)+\hat{\sigma}_2\hat{\sigma}_3\hat{\sigma}_d\left(\frac{z}{2}(1-P_1)-1\right) \\
&\quad +\hat{\sigma}_1\hat{\sigma}_3\hat{\sigma}_d\left(\frac{z}{2}(1-P_2)-1\right)+\hat{\sigma}_1\hat{\sigma}_2\hat{\sigma}_d\left(\frac{z}{2}(1-P_3)-1\right) \\
\mathcal{K}_{\hat{\sigma}}^{(4)} &= \hat{\sigma}_1\hat{\sigma}_2\hat{\sigma}_3\hat{\sigma}_d
\end{aligned}$$

Due to the length of these coupling coefficients, the diagrams shall not be presented but using the intuition obtained from the three-component system, the combinatorial way in which coupling occurs can be carefully inspected term-by-term. The Ferrari's solution for the quartic equation can be used to obtain the analytical equation applicable to DC regime and low-frequency region [86]. While this analytical solution can be very lengthy to implement, the previous-mentioned `roots` function from Python or MATLAB can also be implemented again even for the DC case. However, the Ferrari's solution will still be presented here for the sake of completion:

$$\hat{\sigma}_{\text{eff}} = -\frac{\mathcal{K}_{\hat{\sigma}}^{(1)}}{4\mathcal{K}_{\hat{\sigma}}^{(0)}} - \mathfrak{T}_{\hat{\sigma}} + \frac{1}{2}\sqrt{-4\left(\mathfrak{T}_{\hat{\sigma}}\right)^2 - 2\mathfrak{p} + \frac{\mathfrak{q}}{\mathfrak{T}_{\hat{\sigma}}}} \tag{3.69}$$

$$\mathfrak{p} = \frac{8\mathcal{K}_{\hat{\sigma}}^{(0)}\mathcal{K}_{\hat{\sigma}}^{(2)} - 3\left(\mathcal{K}_{\hat{\sigma}}^{(1)}\right)^2}{8\left(\mathcal{K}_{\hat{\sigma}}^{(0)}\right)^2} \tag{3.70}$$

$$\mathfrak{q} = \frac{\left(\mathcal{K}_{\hat{\sigma}}^{(1)}\right)^3 - 4\mathcal{K}_{\hat{\sigma}}^{(0)}\mathcal{K}_{\hat{\sigma}}^{(1)}\mathcal{K}_{\hat{\sigma}}^{(2)} + 8\left(\mathcal{K}_{\hat{\sigma}}^{(0)}\right)^2\mathcal{K}_{\hat{\sigma}}^{(3)}}{8\left(\mathcal{K}_{\hat{\sigma}}^{(0)}\right)^3} \tag{3.71}$$

$$\mathfrak{T}_{\hat{\sigma}} = \frac{1}{2}\sqrt{-\frac{2}{3}\,p + \frac{1}{3\mathcal{K}_{\hat{\sigma}}^{(0)}}\left(\mathfrak{U}_{\hat{\sigma}} + \frac{\Lambda_0}{\mathfrak{U}_{\hat{\sigma}}}\right)} \tag{3.72}$$

$$\mathfrak{U}_{\hat{\sigma}} = \sqrt[3]{\frac{\Lambda_1 + \sqrt{\Lambda_1^2 - 4\Lambda_0^3}}{2}} \tag{3.73}$$

$$\Lambda_0 = \left(\mathcal{K}_{\hat{\sigma}}^{(2)}\right)^2 - 3\mathcal{K}_{\hat{\sigma}}^{(1)}\mathcal{K}_{\hat{\sigma}}^{(3)} + 12\mathcal{K}_{\hat{\sigma}}^{(0)}\mathcal{K}_{\hat{\sigma}}^{(4)} \tag{3.74}$$

$$\begin{aligned}\Lambda_1 =& 2\left(\mathcal{K}_{\hat{\sigma}}^{(2)}\right)^3 - 9\mathcal{K}_{\hat{\sigma}}^{(1)}\mathcal{K}_{\hat{\sigma}}^{(2)}\mathcal{K}_{\hat{\sigma}}^{(3)} + 27\left(\mathcal{K}_{\hat{\sigma}}^{(1)}\right)^2\mathcal{K}_{\hat{\sigma}}^{(4)} + 27\mathcal{K}_{\hat{\sigma}}^{(0)}\left(\mathcal{K}_{\hat{\sigma}}^{(3)}\right)^2 \\ & - 72\mathcal{K}_{\hat{\sigma}}^{(0)}\mathcal{K}_{\hat{\sigma}}^{(2)}\mathcal{K}_{\hat{\sigma}}^{(4)}\end{aligned} \tag{3.75}$$

3.4 Application: Dispersed Ionic Conductors

The most important feature to be accounted for in dispersed ionic conductors is the volume fractions equations. Since a two-phase material is being modelled as a three-component system, the extra degree of freedom must be taken account for based on how space charge layer volume fraction changes with the insulator concentration. This depends on how one view the geometrical problem. Early percolation-based models relied upon an analysis of small primitive square and cubic lattices [6, 42]. Applying these volume fraction equations can allow obtaining the right qualitative shape of the conductivity vs. insulator concentration curve, even with a non-percolating model as exemplified in Ref. [2].

Volume fraction equations can be modeled more precisely by considering overlapping spherical particles which follow a Poisson distribution [3]. Firstly, suppose that the dispersed material is the insulator, in the form of spherical particles (in 3D) or circular disks (in 2D). The volume fraction of each spherical insulating particle can be denoted as $P_c = p$ and may be found as:

$$p = 1 - e^{-cR^N\rho_d} \tag{3.76}$$

where c is a constant related to the dimension of the space, ρ_d is the density of the matrix (which is the conductor), R is the insulting particle's radius, and N is the dimension of the space ($N = 3$ for 3D). Using Eq. 3.76, ρ_d can also be expressed in

terms of the insulator volume fraction:

$$\rho_d = -\ln(1-p)^{\frac{1}{cR^N}} \tag{3.77}$$

In dispersed ionic conductors, each insulating particle will have a concentric shell of space charge layer surrounding it. Suppose that a dimensionless variable $\eta = 1 + \frac{\lambda}{R}$ is introduced, where λ is the thickness of the shell or space charge layer. This allows expressing the volume fraction of the composite core-shell particle similarly to P_c:

$$P_{c-s} = 1 - e^{-c(\eta R)^N \rho_d} \tag{3.78}$$

Therefore, the volume fraction of the space charge layer P_b can be found in terms p through Eq. 3.77 and 3.78

$$P_b = P_{c-s} - p \tag{3.79}$$

$$= 1 - p - (1-p)^{\eta^N} \tag{3.80}$$

The volume fraction of the conductor can be found easily afterwards. Recalling that subscript 'a' refers to the conductor, subscript 'b' refers to the space charge layer, and subscript 'c' refers to the insulator, then the volume fraction equations for dispersed ionic conductors can be found as:

$$P_a = (1-p)^{\eta^N} \tag{3.81}$$

$$P_b = 1 - p - (1-p)^{\eta^N} \tag{3.82}$$

$$P_c = p \tag{3.83}$$

$$\eta = 1 + \frac{\lambda}{R} \tag{3.84}$$

With these equations in mind, it is possible to re-derive the EMA 'continuum percolation' model from Ref. [3] by performing a decoupling procedure. By setting the insulator one of the component's conductivity to be zero ($\hat{\sigma}_c = 0$ in this case), normalizing the conductor's conductivity, i.e. $\hat{\sigma}_1 = 1$ and $\hat{\sigma}_2 = \tau$, and letting the conductivity to be purely real, Eq. 3.52 can be used to obtain the solution that is

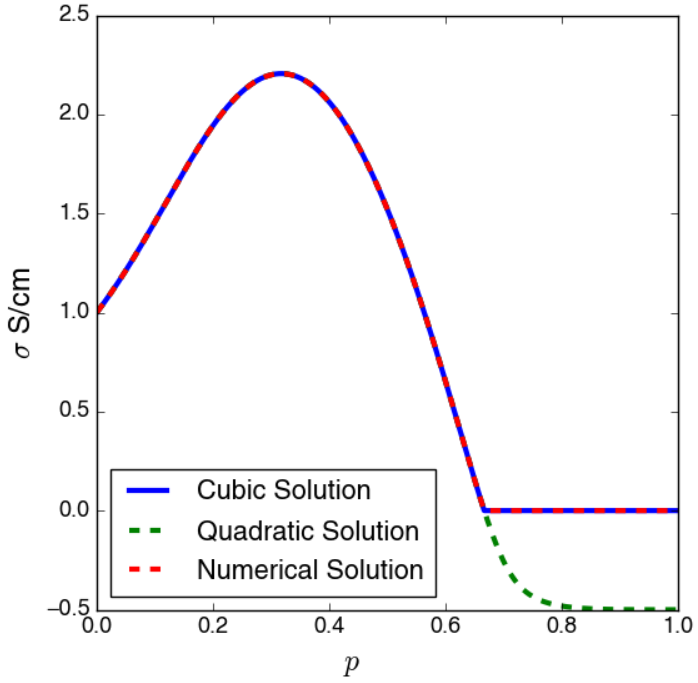

Figure 3.14: A comparison between this work's analytical solution, representing the original three-component system, the quasi two-component system's solution, identical to solution by Roman [3], and the numerical solution. The quasi-two component system will yield unphysical result beyond the conductor/insulator transition, limiting its applicability. Parameters: $\sigma_a = 1$, $\sigma_b = 10$, $\eta = 1.5$

completely identical to the one given in Ref. [3]. Care must be taken in using this solution as it is restricted to volume fractions below the conductor/insulator transition p_c, as illustrated in Fig. 3.14. In Fig. 3.14, the conductivity of the insulator goes to negative as a result of the decoupling procedure while both the numerical and analytical solution was still applicable above the percolation threshold. Therefore, the solution to the quasi-two phase component system *shall not be used* and the solution for the original cubic equation, as presented in Section 3.3, will be used instead.

Now that the volume fraction equations are established, the discriminant $\Delta_{M=3}$ can be plotted to observe the percolating behavior of the system. Fig. 3.15 shows the plot of the discriminant normalized to its value at 100% insulator and DC conductivity, using some set parameters. The shape of the curve resembles a double-well

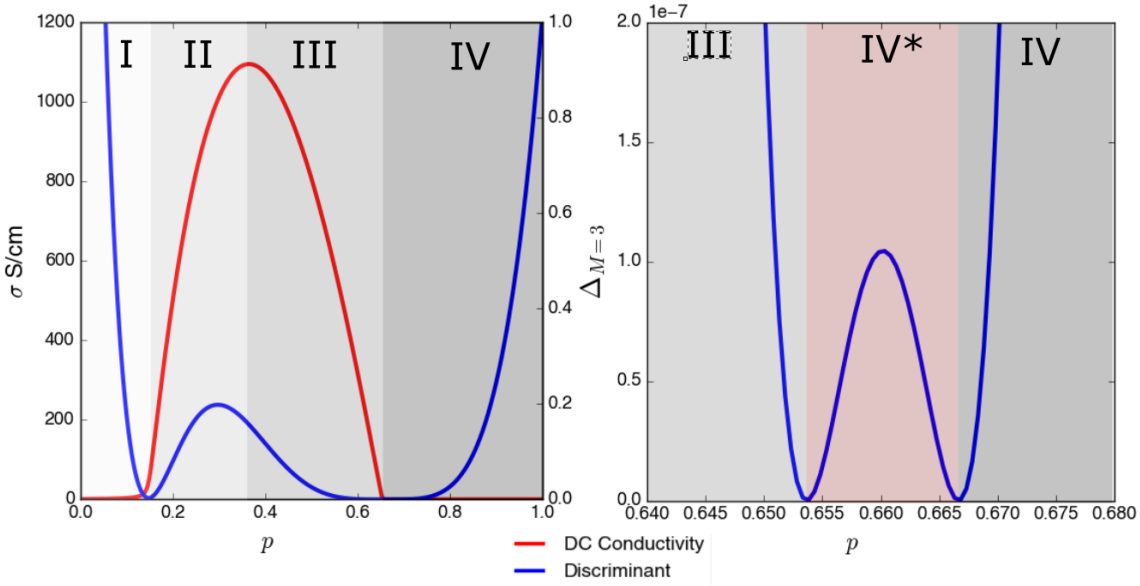

Figure 3.15: Plot of the discriminant $\Delta_{M=3}$ and DC conductivity, showcasing different regions of dispersed ionic conductor and existing percolation thresholds. In subsequent analysis, Region IV* is taken to be the same as Region IV. Parameters: $\sigma_a = 1$, $\sigma_b = 100$, $\eta = 1.6$.

potential, with both minima touch the x-axis. The minimum closer to the conductor side is known as the interface percolation p_c' while the minimum closer to the insulator side is known as the conductor/insulator transition p_c''. Closer inspection reveals that there's a third minimum very close to the conductor/insulator transition. The existence of a third percolation threshold p_c''' is a consistent feature in all percolation-based models of dispersed ionic conductors [3,6,42,43]. But for all practical purposes, this transition can be regarded to be equivalent to the conductor/insulator transition, i.e. $p_c'' \approx p_c'''$.

With the help of the discriminant function, four regions can be identified that is specific to the dispersed ionic conductor:

1. (Region I) *Normal region.* This is the region in a composite material where the electrical properties does not differ from the bulk conductor.

2. (Region II) *Space-charge layer region*: This is the region above the interface percolation, where enough space charge layers have formed to provide continuous highly conducting pathways.

3. (Region III) *Blocking region.* This is the region after the optimum concentration when the insulator concentration is high enough that it starts to decrease the conductivity of the composite.

4. (Region IV). *Insulating region.* This is the region after the conductor/insulator transition where the insulator component forms continuous blocking pathways that disrupts the composite and turning it into an insulator.

In addition, one may notice that the conductor-insulator transition can be calculated by performing a minimization procedure onto the discriminant function. While this can be done to solve for the interface percolation p_c' and the conductor/insulator transition p_c'', a less time-consuming method is to solve the following two relations: (1) $P_c = 1 - \frac{2}{z}$ for p_c'', and (2) $P_b = \frac{2}{z}$ for p_c' [3].

It is also useful to derive some bounds for theoretical maximum and minimum conductivity of the dispersed ionic conductor. These bounds come from two different limits: (1) negligible space charge layer ($\frac{\lambda}{R} \to 0$) and (2) very thick space charge layer ($\frac{\lambda}{R} \to \infty$). Alternatively, the first limit can also correspond to large particle sizes while the second limit corresponds to very small particle sizes. For $\frac{\lambda}{R} \to 0$ the volume fraction equations will be,

$$P_1 = 0; \quad P_2 = 1 - p; \quad P_3 = p \tag{3.85}$$

And for $\frac{\lambda}{R} \to \infty$,

$$P_1 = 1 - p; \quad P_2 = 0; \quad P_3 = p \tag{3.86}$$

These limiting cases affect the previous probability distribution by completely eliminating either the conductor's or space charge layer's contribution towards the conductivity of the composite. Performing the decoupling procedure, it may be readily confirmed that the bounds are straight line equations:

$$\sigma_{\text{eff}}^{\min} = \frac{\hat{\sigma}_1}{2}(2 - 3p) \quad \text{when } \frac{\lambda}{R} \to 0 \tag{3.87}$$

$$\sigma_{\text{eff}}^{\max} = \frac{\hat{\sigma}_2}{2}(2 - 3p) \quad \text{when } \frac{\lambda}{R} \to \infty \tag{3.88}$$

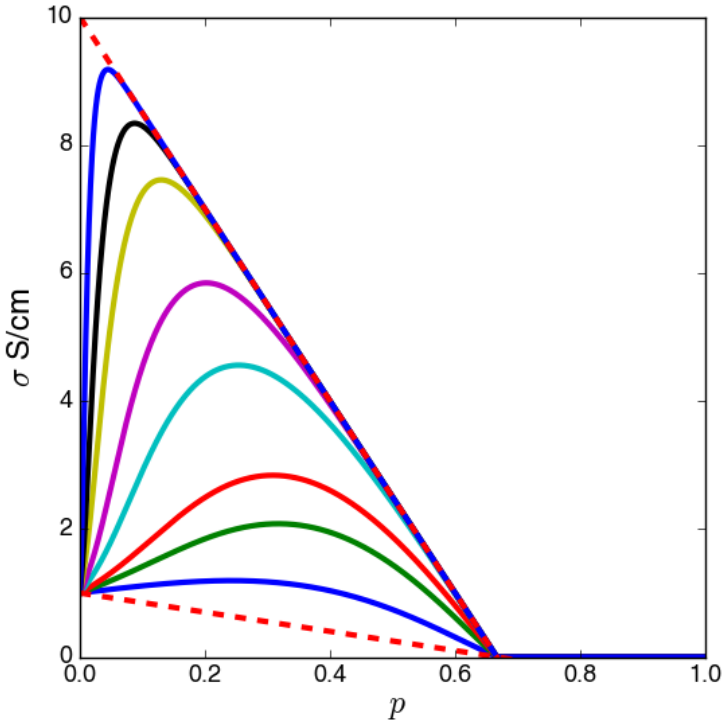

Figure 3.16: DC conductivity curves at different η values. With higher η, i.e. large space charge layer or smaller particle size, the enhancement will be significantly higher and the peak will move much closer to the conductor side. Parameters: $\sigma_a = 1$, $\sigma_b = 10$

Fig. 3.16 shows the usage of these bounds with plots of dispersed ionic conductors of different η. The trend can be clearly seen where the system will shift its optimum peak to the conductor side as the space charge layer thickness is increased or the particle size is reduced through different processing methods. In addition, the bounds can also provide an idea of whether a material, at its given concentration, can be further enhanced by looking at how far it is from its theoretical maximum.

3.4.1 Case Study: $LiI - Al_2O_3$

Now that all essential features of the model have been explained, the model's predictions on impedance spectra and conductivity can be explored. The case study material to be used is the $LiI - Al_2O_3$ system, based on Ref. [1]. Fitting was obtained through Python's LMFIT package, which provides non-linear regression as well as error analysis tools [87]. Fig. 3.17 provides the fitting result for the $LiI - Al_2O_3$ system. Table 3.1 provides the set parameters used in this work, fitted parameters from the non-linear regression, and important calculated parameters, such as percolation thresholds and theoretical maximum.

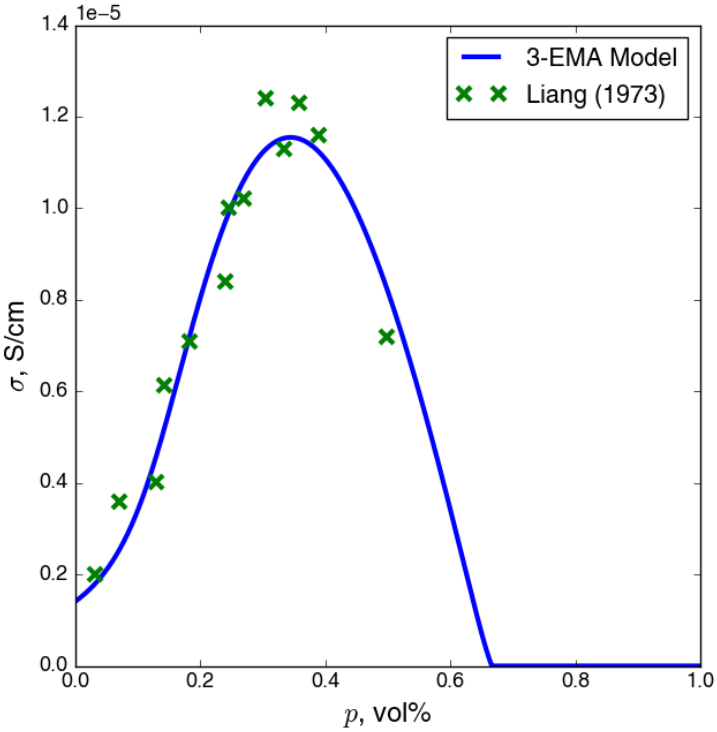

Figure 3.17: Fitting result for $LiI - Al_2O_3$ system.

With only two parameters, the model was able to provide accurate fitting of the conductivity data. The model indicates that the space charge layer conductivity is roughly 35 times higher than the pure conductor. However, in combination with the insulator, the conductivity enhancement was found to only be 8.25 times instead.

Table 3.1: Set parameters for the $LiI - Al_2O_3$ system.

Set Parameters		**Calculations**	
$\sigma_{a,\infty}$ (S/cm)	$1.4 \cdot 10^{-6}$	p_c'	0.145
$\sigma_{c,\infty}$ (S/cm)	10^{-14}	p_c''	0.667
$\varepsilon_{a,r}$	11.3	$p_{\max}$	0.345
$\varepsilon_{b,r}$	11.3	Theoretical, $\sigma_{\text{eff}}^{\max}$ (S/cm)	$2.3 \cdot 10^{-5}$
$\varepsilon_{c,r}$	9.1		
Fitted Parameters		Theoretical, $\sigma_{\text{eff}}^{\min}$ (S/cm)	$6.8 \cdot 10^{-7}$
$\sigma_{b,\infty}$ (S/cm)	$(4.7 \pm 0.4) \cdot 10^{-5}$		
η	1.61 ± 0.01		

To find whether the material can be further optimized with processing methods, the theoretical maximum and real maximum can be compared. The calculated theoretical maximum at optimal concentration ($p_{\max}$=0.345) was found to be $2.26 \cdot 10^{-5}$ S/cm which is not very far off from the optimum peak $1.15 \cdot 10^{-5}$. This shows that the material was fairly optimized in terms of processing method.

Before moving on towards impedance spectra parametric studies, the percolating behavior of the system can now be studied through the discriminant function $\Delta_{M=3}$, as shown in Fig. 3.18.a. The most interesting result can be found from the lack of minimum peak corresponding to the interface percolation. Recalling the result from the two-component system, this implied that Region I and Region II of the system has significant overlap. This result makes sense in relative to the ratio of pure conductor's conductivity and the space charge layer conductivity. To confirm the degree of overlap, the behavior of interface percolation with increasing conductivity enhancement may be found in Fig. 3.18.b. It is found that interface percolation becomes more distinguishable only if the space charge layer conductivity is 1000-5000 times higher than the pure conductor itself. The trend in the disappearance of minimum also suggests that there are different types of dispersed ionic conductors based on the degree of overlap between Region I and Region II. This observation also can be found somewhere else [38].

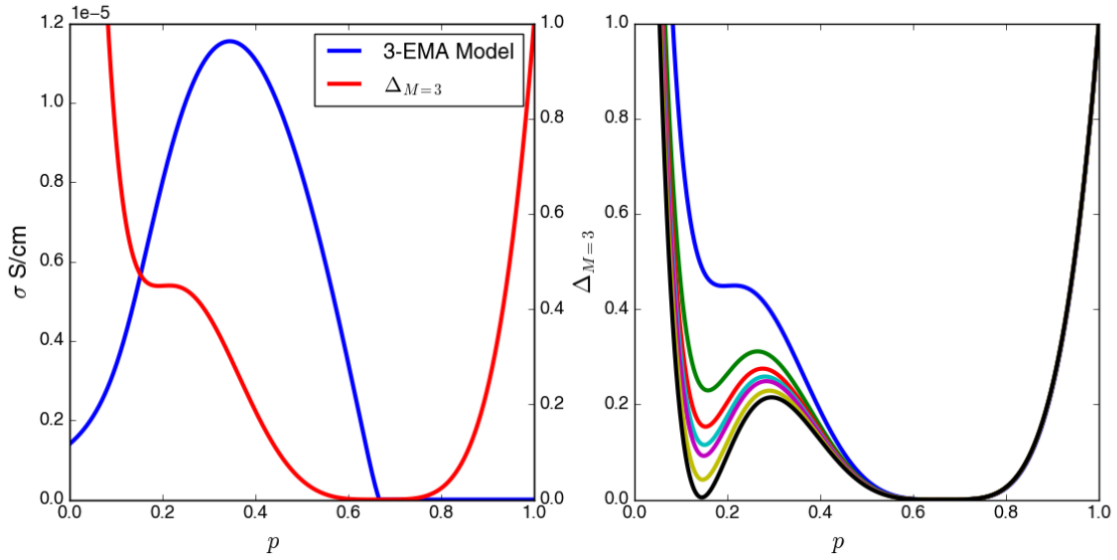

Figure 3.18: (Left) Plot of the discriminant function $\Delta_{M=3}$, normalized to its value at 100% insulator concentration, compared to the fitted curve. The model suggests that the material does not have a well-defined interface percolation, which is consistent with the space charge layer conductivity obtained. (Right) a parametric study on space charge layer conductivity and its effect to interface percolation. With increasing τ, the material starts to have a well-defined interface percolation. The interface percolation will shift more towards the conductor side.

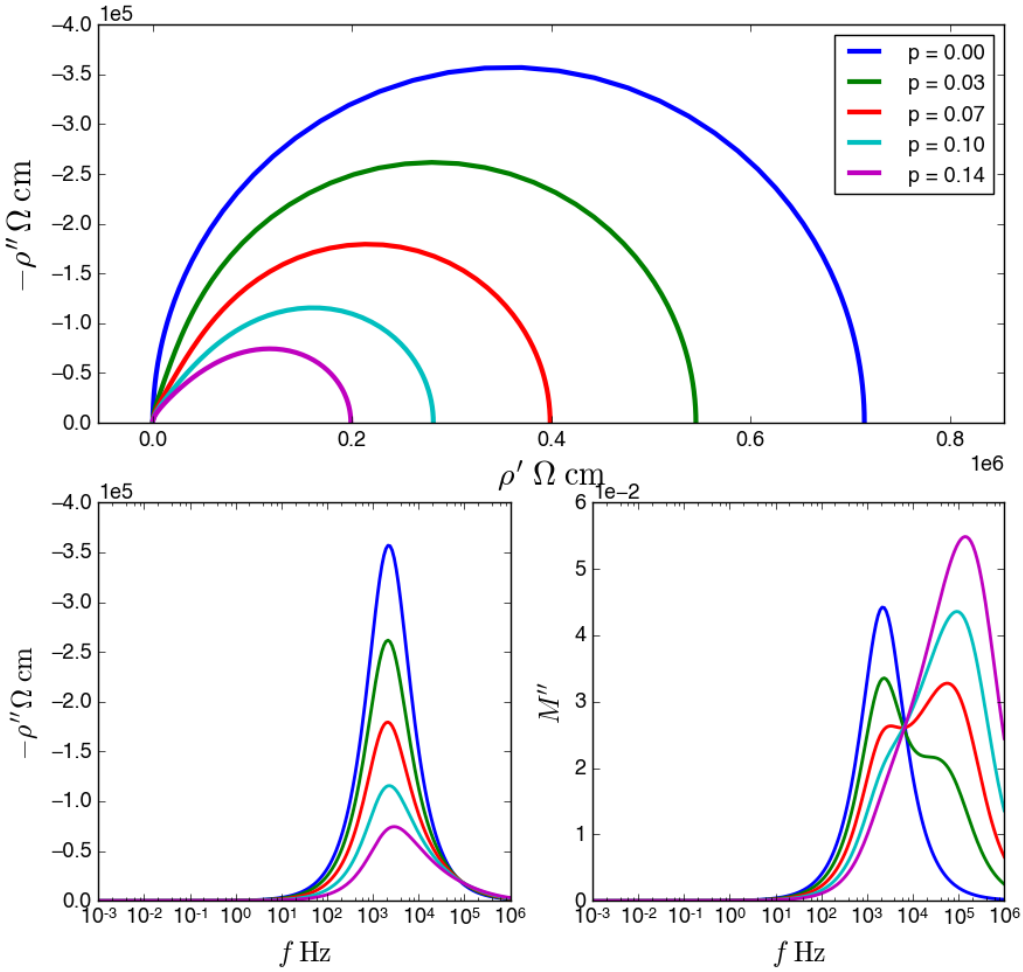

Figure 3.19: Impedance spectra, $-\rho''$ bode plot, and M'' bode plot for Region I.

Fig. 3.19 provides impedance spectra, imaginary impedance ($-\rho''$) bode plot, and imaginary modulus (M'') bode plot for Region I in the $\mathrm{LiI} - \mathrm{Al_2O_3}$. In accordance with the trend in DC conductivity, the real impedance is shown to be decreasing with more $\mathrm{Al_2O_3}$ content. Furthermore, according to the impedance spectra, the composite material retains the characteristics of the conductor at very small concentrations until an asymmetric arc was observed near the interface percolation. Looking at the modulus bode plot, two overlapping relaxation peaks can be observed starting very early but gradually before the interface percolation happens. This behavior is consistent with the previous discussion regarding the overlap of Region I and Region II based on the discriminant function found in Fig. 3.18.

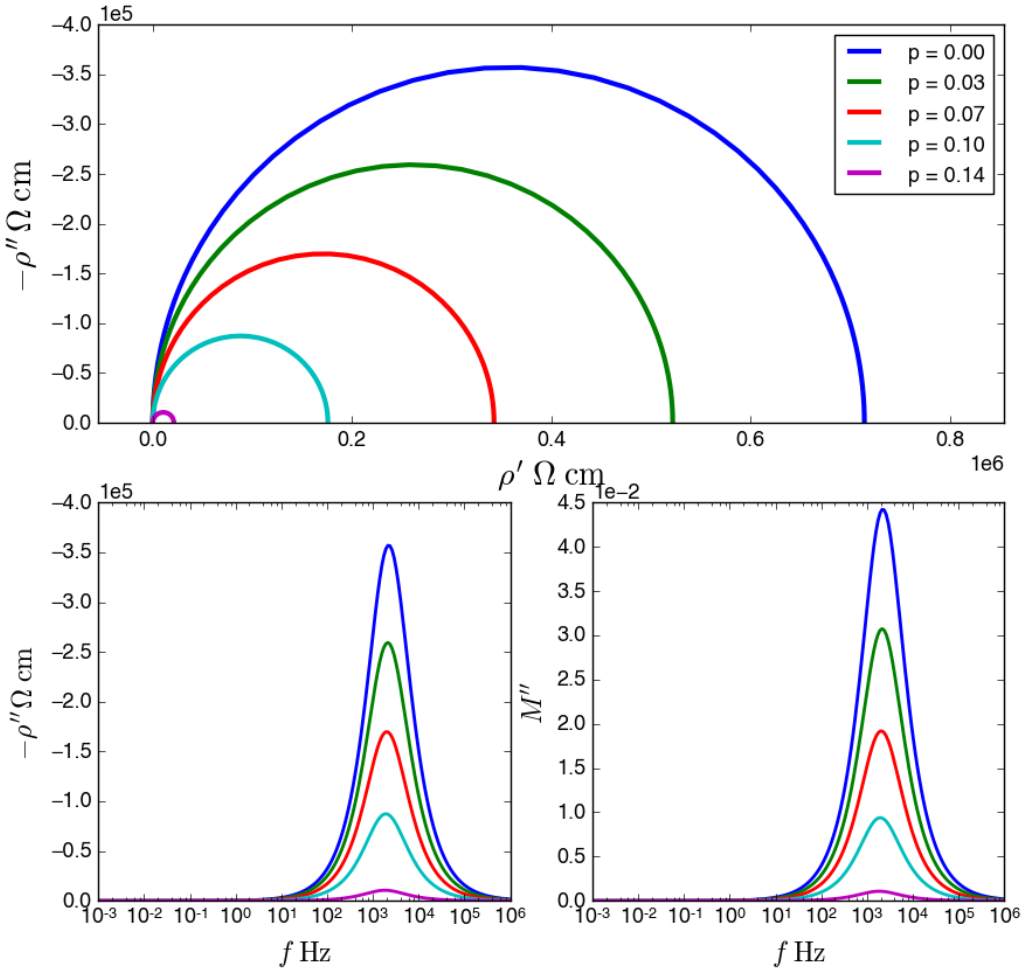

Figure 3.20: Impedance spectra, $-\rho''$ bode plot, and M'' bode plot for Region I, when ratio of space charge layer conductivity and pure conductor is very high.

Because there's an overlap between two regions, it would beneficial to observe the case in which the system has little overlap and the interface percolation p_c' is close to the calculated value found in Table 3.1. This particular case is plotted in Fig. 3.20, where the conductivity of the space charge layer is increased by 5000 times. In here, the expected behavior can be found; the semicircle arc of the conductor retains its shape up until the interface percolation. The dispersed ionic conductor still retains its characteristic frequency in the relaxation peaks while their magnitude for both $-\rho''$ and M'' decreases with more insulator content. No overlapping peaks or gradual transitions were observed in the modulus bode plot as well, indicating a proper distinction between Region I and Region II.

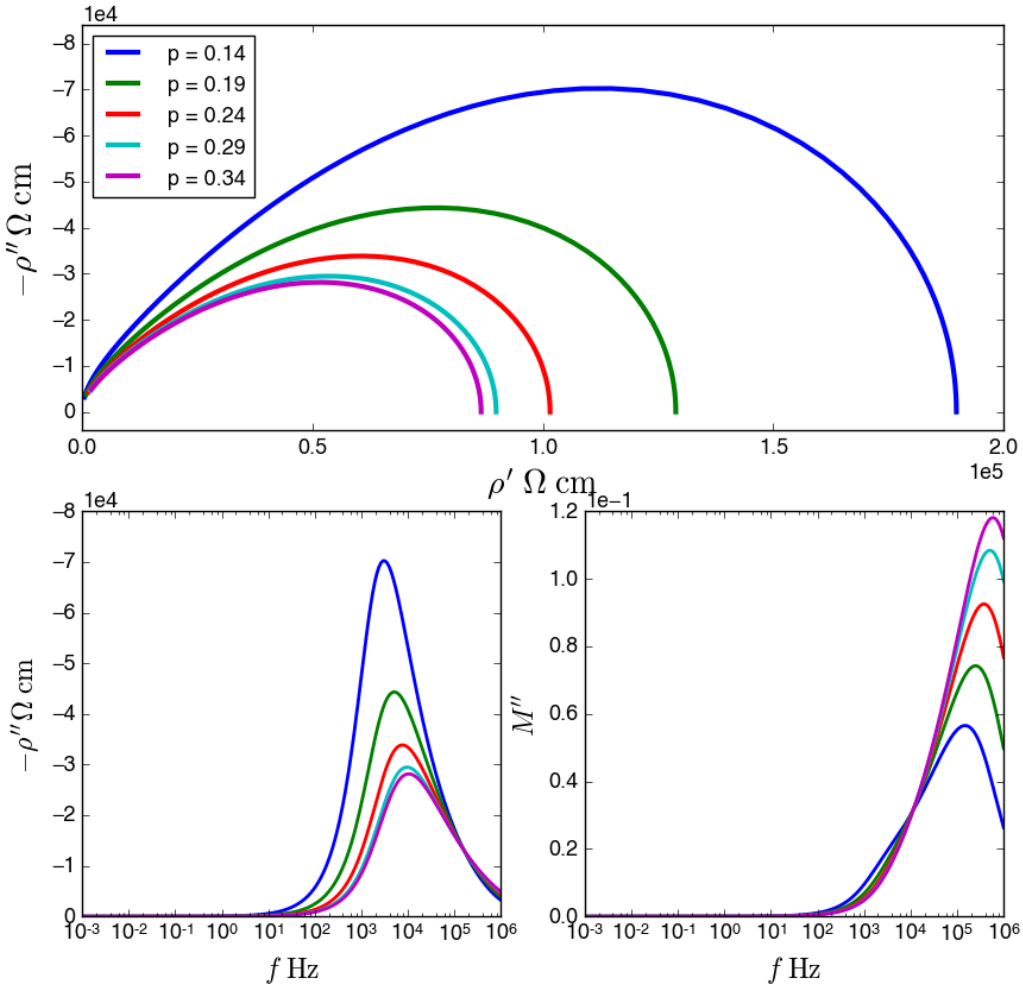

Figure 3.21: Impedance spectra, $-\rho''$ bode plot, and M'' bode plot for Region II.

Going back to the original parameters, the asymmetric impedance arc, the characteristic of Region II, becomes more noticeable as the system moves away from the interface percolation. The impedance spectra, imaginary impedance, and modulus plots can be found in Fig. 3.21. Because the asymmetric impedance arc is unique to Region II, the shape is retained for all volume concentrations before the optimum concentration. Another interesting trend to be observed is the shift of both relaxation peaks in imaginary impedance and modulus towards higher frequencies. In addition, it should be noted that the reduction in real impedance is no longer as rapid in Region I, which is expected as the composite material reaches its optimum concentration. This is merely a reflection of the change in curvature in the DC conductivity.

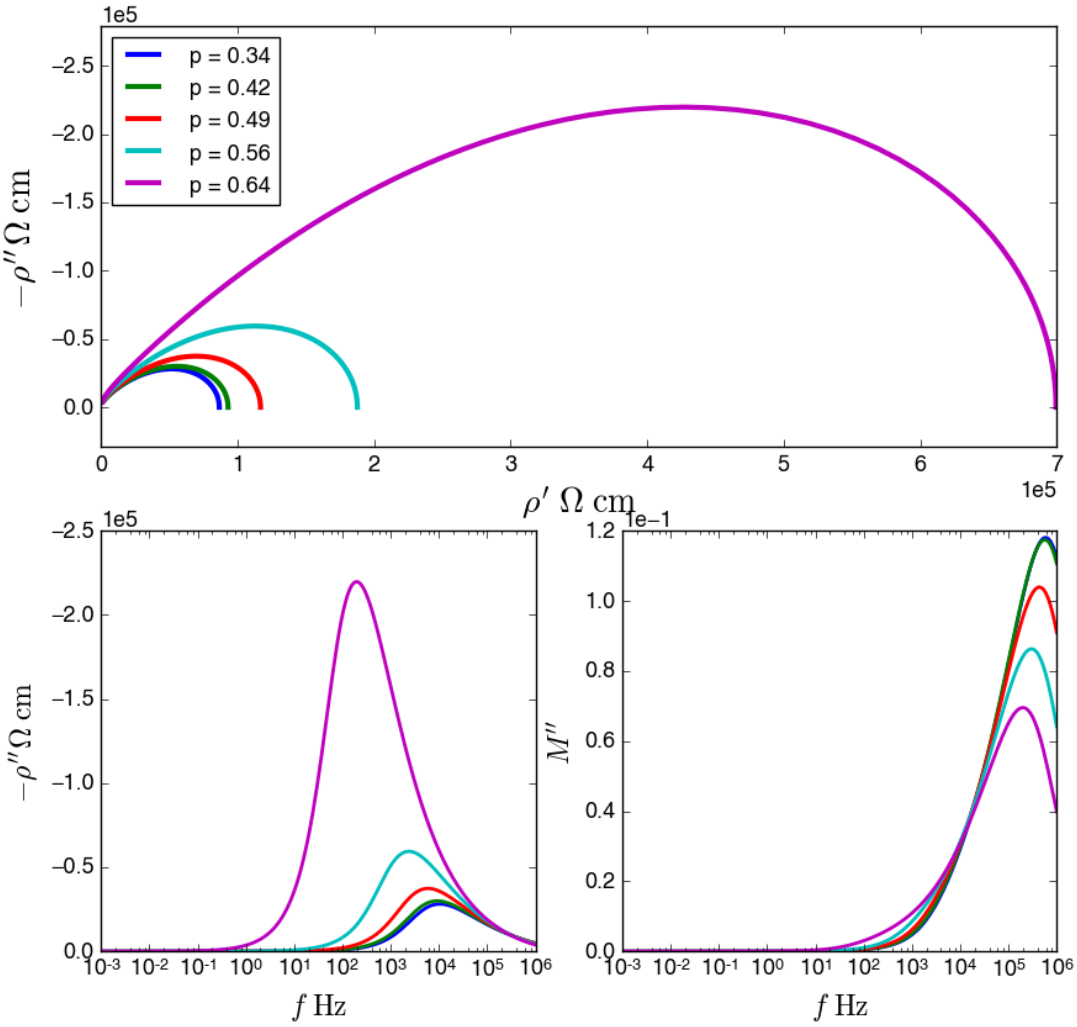

Figure 3.22: Impedance spectra, $-\rho''$ bode plot, and M'' bode plot for Region III.

The opposite trend starts to appear in Region III, as shown in Fig. 3.22. In this region, the insulator increases the real impedance at a much faster rate than the space charge layer increasing the conductivity and shifts relaxation peaks for both the imaginary impedance and modulus. The shift in relaxation peaks makes sense because to reach a capacitive behavior, the relaxation peak in the imaginary impedance must go to a lower frequency and increase in magnitude. This behavior will allow the material to reach capacitive behavior, which is the way the insulator is modeled. Similarly, the modulus behavior progresses by diminishing the magnitude of its peak as insulator concentration is increased.

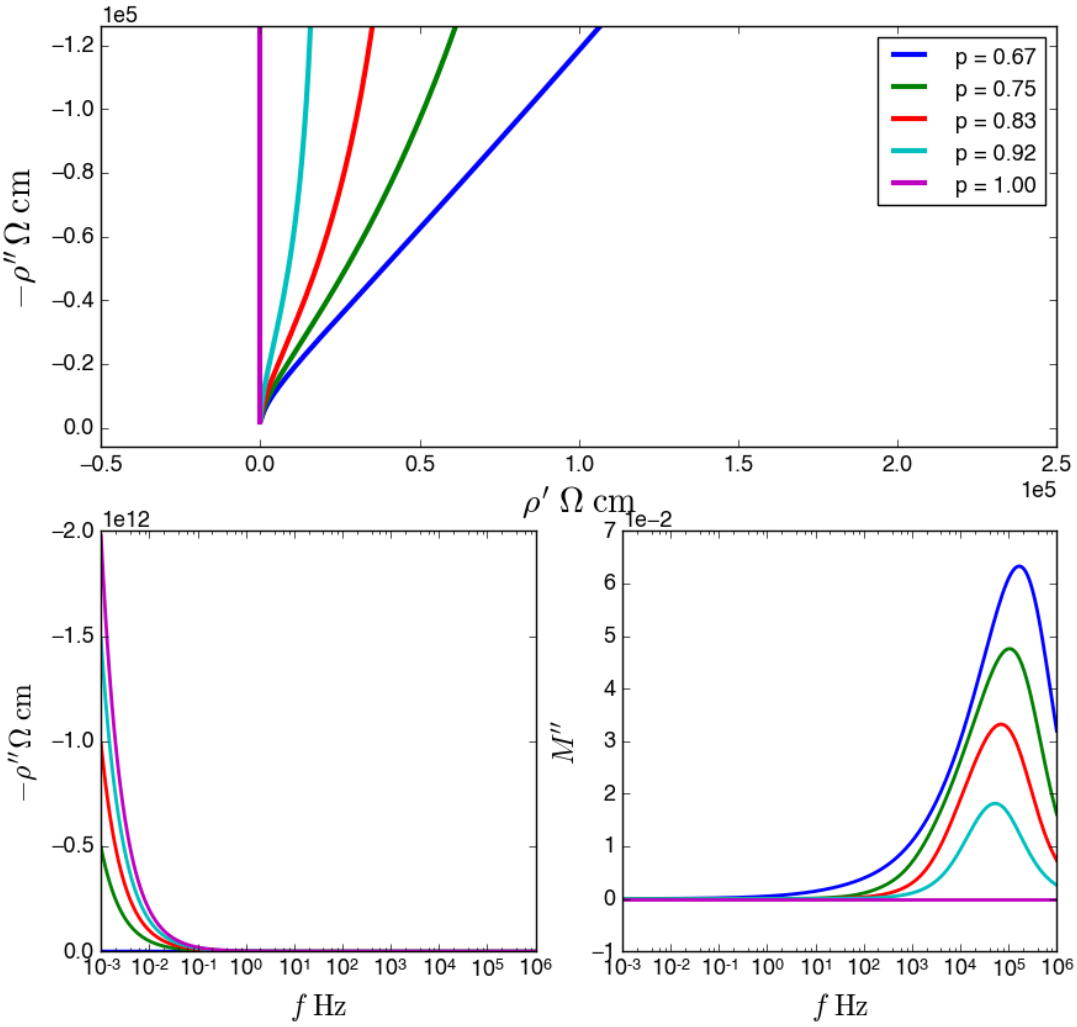

Figure 3.23: Impedance spectra, $-\rho''$ bode plot, and M'' bode plot for Region IV.

Finally, in Region IV, the material has become an insulator, as shown in Fig. 3.23. The change in phase angle since the composite material takes a phase angle of 45^o at the conductor-insulator transition, similar to a semi-infinite Warburg impedance. This particular behavior is similar to the simulation of a two-component percolating EMA for relative permittivity [84]. Once this transition is passed, the low-frequency angle starts to increase before it becomes fully 90^o, consistent with the insulator model. Due to the drastic change in phase angle, it is instructive to compile a figure that demonstrates the phase angle change starting from Region III to Region IV, ending at pure insulator. This figure can be found in Fig. 3.24

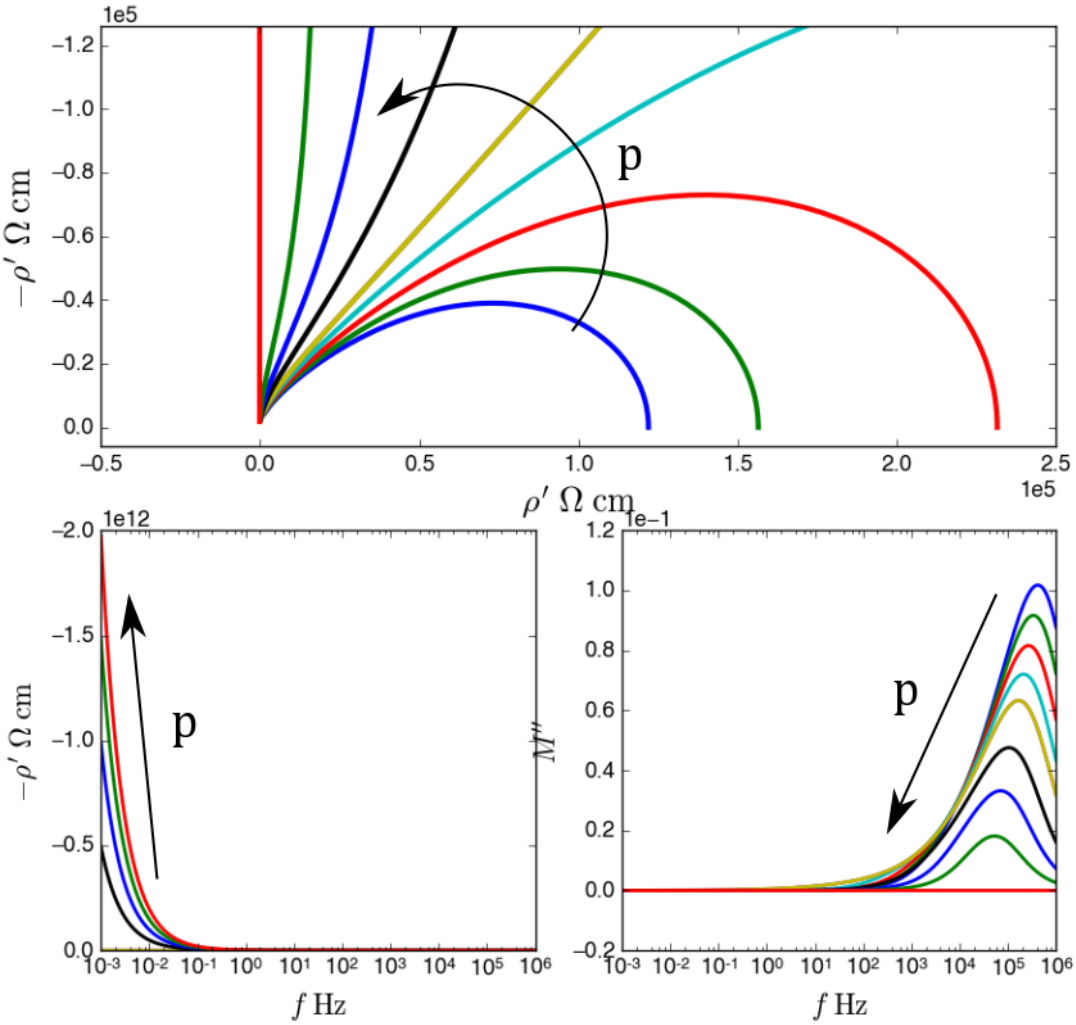

Figure 3.24: Impedance spectra, $-\rho''$ bode plot, and M'' bode plot moving from Region III to Region IV. Arrow indicates higher insulator content.

As one last comparison, it is useful to discuss the trends in the low-frequency relative permittivity as shown in Fig. 3.25. The low-frequency relative permittivity is an important data to obtain as it provides a direct evidence as to where percolation is taking place in the composite material. Both numerical and analytical solutions predicted two peaks corresponding to the interface percolation and the conductor/insulator transition respectively. These results are in agreement with early AC studies performed for percolation-based dispersed ionic conductor models [7, 8].

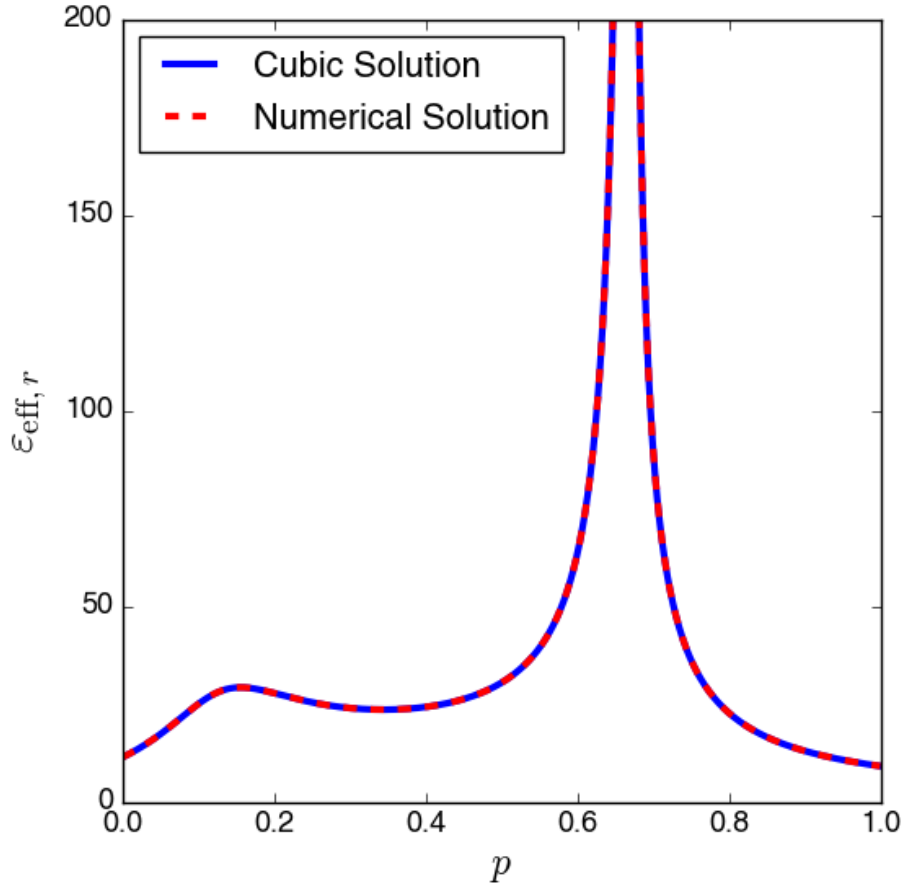

Figure 3.25: Low-frequency (1 Hz) dielectric constant/relative permittivity using the solution of the cubic equation and the numerical solution.

The impedance spectroscopy parametric studies for the $\text{LiI} - \text{Al}_2\text{O}_3$ showcase the practicality of the frequency domain EMA in assessing impedance characteristics of a dispersed ionic conductor in different regions of insulator concentrations. In particular, non-linear regression analysis on DC conductivity data can be performed to study its percolating behaviors, through the discriminant function $\Delta_{M=3}$ and assess its closeness to the optimal high conductivity using theoretical bounds. Impedance spectra simulations can be performed for all concentrations where regions of interest can be evaluated before experimentally synthesizing the composite materials.

3.5 Summary

In conclusion, a framework for deriving frequency-domain effective medium approximation (EMA) has been developed for a general composite material of an arbitrary number of components. The lattice picture in the form of random AC network is shown to be the most appropriate lattice model and has a direct correspondence with its continuum version governed by the continuum electrodynamics or Maxwell's equations. The EMA was derived using both the heuristics and lattice Green's function to elucidate both the strengths and weaknesses of the EMA being used in this work. The resulting equation to solve is in the form of a polynomial, in which the coefficients are denoted as coupling coefficients for their role in determining the mixing rule for the system, coupling the conductivity of each component, and determining the percolating behavior of the system through the discriminant function Δ_M. Specific cases were considered for 2-,3-, and 4- component systems where the coupling coefficients have been represented.

The three-component system was then used to develop the macroscopic, frequency-domain model for dispersed ionic conductors. After establishing volume fraction equations, the percolating behaviors and conductivity trends were discussed, specifically in the context of the coupling coefficients. Comments were made regarding the limited scope of the 'continuum percolation' model of dispersed ionic conductors proposed by Roman [3]. Case study application of the model was performed to the classic $\mathrm{LiI} - \mathrm{Al_2O_3}$ system, where peculiar features such as in-distinctive interface percolation or overlapping Region I and Region II, as well as frequency dispersion in impedance spectra are discussed. The combined parametric studies showcase the power of the model and the general EMA framework in modeling DC and AC characteristics of a composite material.

Appendix A

Python Code for 3-Component System

The following attached code is used to perform numerical fitting and simulation of DC conductivity data and impedance spectra using either the derived analytical solution or the `roots` function provided by Python.

```
from lmfit import *
from numpy import *
from matplotlib.pyplot import *
from scipy.optimize import *
#3 Component System, Random AC Network Model
#Material Type: Conductor Insulator Composite
#Author: Muhammad Risyad Hasyim
#Date: 03/30/2017
#Contact: mrh5506@psu.edu or muhammadrisyadh@gmail.com
#Data from Liang 1973, LiI Al2O3


#Initialize formatting
rcParams["font.family"] = "sans serif"
rcParams["font.sans serif"]="Helvetica"
rcParams["font.size"]="13"

#Reading file
```

```
19 data=loadtxt('Liang.txt')
20 DETA=data[:,1]
21
22 #MATERIAL'S PROPERTIES
23 eps0=8.8541878176*10**12 #permittivity of vacuum
24 d=3. #dimension. Set to 3 unless some 2D simulation is needed
25 z=2*d #number of bonds in the network, for a hypercubic lattice.
26
27 #Expressing the conductivities of each individual component, a, b, and c
28 #a = conductor
29 #b = space charge layer
30 #c = insulator
31 #The microscopic model for the conductivities are currently simple.
       Specialized
32 #dielectric functions such as the Lorentz model or Jonscher's Universal
       Law can
33 #also be used if one wishes.
34 om = lambda f: 2*pi*f*eps0*1j
35 def a(f,cond,epsra):
36     return cond+om(f)*epsra
37 def b(f,cond,n,epsrb):
38     return cond*n+om(f)*epsrb
39 def c(f,ins,epsrc):
40     return ins+om(f)*epsrc
41
42 #k TH ORDER COUPLING COFFICIENTS
43 def K0(z):
44     return  (z/2 1)**2
45
46 def K1(f,p,n,eta,z,cond,ins,epsra,epsrb,epsrc):
47     Pc=p
48     Pa=(1 p)**eta**d
49     Pb=1 p (1  p)**eta**d
50     q=(z/2 1)*(a(f,cond,epsra)*(z/2*Pa 1)+b(f,cond,n,epsrb)*(z/2*Pb 1)+c
       (f,ins,epsrc)*(z/2*Pc 1))
51     return q
52
53
54 def K2(f,p,n,eta,z,cond,ins,epsra,epsrb,epsrc):
55     Pc=p
```

```
56      Pa=(1 p)**eta**d
57      Pb=1 p (1  p)**eta**d
58      q=(a(f,cond,epsra)*b(f,cond,n,epsrb)*(z/2*(1 Pc) 1)+a(f,cond,epsra)*
        c(f,ins,epsrc)*(z/2*(1 Pb) 1)+b(f,cond,n,epsrb)*c(f,ins,epsrc)*(z
        /2*(1 Pa) 1))
59      return q
60
61  def K3(f,p,n,eta,z,cond,ins,epsra,epsrb,epsrc):
62      return a(f,cond,epsra)*b(f,cond,n,epsrb)*c(f,ins,epsrc)
63
64
65  #Analytical solution for a cubic polynomial using Cardano's solution
66  def cardan(f,p,n,eta,z,cond,ins,epsra,epsrb,epsrc):
67      u=empty(2,complex128)
68      v=empty(2,complex128)
69      k1=K1(f,p,n,eta,z,cond,ins,epsra,epsrb,epsrc)
70      k2=K2(f,p,n,eta,z,cond,ins,epsra,epsrb,epsrc)
71      k3=K3(f,p,n,eta,z,cond,ins,epsra,epsrb,epsrc)
72      k0=K0(z)
73      z0= k1/(3*k0)+0j
74      s=k2/(3*k0) k1*k1/(9*k0*k0)+0j
75      r=(9*k1*k2/(k0*k0) 27*k3/(k0) 2*(k1/k0)**3)/54+0j
76      u=(r+sqrt(r**2+s**3))**(1/3.)
77      v=(r  sqrt(r**2+s**3))**(1/3.)
78      sigeff=u+v+z0
79      return sigeff
80
81
82  #Quasi two component solution for the 3 component system
83  def quadratic(f,p,n,eta,z,cond,ins,epsra,epsrb,epsrc):
84      k1=K1(f,p,n,eta,z,cond,ins,epsra,epsrb,epsrc)
85      k2=K2(f,p,n,eta,z,cond,ins,epsra,epsrb,epsrc)
86      k0=K0(z)
87      sigeff=( k1  sqrt(k1**2 4*k0*k2))/(2*k0)
88      return sigeff
89
90  #Discriminant function for the 3 component system
91  def discri(f,p,n,eta,z,cond,ins,epsra,epsrb,epsrc):
92      k1=K1(f,p,n,eta,z,cond,ins,epsra,epsrb,epsrc)
93      k2=K2(f,p,n,eta,z,cond,ins,epsra,epsrb,epsrc)
```

```
94      k3=K3(f,p,n,eta,z,cond,ins,epsra,epsrb,epsrc)
95      k0=K0(z)
96      delt=(k1*k2)**2 4*k0*k2**3 4*k1**3*k3 27*k0**2*k3**2+18*k0*k2*k3*k1
97      return delt
98
99  #Numerical solution for conductivity of 3 component system
100 #Set to solve for a range of insulator concentrations under a given
        frequency
101 #Can be used for DC conductivity and low frequency dielectric constant
102 def numerical(f,p,n,eta,z,cond,ins,epsra,epsrb,epsrc):
103     sig=[roots([K0(z),K1(f,p[i],n,eta,z,cond,ins,epsra,epsrb,epsrc),
104                 K2(f,p[i],n,eta,z,cond,ins,epsra,epsrb,epsrc),
105                 K3(f,p[i],n,eta,z,cond,ins,epsra,epsrb,epsrc)])
106                 for i in range(0,len(p))]
107     sig=array(sig)
108     sig=amax(sig,axis=1)
109     return sig
110
111 #Numerical solution for the impedance of the dispersed ionic conductor
112 #Set to solve a range of frequencies under a given concentration
113 def imp(f,p,n,eta,z,cond,ins,epsra,epsrb,epsrc):
114     sig=[roots([K0(z),K1(f[i],p,n,eta,z,cond,ins,epsra,epsrb,epsrc),
115                 K2(f[i],p,n,eta,z,cond,ins,epsra,epsrb,epsrc),
116                 K3(f[i],p,n,eta,z,cond,ins,epsra,epsrb,epsrc)])
117                 for i in range(0,len(f))]
118     sig=array(sig)
119     sig=amax(sig,axis=1)
120     imp=1/sig
121     return imp
122
123 #    Fitting Procedure LMFIT   #
124 def fcn2min(params,p,K1,K2,K3,f,DETA):
125     # Defining Parameters #
126     n = params['n'].value
127     eta = params['eta'].value
128     z = params['z'].value
129     cond = params['cond'].value
130     ins = params['ins'].value
131     epsra = params['epsra'].value
132     epsrb = params['epsrb'].value
```

```
133     epsrc = params['epsrc'].value
134
135     #Fitting may be done based on numerical or analytical solution
136     #Currently uses analytical solution
137     model=cardan(f,p,n,eta,z,cond,ins,epsra,epsrb,epsrc)
138
139     #Numerical solution based fitting is commented out below:
140     #model=numerical(f,p,n,eta,z,cond,ins,epsra,epsrb,epsrc)
141     return model.real DETA
142
143 #Define fitting parameters
144 #FALSE means it's not a fitting parameter, but can be if you wish
145 params = Parameters()
146 params.add('n', 33.47,True,0,None,None) #conductivity ratio between
        space charge layer and bulk
147 params.add('eta',0.3,True,0,None,None) #dimensionless space charge layer
        thickness
148 params.add('z',6.,False,0,None,None) #number of bonds in network
149 params.add('cond',1.4e 6,False,0,None,None) #econductivity of conductor
150 params.add('ins',0,False,0,None,None) #conductivity of an insulator
151 params.add('epsra',11.3,False,0,None,None) #relative permittivity of 'a'
152 params.add('epsrb',11.3,False,0,None,None) #relative permittivity of 'b'
153 params.add('epsrc',9.1,False,0,None,None) #relative permittivity of 'c'
154
155 #Frequency and concentration taken on data. Defaulted to DC (f=0 Hz)
156 f=0
157 p=data[:,0]
158 mini = Minimizer(fcn2min,params,fcn_args=(p,K1,K2,K3,f,DETA))
159
160 #Fitting procedure + error analysis
161 out1 = mini.minimize(method='Nelder')
162 out1 = mini.minimize(method='leastsq')
163 report_fit(out1.params)
164
165 #Obtain parameters
166 n = out1.params['n'].value
167 eta = out1.params['eta'].value
168 z = out1.params['z'].value
169 cond = out1.params['cond'].value
170 ins = out1.params['ins'].value
```

```
epsra = out1.params['epsra'].value
epsrb = out1.params['epsrb'].value
epsrc = out1.params['epsrc'].value

#Solve for percolation thresholds
pc2=(1 2/(z)) #conductor/insulator transition
yeha = lambda x: 1 x (1 x)**(eta**d) 2/z
pc1=newton_krylov(yeha,0) #interface percolation

#   BASIC PLOTTING   #
#Plots that are individually generated are:
# (1) DC Conductivity with fitting result
# (2) Discriminant function
# (3) low frequency relative permittivity
# (4) An impedance spectra sampled at a range of concentrations
# It is up to you on which data to use and how you want to use them.

#(1) DC conductivity with fitting result. Analytical solution is used
#You may also use this to find real conductivity at some low frequency
figure(1)
fig = matplotlib.pyplot.gcf()
fig.set_size_inches(7,7,forward=True)
f=0 #set frequency to zero.
p=linspace(0,1,1000)

sigmaeff=cardan(f,p,n,eta,z,cond,ins,epsra,epsrb,epsrc)
#Numerical solution commented out below
#sigmaeff=numerical(f,p,n,eta,z,cond,ins,epsra,epsrb,epsrc)

plot(p,sigmaeff.real,'b',linewidth=4)
plot(data[:,0],data[:,1],'x',color='g',markersize=9,mew=3)
gca().set_ylim(bottom=0)
xlabel(r'$p$',fontsize=20)
ylabel(r'$\sigma$ S/cm',fontsize=20)
ticklabel_format(style='sci', axis='y', scilimits=(0,0))
tight_layout()

#(1) Discriminant function. Plot is normalized to its value at p=1
#Also applicable in low frequency
figure(2)
```

```
211 fig = matplotlib.pyplot.gcf()
212 fig.set_size_inches(7,7,forward=True)
213 f=0 #set frequency to zero.
214 p=linspace(0,1,1000)
215
216 discrim=discri(f,p,n,eta,z,cond,ins,epsra,epsrb,epsrc)/discri(f,1,n,eta,
        z,cond,ins,epsra,epsrb,epsrc)
217
218 plot(p,discrim,'b',linewidth=4)
219 xlabel(r'$p$',fontsize=20)
220 ylabel(r'$\Delta_{M=3}$',fontsize=20)
221 tight_layout()
222
223 #(3) low frequency dielectric permittivity. Analytical solution is used
224 #For higher frequencies (above ~100 1000 Hz) use numerical solution
225 figure(3)
226 fig = matplotlib.pyplot.gcf()
227 fig.set_size_inches(7,7,forward=True)
228 f=10 #Currently set to 10 Hz
229 p=linspace(0,1,1000)
230
231 epsreff=cardan(f,p,n,eta,z,cond,ins,epsra,epsrb,epsrc)/(2*pi*f*eps0)
232 #Numerical solution commented out below
233 #sigmaeff=numerical(f,p,n,eta,z,cond,ins,epsra,epsrb,epsrc)
234
235 plot(p,epsreff.imag,'b',linewidth=4)
236 gca().set_ylim(bottom=0)
237 xlabel(r'$p$',fontsize=20)
238 ylabel(r'$\varepsilon_r$',fontsize=20)
239 tight_layout()
240
241 #(4) An impedance spectra for a range of concentrations.
242 # Numerical solution must be used for this purpose.
243 figure(4)
244 fig = matplotlib.pyplot.gcf()
245 fig.set_size_inches(7,7,forward=True)
246 f=10**linspace(3,6,1000) #Standard range of 1 MHz to 1 mHz is used
247 p=linspace(0,pc1,5) #Looking at Region I/II
248
249
```

```
250 A=1 #Setting area of the electrolytic cell (cm^2)
251 t=0.1 #Setting thickness of the electrolytic cell (cm)
252
253 h=[None]*len(p)
254 label=h
255 for k in range(0,len(p)):
256     Z=imp(f,p[k],n,eta,z,cond,ins,epsra,epsrb,epsrc)*A/t
257     ax = plot(Z.real,Z.imag,linewidth=3)
258     h[k]=' p = %0.2f' % p[k]
259     label.append(h[k])
260 axis('equal')
261 gca().invert_yaxis()
262 xlabel(r'$Z^{\prime}$ $\mathrm{\Omega\;cm^2}$',fontsize=20)
263 ylabel(r'$ Z^{\prime}$ $\mathrm{\Omega\;cm^2}$',fontsize=20)
264 ticklabel_format(style='sci', scilimits=(0,0))
265 legend(label,loc=0,fontsize=13)
266 show()
```

Bibliography

[1] Liang, C. C. (1973) "Conduction characteristics of the lithium iodide-aluminum oxide solid electrolytes," *Journal of the Electrochemical Society*, **120**(10), p. 1289.

[2] Jow, T. and J. B. Wagner (1979) "The effect of dispersed alumina particles on the electrical conductivity of cuprous chloride," *Journal of the Electrochemical Society*, **126**(11), pp. 1963–1972.

[3] Roman, H. E. (1990) "A continuum percolation model for dispersed ionic conductors," *Journal of Physics: Condensed Matter*, **2**(17), pp. 3909–3917.

[4] Indris, S., P. Heitjans, H. E. Roman, and A. Bunde (2000) "Nanocrystalline versus microcrystalline $Li_2O:B_2O_3$ composites: anomalous ionic conductivities and percolation theory," *Physical Review Letters*, **84**(13), pp. 2889–2892.

[5] Maier, J. (1984) "Enhancement of the ionic conductivity in solid-solid-dispersions by surface induced defects," *Berichte der Bunsengesellschaft für Physikalische Chemie*, **88**(11), pp. 1057–1062.

[6] Roman, E. R. and M. Yussouff (1987) "Particle-size effect on the conductivity of dispersed ionic conductors," *Physical Review B - Condensed Matter and Materials Physics*, **36**(13), pp. 7285–7288.

[7] Cáceres, M. O. and E. R. Reyes (1996) "AC conductivity in dispersed ionic conductors: the effective medium approximation," *Physica A: Statistical Mechanics and Its Applications*, **227**, pp. 277–290.

[8] Blender, R. and W. Dieterich (1987) "A random AC network model for dispersed ionic conductors," *Journal of Physics C: Solid State Physics*, **20**, pp. 6113–6126.

[9] van der Pol, B. (1957) "The finite difference analogy of the periodic wave equation and the potential equation," in *Probability and Related Topics in Phys-*

ical Sciences (A. S. Householder, M. Kac, and H. Greenberg, eds.), 1 ed., chap. Appendix IV, Interscience Publishers, New York, pp. 237–257.

[10] Murugan, R., V. Thangadurai, and W. Weppner (2007) "Fast lithium ion conduction in garnet-type $Li_7La_3Zr_2O_{12}$," *Angewandte Chemie - International Edition*, **46**(41), pp. 7778–7781.

[11] Thangadurai, V., H. Kaack, and W. J. F. Weppner (2003) "Novel fast lithium ion conduction in garnet-type $Li_5La_3M_2O_{12}$ (M = Nb,Ta)," *Journal of the American Ceramic Society*, **86**(3), pp. 437–440.

[12] Kanno, R. and M. Murayama (2001) "Lithium ionic conductor thio-LISICON: the $Li_2S - GeS_2 - P_2S_5$ system," *Journal of the Electrochemical Society*, **148**(7), p. A742.

[13] Mizuno, F., A. Hayashi, K. Tadanaga, and M. Tatsumisago (2005) "New, highly ion-conductive crystals precipitated from $Li_2S - P_2S_5$ glasses," *Advanced Materials*, **17**(7), pp. 918–921.

[14] Inaguma, Y., C. Liquan, M. Itoh, T. Nakamura, T. Uchida, H. Ikuta, and M. Wakihara (1993) "High ionic conductivity in lithium lanthanum titanate," *Solid State Communications*, **86**(10), pp. 689–693.

[15] Mei, A., X. L. Wang, J. L. Lan, Y. C. Feng, H. X. Geng, Y. H. Lin, and C. W. Nan (2010) "Role of amorphous boundary layer in enhancing ionic conductivity of lithium-lanthanum-titanate electrolyte," *Electrochimica Acta*, **55**(8), pp. 2958–2963.

[16] Alamo, J. (1993) "Chemistry and properties of solids with the [NZP] skeleton," *Solid State Ionics*, **63**, pp. 547–561.

[17] Aono, H., E. Sugimoto, Y. Sadaoka, N. Imanaka, and G. Y. Adachi (1992) "Electrical-properties and sinterability of lithium germanium phosphate $Li_{1+x}M_xGe_{2-x}(PO_4)_3$, M=Al, Cr, Ga, Fe, Sc, and In systems," *Bulletin of the Chemical Society of Japan*, **65**(8), pp. 2200–2204.

[18] Bruce, P. G. and A. R. West (1983) "The A-C conductivity of polycrystalline LISICON, $Li_{2+2x}Zn_{1-x}GeO_4$, and a model for intergranular constriction resistances," *Journal of the Electrochemical Society*, **130**(3), pp. 662–669.

[19] Kamaya, N., K. Homma, Y. Yamakawa, M. Hirayama, R. Kanno, M. Yonemura, T. Kamiyama, Y. Kato, S. Hama, K. Kawamoto, and A. Mitsui (2011) "A lithium superionic conductor." *Nature Materials*, **10**(9), pp. 682–686.

[20] Bron, P., S. Johansson, K. Zick, a. d. G. Jörn, S. Dehnen, and B. Roling (2013) "$Li_{10}SnP_2S_{12}$: An affordable lithium superionic conductor," *Journal of the American Chemical Society*, **135**(42), pp. 15694–15697.

[21] Kuhn, A., O. Gerbig, C. Zhu, F. Falkenberg, J. Maier, and B. V. Lotsch (2014) "A new ultrafast superionic Li-conductor: ion dynamics in $Li_{11}Si_2PS_{12}$ and comparison with other tetragonal LGPS-type electrolytes." *Physical Chemistry Chemical Physics*, **16**(28), pp. 14669–74.

[22] Kato, Y., S. Hori, T. Saito, K. Suzuki, M. Hirayama, A. Mitsui, M. Yonemura, H. Iba, and R. Kanno (2016) "High-power all-solid-state batteries using sulfide superionic conductors," *Nature Energy*, **1**(16030), pp. 1–7.

[23] Maier, J. (1995) "Ionic conduction in space charge regions," *Progress in Solid State Chemistry*, **23**(3), pp. 171–263.

[24] Shahi, K. and J. B. Wagner (1981) "Ionic conductivity and thermoelectric power of pure andAl_2O_3-dispersed AgI," *Journal of the Electrochemical Society*, **128**(1), pp. 6–13.

[25] Fujitsu, S., M. Miyayama, K. Koumoto, H. Yanagida, and T. Kanazawa (1985) "Enhancement of ionic conduction in CaF_2 and BaF_2 by dispersion of Al_2O_3," *Journal of Materials Science*, **20**(6), pp. 2103–2109.

[26] Knauth, P. (2000) "Ionic conductor composites: theory and materials," *Journal of Electroceramics*, **5**(2), pp. 111–125.

[27] Agrawal, R. C. and R. K. Gupta (1999) "Superionic solids: composite electrolyte phase - an overview," *Journal of Materials Science*, **34**(6), pp. 1131–1162.

[28] Islam, M. M., T. Bredow, S. Indris, and P. Heitjans (2007) "Enhanced conductivity at the interface of Li_2O:B_2O_3 nanocomposites: atomistic models," *Physical Review Letters*, **99**(14), p. 145502.

[29] Mei, A., X. L. Wang, Y. C. Feng, S. J. Zhao, G. J. Li, H. X. Geng, Y. H. Lin, and C. W. Nan (2008) "Enhanced ionic transport in lithium lanthanum titanium oxide solid state electrolyte by introducing silica," *Solid State Ionics*, **179**(39), pp. 2255–2259.

[30] Zhu, B., Z. H. Lai, and B. E. Mellander (1994) "Structure and ionic conductivity of lithium sulphate aluminum oxide ceramics," *Solid State Ionics*, **70-71**(PART 1), pp. 125–129.

[31] Stoneham, A. M., E. Wade, and J. A. Kilner (1979) "A model for the fast ionic diffusion in alumina-doped LiI," *Materials Research Bulletin*, **14**(5), pp. 661–666.

[32] Maier, J. (1985) "Space charge regions in solid two-phase systems and their conduction contribution-I. Conductance enhancement in the system ionic conductor-'inert' phase and application on AgC1:Al_2O_3 and AgC1:SiO_2," *Journal of Physics and Chemistry of Solids*, **46**(3), pp. 309–320.

[33] Maier, J. (1986) "On the conductivity of polycrystalline materials," *Berichte der Bunsengesellschaft für Physikalische Chemie*, **90**, pp. 26–33.

[34] Maier, J. (1987) "Composite electrolytes," *Materials Chemistry and Physics*, **17**(5), pp. 485–498.

[35] Maier, J. (1985) "Space charge regions in solid two phase systems and their conduction contributionII Contact equilibrium at the interface of two ionic conductors and the related conductivity effect," *Berichte der Bunsengesellschaft für physikalische Chemie*, **89**(4), pp. 355–362.

[36] Goodyer, C. E., J. S. Fish, J. D. Fehribach, R. O'Hayre, and A. L. Bunge (2011) "Modeling space charge layer interaction and conductivity enhancement in nanoionic composites," *Electrochimica Acta*, **56**(25), pp. 9295–9302.

[37] Fish, J. S., C. P. Li, J. D. Fehribach, C. A. Wolden, R. O'Hayre, A. L. Bunge, and C. E. Goodyer (2012) "Poisson-Boltzmann model of space charge layer effects on conductivity in randomly distributed nanoionic composites," *Electrochimica Acta*, **83**, pp. 454–462.

[38] Brailsford, A. D. (1986) "A phenomenological classification of the electrical conductivity of dispersed solid electrolyte systems," *Solid State Ionics*, **21**(2), pp. 159–169.

[39] Jiang, S. and J. Wagner (1995) "A theoretical model for composite electrolytesI. Space charge layer as a cause for charge-carrier enhancement," *Journal of Physics and Chemistry of Solids*, **56**(8), pp. 1101–1111.

[40] Bjorkstam, J. L., M. Villa, M. Rahman, and P. M. Skarstad (1983) "Lithium-ion diffusion and water molecule reorientations in lithium iodide monohydrate," *Solid State Ionics*, **9-10**(Part 1), pp. 111–118.

[41] Finch, D. S. and J. B. Wagner (1993) "Composite electrolytes with special reference to the copper chloride - alumina system," in *Fast Ion Transport in Solids* (B. Scrosati, A. Magistris, C. Mari, and G. Mariotto, eds.), Kluwer Academic Publishers, p. 291.

[42] Roman, H., A. Bunde, and W. Dieterich (1986) "Conductivity of dispersed ionic conductors: a percolation model with two critical points," *Physical Review B - Condensed Matter and Materials Physics*, **34**(5), pp. 3439–3445.

[43] Rojo, A. and H. E. Roman (1988) "Effective-medium approach for the conductivity of dispersed ionic conductors," *Physical Review B - Condensed Matter and Materials Physics*, **37**(7), pp. 3696–3698.

[44] Nan, C.-W. (1987) "Conduction theory of ionic conductor containing dispersed second phase," *Acta Physica Sinica*, **36**(2), pp. 191–198.

[45] Ma, Y.-Q. and Li-Zhen-Ya (1990) "Effective-medium theory for two-phase random composite/system," *Acta Physica Sinica*, **39**(3), pp. 457–463.

[46] Nan, C.-W. and D. M. Smith (1991) "A.c. electrical properties of composite solid electrolytes," *Materials Science and Engineering: B*, **10**(2), pp. 99–106.

[47] Guo, X., I. Matei, J. Jamnik, J. S. Lee, and J. Maier (2007) "Defect chemical modeling of mesoscopic ion conduction in nanosized CaF_2/BaF_2 multilayer heterostructures," *Physical Review B - Condensed Matter and Materials Physics*, **76**(12), pp. 1–7.

[48] Hasyim, M. R., S. S. Berbano, R. M. Cleary, M. T. Lanagan, and D. K. Agrawal (2017) "Impedance spectroscopy modeling of lithium borate with silica: A dispersed ionic conductor system," *Ceramics International*, **43**(9), pp. 6796 – 6806.

[49] Wohlmuth, D., V. Epp, B. Stanje, A.-M. Welsch, H. Behrens, and M. Wilkening (2016) "High-energy mechanical treatment boosts ion transport in nanocrystalline$Li_2B_4O_7$," *Journal of the American Ceramic Society*, **9**(5), pp. 1687–1693.

[50] Sastry, B. S. R. and F. A. Hummel (1958) "Studies in lithium oxide systems: v, $Li_2O - B_2O_3.B_2O_3$," *Journal of the American Ceramic Society*, **41**(1), pp. 7–17.

[51] Sastry, B. S. R. and F. A. Hummel (1960) "Studies in lithium oxide systems: vii,Li_2O-B_2O_3-SiO_2," *Journal of the American Ceramic Society*, **43**(1), pp. 23–33.

[52] Raistrick, I. D., D. R. Franceschetti, and J. R. Macdonald (2005) "The electrical analogs of physical and chemical processes," in *Impedance Spectroscopy: Theory, Experiment, and Applications* (E. Barsoukov and J. R. Macdonald, eds.), Wiley, pp. 72–74.

[53] Bonanos, N., B. Steele, and E. Butler (2005) "Characterization of materials," in *Impedance Spectroscopy: Theory, Experiment, and Applications* (E. Barsoukov and J. R. Macdonald, eds.), 2 ed., chap. 4, Wiley, pp. 213–214.

[54] Guangling, S. (2000) "Equivalent circuit model for AC electrochemical impedance spectroscopy of concrete," *Cement and Concrete Research*, **30**(11), pp. 1723–1730.

[55] Christensen, B. J., T. Coverdale, R. a. Olson, S. J. Ford, E. J. Garboczi, H. M. Jennings, and T. O. Mason (1994) "Impedance spectroscopy of hydrating cement-based materials: measurement, interpretation, and application," *Journal of the American Ceramic Society*, **77**(11), pp. 2789–2804.

[56] Kim, S., J. Fleig, and J. Maier (2003) "Space charge conduction: simple analytical solutions for ionic and mixed conductors and application to nanocrystalline ceria," *Physical Chemistry Chemical Physics*, **5**(11), pp. 2268–2273.

[57] Jamnik, J. (1999) "Treatment of the impedance of mixed conductors equivalent circuit model and explicit approximate solutions," *Journal of the Electrochemical Society*, **146**(11), p. 4183.

[58] Franceschetti, D. R. and J. R. Macdonald (1977) "Electrode kinetics, equivalent circuits, and system characterization: small-signal conditions," *Journal of Electroanalytical Chemistry and Interfacial Electrochemistry*, **82**(1-2), pp. 271–301.

[59] Fricke, H. (1932) "XXXIII. The theory of electrolytic polarization," *Philosophical Magazine Series 7*, **14**(90), pp. 310–318.

[60] Fricke, H. (1953) "The Maxwell-Wagner dispersion in a suspension of ellipsoids," *Journal of Physical Chemistry*, **57**(9), pp. 934–937.

[61] Raistrick, I., C. Ho, and R. Huggins (1976) "Ionic Conductivity of some lithium silicates and aluminosilicates," *Journal of the Electrochemical Society*, **123**(10), pp. 1469–1476.

[62] Button, D. P., L. S. Mason, H. L. Tuller, and D. R. Uhlmann (1983) "Structural disorder and enhanced ion transport in amorphous conductors," *Solid State Ionics*, **9-10**, pp. 585–592.

[63] Jacob, M. M. E., S. Rajendran, R. Gangadharan, M. S. Michael, and S. R. S. Prabaharan (1996) "Effect of dispersion of CeO_2 in the ionic conductivity of Li_2MnCl_4," *Solid State Ionics*, **86-88**(PART 1), pp. 595–602.

[64] Nishino, M. T. (1994) "Fabrication of Li3PO4-Al_2O_3 composites by an electrochemical technique," *Solid State Ionics*, **70/71**, pp. 96–100.

[65] Kirkpatrick, S. (1973) "Percolation and conduction," *Reviews of Modern Physics*, **45**(4), pp. 574–588.

[66] Summerfield, S. (1981) "Effective medium theory of a.c. hopping conductivity for random-bond lattice models," *Solid State Communications*, **39**(3), pp. 401–402.

[67] Odagaki, T. and M. Lax (1981) "Coherent-medium approximation in the stochastic transport theory of random media," *Physical Review B - Condensed Matter and Materials Physics*, **24**(9), pp. 5284–5294.

[68] Bustingorry, S., M. O. Cáceres, and E. R. Reyes (2002) "Effective-medium approximation with asymmetric transition rates," *Physical Review B - Condensed Matter and Materials Physics*, **65**(16), pp. 1652051–1652058.

[69] Lax, M. and T. Odagaki (1984) "Hopping conduction from multiple scattering theory and continuous time random walk to the coherent medium approximation," *AIP Conference Proceedings*, **109**, pp. 133–154.

[70] Dyre, J. C. (1993) "Universal low-temperature ac conductivity of macroscopically disordered nonmetals," *Physical Review B - Condensed Matter and Materials Physics*, **48**(17), pp. 12511–12526.

[71] Stroud, D. (1998) "The effective medium approximations: Some recent developments," *Superlattices and Microstructures*, **23**(3-4), pp. 567–573.

[72] Stroud, D. (1975) "Generalized effective-medium approach to the conductivity of an inhomogeneous material," *Physical Review B - Condensed Matter and MaterialsPhysics*, **12**(8), p. 3368.

[73] van der Pol, B. and H. Bremmer (1987) *Operational Calculus Based on the Two-Sided Laplace Integral*, 3 ed., Chelsea Publishing Company, New York.

[74] Turban, L. (1978) "On the effective-medium approximation for bond-percolation conductivity," *Journal of Physics C: Solid State Physics*, **11**(3), p. 449.

[75] Ahmed, G. and J. A. Blackman (1976) "A theory of conductivity in disordered resistor networks," *Journal of Physics C: Solid State Physics*, **9**, pp. 2049–2071.

[76] Blackman, J. (1979) "On theories of transport in disordered media," *Journal of Physics C: Solid State Physics*, **12**(1979), pp. 837–853.

[77] Nagatani, T. (1981) "Multi-bond expansions for the effective conductivity in bond-disordered resistor networks," *Journal of Physics C: Solid State Physics*, **14**, pp. 4839–4847.

[78] Nagatani, T. (1981) "A two-bond theory of conductivity in bond-disordered resistor networks," *Journal of Physics C: Solid State Physics*, **14**(23), p. 3383.

[79] Nagatani, T. (1983) "Disordered resistor network approach to the effective conductivity in inhomogeneous continua with substitutional disorder," *Journal of Applied Physics*, **54**(9), pp. 5132–5138.

[80] Choy, T. C. (2016) *Effective Medium Theory: Principles and Application*, 3 ed., Oxford Science Publications.

[81] Vergu, C. (2007) "Factorization of the connected prescription for Yang-Mills amplitudes," *Physical Review D*, **75**(2), p. 025028.

[82] Johansson, H., D. A. Kosower, and K. J. Larsen (2012) "An overview of maximal unitarity at two loops," *ArXiv e-prints*, 1212.2132.

[83] Brewster, R. A. and J. D. Franson (2016) "Generalized Delta functions and their use in quasi-probability distributions," *ArXiv e-prints*, 1605.04321.

[84] Clerc, J., G. Giraud, J. Laugier, and J. Luck (1990) "The electrical conductivity of binary disordered systems, percolation clusters, fractals and related models," *Advances in Physics*, **39**(3), pp. 191–309.

[85] Bruggeman, V. D. (1935) "Berechnung verschiedener physikalischer Konstanten von heterogenen Substanzen. I. Dielektrizitätskonstanten und Leitfähigkeiten der Mischkörper aus isotropen Substanzen," *Annalen der physik*, **416**(7), pp. 636–664.

[86] Abramowitz, M. and I. A. Stegun (1964) *Handbook of mathematical functions: with formulas, graphs, and mathematical tables*, vol. 55, Courier Corporation.

[87] Newville, M., T. Stensitzki, D. B. Allen, and A. Ingargiola (2014), "LMFIT: Non-Linear Least-Square Minimization and Curve-Fitting for Python," .

Muhammad Risyad Hasyim

Address: 201 Vairo Boulevard, 344 K Building, State College, PA 16803; Phone (Home): +1-814-880-7787;
E-mail: mrh5506@psu.edu; LinkedIn profile: http://www.linkedin.com/in/mrh5505

EDUCATION

THE PENNSYLVANIA STATE UNIVERSITY, University Park, PA — Graduation, **May 2017**
Bachelor of Science, *Chemical Engineering (Honors)* — *GPA: 3.97/4.00*
Bachelor of Science, Engineering Science (Honors) — *Minor: Mathematics*

REYKJAVIK UNIVERSITY, Reykjavik**,** Iceland — 05/14 – 06/14
The GREEN Program

- Short-term study abroad program on renewable energy at Reykjavik University's School of Science and Engineering with visitations to geothermal, biomass, and hydroelectric facilities.

RESEARCH EXPERIENCE

DR. RAMAKRISHNAN RAJAGOPALAN RESEARCH GROUP — University Park, PA
Undergraduate Researcher — *05/16 – Present*

- Conducting chemical engineering honors thesis project titled "Mathematical Modeling of Electrochemical Capacitors".
- Verify newly-built mathematical models on a working symmetric MnO_2 pseudocapacitor with electrochemical impedance spectroscopy and charge/discharge experiments (chronopotentiometry).
- Connect theory and experiments by building Python programs to perform complex non-linear regression on impedance data and numerical inverse Laplace transform for simulation.

PPG/MRI Undergraduate Research Fellowship Program 2016 — *05/16 – 08/16*

- Awarded summer research funds and stipend by the PPG Industries and the Materials Research Institute for the development of polymeric coatings on alkali-free thin glasses and characterization using infrared spectroscopy (ATR-IR) and scanning electron microscopy (SEM).
- Presented research findings in oral and poster presentation at the 8th Annual Penn State REU/RET Symposium 2016, University Park, PA.

College of Engineering Research Initiative (CERI) REU 2016 — *01/16 – 05/16*

- Awarded research stipend by the College of Engineering to test $LaNiO_3$ as possible candidate for pseudocapacitive materials and evaluate its electrochemical properties with voltammetry techniques.
- Won the Peter T. Luckie award for best research in engineering and physical science category by a junior at the poster presentation session at the 2016 Undergraduate Exhibition, University Park, PA.

DR. MICHAEL LANAGAN RESEARCH GROUP — University Park, PA
Undergraduate Researcher — *09/14 – Present*

- Conducting engineering science honors thesis project titled "Experimental Studies and Modeling of Lithium Borate/Silica Composite Solid Electrolyte".
- Perform characterization with scanning electron microscopy (SEM), x-ray diffraction (XRD), and energy dispersive x-ray spectroscopy (EDS) coupled with impedance spectroscopy to model material's conductivity.
- Presented research findings in 12th (2014) and 13th (2015) Annual College of Engineering Research Symposiums, University Park, PA.

TECHNISCHE UNIVERSITÄT BRAUNSCHWEIG, INSTITUT FÜR PARTIKELTECHNIK — Braunschweig, Germany
Research Intern — *06/15 – 08/15*

- Awarded funds by DAAD (*Deutscher Akademischer Austauschdienst* or German Academic Exchange Service) to conduct research in non-aqueous synthesis and *in-situ* stabilization of TiO_2 nanoparticle dispersions.
- Performed characterizations on dispersion stability with dynamic light scattering (DLS) and coating thickness with surface profilometry.

MODELING PROJECTS

STOCHASTIC DIFFERENTIAL EQUATIONS IN GENE CIRCUITS *04/16 – 05/16*

MATH 450 – Mathematical Modeling

- Explored and applied stochastic differential equations (SDEs) as chemical Langevin equations to model molecular noise in simple chemical reactions and the 'repressilator' model from gene circuits.
- Developed a Python program to simulate the system of SDEs with their corresponding deterministic ones, and experiment on the dimensional scaling of those equations.

NONLINEAR SCHRÖDINGER EQUATION AND INVERSE SCATTERING TRANSFORM *04/16 – 05/16*

MATH 412 – Fourier Series and Partial Differential Equations

- Developed a Python program to simulate the 1D nonlinear Schrödinger equation with a simple finite difference method to produce bright soliton solutions.
- Explored the mathematics of the inverse scattering transform and its application in deriving the 1D soliton solution of the nonlinear Schrödinger equation.

THE MCM 1995, PROBLEM A: THE SINGLE HELIX PROBLEM *03/16 – 04/16*

MATH 450 – Mathematical Modeling

- Tasked to compute all intersections of a helix going through a plane in any location and any orientation in space, a problem statement from the 1995 Mathematical Contest in Modeling.
- Developed and tested a MATLAB program to compute such intersections by using rotational matrices and independently analyzing the geometrical properties of intersecting helices.

TECHNICAL SKILLS

MATERIALS/ELECTROCHEMICAL CHARACTERIZATION: Scanning electron microscopy (SEM), energy dispersive x-ray spectroscopy (EDS), x-ray diffraction (XRD), infrared spectroscopy (IR), dynamic light scattering (DLS), surface profilometry, impedance spectroscopy (IS), cyclic voltammetry (CV), and chronopotentiometry.

MATERIALS SYNTHESIS: Ceramics fabrication processes for crystalline and amorphous materials. Aqueous and non-aqueous sol-gel techniques for various metal oxides. Surface chemical modifications and coating strategies.

MODELING: Development of systems of ordinary and partial differential equations in the context of transport phenomena and electrochemistry. Numerical methods for simulations of partial, ordinary, and stochastic differential equations. Data fitting with complex non-linear regression.

PROGRAMMING: Fluency in Python, MATLAB, and Mathematica for scientific and numerical programming and LaTeX for manuscript and presentation preparation. Basics in C/C++.

HONORS AND AWARDS

EXCEPTIONAL STUDENT ASSISTANCE 2013 SCHOLARSHIP PROGRAM: Full-time Indonesian scholarship in the amount of $45,000 per year by Chevron Pacific Indonesia to study abroad for 4.5 years.

PETER T. LUCKIE AWARD FOR EXCELLENCE IN ENGINEERING AND PHYSICAL SCIENCE 2016: Awarded for best research by a junior in the engineering and physical science category at the 2016 Undergraduate Exhibition for the work titled: *Electrochemical Evaluation of $LaNiO_3$/Carbon Composite for Aqueous Asymmetric Capacitors.*

THE PRESIDENT SPARKS AWARD: Successfully maintained a 4.00 cumulative GPA completed by the end of the fall semester of the second academic year.

THE PRESIDENT'S FRESHMAN AWARD: Successfully maintained a 4.00 cumulative GPA completed by the end of the fall semester of the first academic year.

DEAN'S LIST

SENIOR DESIGN PROJECT

SORBITOL CONVERSION TO GLYCOLS *08/16 – 12/16*

CHE 470 – Design of Chemical Plants

- Tasked to explore and evaluate the profitability and practicality of sorbitol-to-glycol conversion process as part of semester-long senior design project.
- Responsible for process modeling with HYSYS, economic and design analysis of reactors and membrane separators, and profitability assessments and projections of the process.

PUBLICATIONS

- **Hasyim, M.,** & Rajagopalan, R. (2017). *Ab Initio* Study of Phenomenological Coupling in Pseudocapacitance. In Preparation.
- **Hasyim, M.,** Ma, D. Rajagopalan, R., & Randall, C., (2017). Prediction of charge-discharge and impedance characteristics of electrical double layer capacitor using porous electrode theory. *To Be Submitted to Journal of the Electrochemical Society.*
- **Hasyim, M.**, Berbano, S., Cleary, R., Lanagan, M., & Agrawal, D. (2017). Impedance Spectroscopy Modeling of Lithium Borate with Silica: A Dispersed Ionic Conductor. *Ceramics International* **43**(9), 6796-6806

POSTERS

- **Hasyim, M.**, Ma, D., Rajagopalan, R., & Randall, C., (2017, May) *Ab-initio approach to model impedance and charge-discharge characteristics of electrical double layer Capacitors*. Poster session will be presented at 231st ECS Meeting, New Orleans, LA.
- **Hasyim, M.**, Ma, D., Rajagopalan, R., & Randall, C., (2017, April) *Mathematical Modeling of Electrochemical Capacitors*. Poster session presented at the 13th Annual College of Engineering Research Symposium, University Park, PA.
- **Hasyim, M.**, Lanagan, M., Rajagopalan, R. (2016, August). *Development of polymeric coating for alkali-free thin glass*. Poster session presented at the 8th Annual Penn State REU/RET Symposium, University Park, PA.
- **Hasyim, M.**, Rajagopalan, R. (2016, April*). Electrochemical evaluation of $LaNiO_3$/carbon composite for aqueous asymmetric capacitors*. Poster session presented at the 2016 Undergraduate Exhibition, University Park, PA.
- **Hasyim, M.**, Berbano, S., Cleary, R., Lanagan, M., & Agrawal, D. (2016, April*). Ionic conductivity in two-phase composite Li^+ solid electrolyte*. Poster session presented at the 13th Annual College of Engineering Research Symposium, University Park, PA.
- **Hasyim, M.**, Berbano, S., Cleary, R., Lanagan, M., & Agrawal, D. (2015, April). *Two-phase composite solid electrolyte for intermediate-temperature solid oxide fuel cell*. Poster session presented at the 12th Annual College of Engineering Research Symposium, University Park, PA.

RELEVANT COURSEWORK

Mass Transfer Operations	Chemical Reaction Engineering	Process Fluid Mechanics
Mathematical Modeling	Computational Methods in Engineering	Partial Differential Equations
Materials Engineering	Molecular Thermodynamics	Solid State Physics

LEADERSHIP & ACTIVITIES

PRESIDENTIAL LEADERSHIP ACADEMY **08/14 – Present**

DESK ASSISTANT, ENGINEERING LIBRARIES PENN STATE **07/14 – Present**

SECRETARY, INDONESIAN STUDENTS ASSOCIATION **05/14 – 05/15**

HEAD OF DISPLAY COMMITTEE, INDONESIAN STUDENT ASSOCIATION **05/14 – 05/15**